

สัมประสิทธิ์การแพร่ผสมและความเสียหายตกค้างในวัสดุ InGaAs/InP โครงสร้างวิวิธของส่วนผสมและ
ความเครียดต่าง ๆ

นางสาวสุนิดา อวิโรจนานนท์



วิทยานิพนธ์นี้เป็นส่วนหนึ่งของการศึกษาตามหลักสูตรปริญญาวิทยาศาสตรมหาบัณฑิต

สาขาวิชาฟิสิกส์ ภาควิชาฟิสิกส์

คณะวิทยาศาสตร์ จุฬาลงกรณ์มหาวิทยาลัย


ปีการศึกษา 2544

ISBN 974-03-0313-7

ลิขสิทธิ์ของจุฬาลงกรณ์มหาวิทยาลัย

I 20125215

INTERMIXING DIFFUSION COEFFICIENTS AND RESIDUAL DAMAGE IN InGaAs/InP
HETEROSTRUCTURES OF VARYING COMPOSITION AND STRAIN



MISS SUNIDA AWIROTHANANON

สถาบันวิทยบริการ
สงวนลิขสิทธิ์
A Thesis Submitted in Partial Fulfillment of the Requirements
for the Degree of Master of Science in Physics


Department of Physics
Faculty of Science
Chulalongkorn University
Academic Year 2001
ISBN 974-03-0313-7

Thesis Title Intermixing Diffusion Coefficients and Residual Damage in
 InGaAs/InP Heterostructures of Varying Composition and Strain.
By Sunida Awirothananon
Field of Study Physics
Thesis Advisor Assistant Professor Kiranant Ratanatammapan
Thesis Co-advisor Dr. Sylvain Raymond

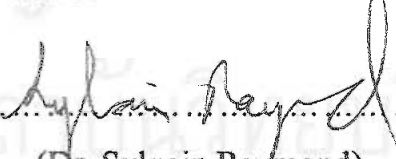
Accepted by the Faculty of Science, Chulalongkorn University in
Partial Fulfillment of the Requirements for the Master 's Degree

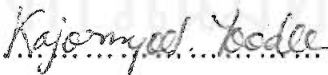
 Dean of Faculty of Science
(Associated Professor Dr. Wanchai Phothiphichitr)


THESIS COMMITTEE

 Chairman
(Associated Professor Anuntasin Tachagumpuch)

 Thesis Advisor
(Assistant Professor Kiranant Ratanatammapan)

 Thesis Co-advisor
(Dr. Sylvain Raymond)

 Member
(Assistant Professor Kajomyod Yoodee)

 Member
(Dr. Rattachat mongkolnavin)

สุนิดา อภิโรจนานนท์ : สัมประสิทธิ์การแพร่ผสมและความเสียหายตกค้างในวัสดุ InGaAs/InP โครงสร้างวิวิธของส่วนผสมและความเครียดต่างๆ. (INTERMIXING DIFFUSION COEFFICIENTS AND RESIDUAL DAMAGE IN InGaAs/InP HETEROSTRUCTURES OF VARYING COMPOSITION AND STRAIN) อ. ที่ปรึกษา : ผศ. กิรณันต์ รัตนธรรมพันธ์, อ.ที่ปรึกษาพร้อม : Dr. Sylvain Raymond 143 หน้า. ISBN 974-03-0313-7.

ประยุกต์วิธีการผสมระหว่างบ่อศักย์ควอนตัม (QWI) กับโครงสร้างบ่อศักย์(QW) InGaAs/InP เป็นเรื่องสนใจมุ่งเน้นวิจัยจากมุมมองศักยภาพของจริงรวมด้านแสงสำหรับการสื่อสารทางไกล ในช่วงคลื่น 1.3-1.6 μm ด้วยต้นทุนการผลิตต่ำ

ในงานนี้ศึกษาถึงสองวิธีการของ QWI: QWI ฝั่งไอออนวิวิธของบ่อศักย์ และ QWI โดยการปลูกความบกพร่อง ทั้งสองวิธีมุ่งเน้นที่ความบกพร่องที่สร้างแบบคัดเลือกบริเวณในสารตัวอย่างเพื่อเพิ่มการแพร่สู่กันของวัสดุระหว่างกระบวนการอบด้วยความร้อนแบบรวดเร็ว การศึกษาถึงความเหมาะสมของ QWI ในแต่ละวิธีการที่ขึ้นกับสองปัจจัยหลัก:

1.ความสามารถคาดการณ์ถึงการเลื่อนของแถบพลังงานนำสู่การควบคุมสภาพการทดลองสำหรับวัสดุในวงกว้าง

2.คุณภาพด้านแสงของชั้นภายหลังการวิวิธบ่อศักย์

งานส่วนแรก เปรียบเทียบผลการวัดการดูดกลืนกับผลการคำนวณที่ได้จากแบบจำลอง ของวิวิธบ่อศักย์ การหาความต่างของระยะการแพร่ของอะตอมกลุ่ม V และกลุ่ม III ($k = \frac{\Delta_V}{\Delta_{III}}$) ของ

$k=4$ เกิดจากแลตทิซคู่เหมาะสม (LM) และ บ่อศักย์ความเครียดดีผสมกับความบกพร่องจากการปลูกวิวิธบ่อศักย์ ขณะที่ $k=\infty$ พบใน LM สารตัวอย่างบ่อศักย์ผสม โดยฝั่งไอออนวิวิธบ่อศักย์ ข้อมูลนี้มีความสำคัญต่อการสร้างแบบจำลองเพื่อการคาดการณ์การเลื่อนแถบช่องว่าง

ส่วนที่สองของงาน วัดช่วงอายุพาหะของสารตัวอย่างที่เตรียมและสารตัวอย่างที่แพร่ผสมแล้ว ที่อุณหภูมิต่างๆกัน พบว่าช่วงอายุพาหะในสารตัวอย่างที่แพร่ผสมแล้วมีความไวต่อการเปลี่ยนแปลงอุณหภูมิมากกว่า ป่งชี้ถึงการเกิดจุดบกพร่องการรวมตัวที่ไม่เปล่งแสง

ภาควิชา ฟิสิกส์.
สาขาวิชา ฟิสิกส์.
ปีการศึกษา 2544

ลายมือชื่อนิสิต..... *Sunida Ajithanam*
ลายมือชื่ออาจารย์ที่ปรึกษา..... *[Signature]*
ลายมือชื่ออาจารย์ที่ปรึกษาพร้อม..... *[Signature]*

4172558023 : MAJOR PHYSICS

KEY WORD: QUANTUM WELL INTERMIXING / PHOTOLUMINESCENCE TECHNIQUES / RESIDUAL DAMAGE / ABSORPTION MEASUREMENT / InGaAs/InP / TIME-RESOLVED PHOTOLUMINESCENCE / DIFFUSION COEFFICIENTS.

SUNIDA AWIROTHANANON : THESIS TITLE. INTERMIXING DIFFUSION COEFFICIENTS AND RESIDUAL DAMAGE IN InGaAs/InP HETEROSTRUCTURES OF VARYING COMPOSITION AND STRAIN. THESIS ADVISOR : Assistant Professor KIRANANT RATANATAMMAPAN, THESIS COADVISOR : DR. SYLVAIN RAYMOND, 143 pp. ISBN 974-03-0313-7.

Quantum Well Intermixing (QWI) methods applied to InGaAsP/InP Quantum Well (QW) structures are the subjects of intense research efforts in view of their potential for low-cost fabrication of photonic integrated circuits in the telecommunication wavelength ranges of 1.3-1.6 μm

In this work, two methods of QWI are investigated: ion implantation QWI and grow-in-defect QWI. Both methods aim at the use of area selective creation of defects in the sample to promote material interdiffusion during a rapid thermal annealing (RTA) process. The applicability of each QWI methods is investigated and it depend on two main factors:

1. Our ability to predict the shifts obtained given controlled experimental conditions for a wide class of materials.
2. The optical quality of the layer after QWI

In the first part of the work, absorption measurements are compared with QWI simulations to quantify the relative interdiffusion length of group-V and group-III atoms ($k = \frac{\Delta_V}{\Delta_{III}}$). Values of $k = 4$ are obtained for lattice-matched (LM) and tensile strain QW intermixed with grown-in-defect QWI, while a value of $k = \infty$ is found for a LM QW sample intermixed via ion implantation QWI. This information is important to establish predictive models of bandgap shifts.

In the second part of the work, carrier lifetimes in as-grown and intermixed samples are measured at varying temperatures. Lifetimes measured in intermixed samples are found to be more sensitive to changes in temperature, suggesting the presence of non-radiative defects.

Department PHYSICS

Field of study PHYSICS

Academic year 2001

Student's signature... *Sunida Awirothananon*

Advisor's signature... *Kiranant Ratanatammapan*

Co-advisor's signature... *Sylvain Raymond*

Acknowledgements

It gives me great pleasure to thank the following people who have assisted me during the period of my research at Quantum Physics group, Institute of Microstructural Science (IMS), National Research Council of Canada (NRC) in Canada.

I would like to say special thanks to Asst. Prof. Kiranant Ratanathammapan, and Dr. Sylvain Raymond for his help, ideas and enthusiasm throughout the course of this work. Thank always give me a hand on my problems! Thank also to Dr. Sylvain Charbonneau for his supporting and kindness.

I wish to express my gratitude to Dr. Phillip Poole for grown materials and training x-ray technique, Dr. Goef Aers for simulation program and put your hand in my problem, and Joan Haysom for great discussion. Tom Simpson for implantation process.

I am also grateful to thank the following people who have collaborated in the project: Ed Vilks and Shawn Poirier for their outstanding technical support, Karin Hinzer and all of my co-workers and whom have given me a hand. Other scientists at NRC have contributed to my education: Dr. Jacques Lefebvre, Dr. Robin Williams and all the others with who I had discussions. Thank you.

I would like to thank National Science and technology development agency (NSTDA) in Thailand for giving me a chance and financial support to work at NRC, Canadian International Development Agency (CIDA) and Canada-ASEAN center (CAC) for supporting the airplane ticket.

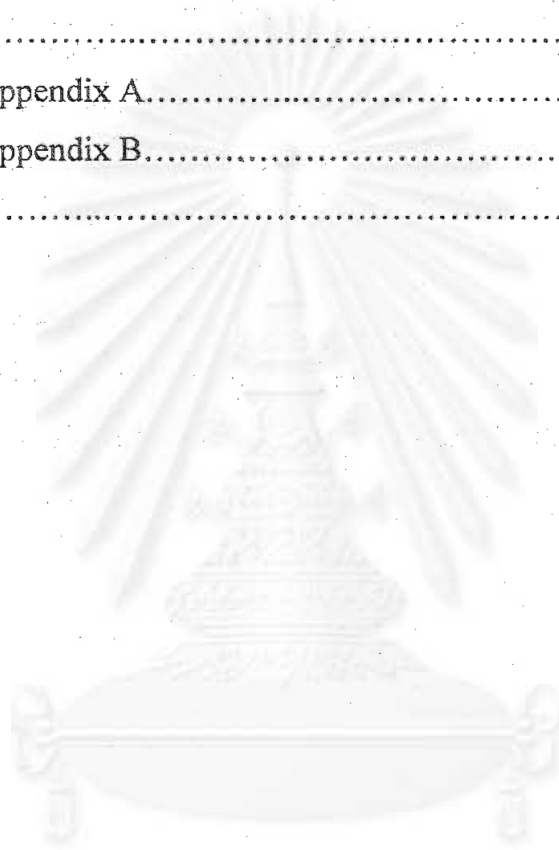
Finally, I am eternally indebted to my mom (Nitaya Awirothananon) and dad (Somsak Awirothananon) for their continuing support and encouragement.

Table of Contents

	Page
Thai Abstract.....	iv
English Abstract.....	v
Acknowledgement.....	vi
Table of contents.....	vii
List of Tables.....	x
List of Figures.....	xi
Chapter I Introduction.....	1
I.1 Quantum Well intermixing.....	3
I.2 Techniques for modifying interdiffusion rates in QWs.....	6
Chapter II Theory.....	10
II.1 Band structure.....	10
II.2 Quantum well energy level.....	15
II.2.1 Infinite square well potential.....	16
II.2.2 Finite Square well potential.....	19
II.2.3 Arbitrary well potential.....	25
II.3 Direct- and indirect- gap semiconductor.....	26
II.4 Recombination	27
II.4.1 Recombination process.....	28
II.4.1.1 Direct band-to-band recombination.....	29
II.4.1.2 Indirect band-to-band recombination.....	36
II.4.2 Effect of non-radiative centers on lifetime	40
II.5 Quantum Well Intermixing simulation.....	44
II.5.1 diffusion phenomena.....	45
II.5.2 Simulation for group III-V semiconductor.....	49

	Page
II.5.3 Theoretical background for simulation.....	56
II.5.3.1 compositional profiles.....	56
II.5.3.2 Quantum states for a lattice-matched square QW.....	57
II.5.3.3 Effect of strain	59
II.5.3.4 Quantum states for an arbitrarily shaped QW.....	61
II.5.3.5 Optical transition energies.....	62
II.5.3.6 Use of the result for QWI studies.....	63
II.5.3.7 Accuracy of the modeling.....	63
II.5.3.8 Comments on as-grown QWs.....	65
Chapter III Experimental set-up.....	66
III.1 Characterized techniques.....	66
III.1.1 Photoluminescence (PL).....	66
III.1.1.1 single PL system.....	67
III.1.1.2 mapping PL system.....	70
III.1.2 Time-resolved photoluminescence (TRPL).....	73
III.1.3 Absorption technique.....	78
III.2 Rapid thermal annealing method (RTA).....	81
III.3 Implantation.....	86
Chapter IV Interdiffusion and Residual damage.....	94
IV.1 Determination of Interdiffusion constant (K value).....	94
VI.1.1 Structure of sample.....	95
VI.1.2 Absorption data.....	106
VI.1.3 simulation data and point to find <i>k</i> value.....	109
VI.2 Investigation of QW damage	115
VI.2.1 System response.....	117
VI.2.2 Lifetime of In _x Ga _{1-x} As/InP heterostructures.....	118
VI.2.3 Lifetime Vs temperature.....	121

	Page
Chapter V Summarization and Future work.....	126
V.1 Summarization and Suggestion.....	126
V.2 Future work.....	127
References	128
Appendices	137
Appendix A.....	138
Appendix B.....	140
Biography	149



สถาบันวิทยบริการ
จุฬาลงกรณ์มหาวิทยาลัย

List of Tables

		page
Table 2.1	Energy band offset of type I,II alignment semiconductors. The zero of energy is chosen at the top of the valence band of material A.	15
Table 2.2	Conservation of energy and momentum of direct and indirect transition.	26
Table 3.1	Cleaning process for RTA	86
Table 3.2	Density and atomic mass, mass number of atom and compound using this thesis	93
Table 4.1	Structure of samples	96
Table 4.2	The best fitting value of composition Ga and QW width by using error function model compare to the ideal one.	110

List of Figures

		page
Fig 1.1	Schematic diagram of a generic PIC containing a laser diode is directed to splitter through electroabsorptive modulator.	3
Fig 1.2	The conduction band and valence band potential energy profiles for an as-grown rectangular single quantum well structure. E_g and E_g' denote the energy gap before and after intermixing process. Closed circles are represented atoms in the barrier region and opened circles are presented atoms in the QW region.	5
Fig 2.1	Schematic of band structure in real space of (a) single quantum well and (b) multiple QW.	11
Fig 2.2	Conduction and valence band energy plotted as a function of momentum in figure (a) and as a function of energy in figure (b). For single QW, active QW layer (material A) sandwiched in between barrier layer (material B) is plotted a function of energy in figure (c).	13
Fig 2.3	Schematic (a) type I alignment and (b) type II alignment of semiconductor QW material	14
Fig 2.4	Schematic of infinite square well potential	16
Fig 2.5	Wave function and state in infinite square well	19
Fig 2.6	A finite-square well potential of width L_z and depth ϕ_0	20
Fig 2.7	Graphical solution of equation (2.54) giving the allowed even boundstate energies. Dot line is represented the right handside of equation (2.54) and solid line is represented the left handside of equation (2.54)	23

	Page	
Fig 2.8	Graphical solution of equation (2.58) giving the allowed odd bound-state energies. The dash line is represented solution of right handside of equation (2.58) and the solid line is represented left handside of equation(2.58)	24
Fig 2.9	Closed and opened circles represent atoms in the QW and barrier region of crystalline semiconductor as shown above figure (a). After intermixing process is performed, those atoms exchange between interface area as shown below figure (b). This causes gradually change shape of QW potential as shown in figure (b), which is one example of arbitrary QW potential.	25
Fig 2.10	Schematic of (a) direct-gap and (b) indirect-gap semiconductors in \bar{k} space	26
Fig 2.11	Illustration of band-to-band of absorption and recombination process in direct-gap semiconductor.	30
Fig 2.12	Schematic representation of Bloch function in semiconductors (a) periodic potential, (b) full wave function, (c) cell-periodic part U_k and (d) plane wave part	32
Fig 2.13	Illustration of band-to-band of absorption and recombination process in indirect-gap semiconductor.	36
Fig 2.14	Band diagram of impurity semiconductor material, which intermediate state represents either non-radiative recombination center or trap state with the number of defects as $N_1(t)$. The number of carriers in the conduction band is denoted by $N(t)$.	40
Fig 2.15	Schematic of intensity as a function of time. Number of carriers at beginning time is 1×10^{24} atoms	42

	Page	
Fig 2.16	Diffusion path in an element crystal is introduced (a) diffusion interstitial, (b) diffusing vacancy, (c) concerted exchange of dopant, (d) interstitial kick-out and (e) interstitial kick-in. Opened circle is host atom and closed circle is defect.	46
Fig 2.17	Band diagram of given parameter in program written by Dr. Goef Ares at National Research Council of Canada (NRC).	51
Fig 2.18	Growth of an epilayer on a perfectly lattice-matched substrate	54
Fig 2.20	square quantum well energy levels	58
Fig 3.1	Schematic of (a) single point PL system at IMS, NRC in Canada and (b) recombination processes in semiconductors.	69
Fig 3.2	Photoluminescence of an non-intermixed InGaAs/InP QW sample at varying temperature.	70
Fig 3.3	Schematic of mapping PL system at NRC.	71
Fig 3.4	Spectral data is displayed (a) intensity as a function of x-y position and emitted photon energy (wavelength) as a function of x-y position.	72
Fig 3.5	(a) Schematic of laser setup for the TRPL techniques. (b) Set-up time-resolved photoluminescence at the wavelength of 0.4 – 1.7 microns used at national research council of Canada.	74
Fig 3.6	Principle of operation of a single-photon correlation. The temporal decay is gradually built up by making successive conversions of the time elapsed between the incident laser pulse and the detected luminescence photon.	76
Fig 3.7	Setup absorption measurement technique at national research council of Canada (NRC)	79
Fig 3.8	Schematic of absorbance spectrum obtained by dividing spectrum from QW and substrated sample by spectrum from substrate. Light- and heavy-hole n=1 transitions are obtained.	80

	Page	
Fig 3.9	Inside view of a commercially available RTA furnace. The wafer is inserted into the quartz isolation tube and heated by infrared and visible radiation from the lamps arranged on each side of the isolation tube.	83
Fig 3.10	Typical time-temperature profile of a sample during rapidly thermal annealing (RTA) which using in this thesis.	84
Fig 3.11	Thermocouple using in this thesis	84
Fig 3.12	Schematic of placing sample	85
Fig 4.1	Schematic representing the sample in cross-section. Those three wafers have similar cross-section structure but different in Ga composition in QW layer and the width of each layer as listed in table 4.1.	95
Fig 4.2	Schematic of PL map performed on non-annealing (on left handside) and annealed (right handside) at different temperature in range 625 C to 750 C for 60 sec-total-time of sample CBE99-172.	97
Fig 4.3	Evolution's CBE99-172 sample of energy shift from PL mapping in figure 4.2 plotted as function of annealing temperature in step of 25 °C for 60 sec-total time.	98
Fig 4.4	Energys shift evolution of CBE99-064 samples plotted as a function of annealing temperature in step of 25 °C for 360 sec-total time.	99
Fig 4.5	PL spectra at (a) 4.2 K and (b) 300 K for tensile strain samples (CBE00-120) annealed for 30 sec.	100
Fig 4.6	Evolution of blueshift of CBE00-120 PL spectra in figure 4.5: opened circle for PL spectra at 4.2 K and closed circle for PL spectra at 300 K.)	101

	Page
Fig 4.7	Density of implanted ions for CBE99-172 sample plotted as a function of penetrated depth from the surface by using SRIM simulation. 102
Fig 4.8	Evolution of single point photoluminescence spectra of CBE99-172 sample implanted and annealed for 150 sec-total time. PL was performed at 4.2 K. 103
Fig 4.9	Intensity of CBE99-172 samples plotted as a function of energy. This sample is excited by 490-nm Ar-laser and 980-nm laser diode. The above, middle, and bottom figure are from As grown, 6×10^{11} ions/cm ² implanted dose, and 2×10^{13} ions/cm ² implanted dose sample, respectively 104
Fig 4.10	Cross-section of wavelength PL spectra of CBE99-172 sample plotted as a function of distance with our PL mapping system. PL mapping is performed at 300 K... 105
Fig 4.11	Evolution of blueshift as a function of implanted dose for CBE99-172 QW samples annealed at 700 C for 150-sec total time 106
Fig 4.12	Normalized absorbance spectra from CBE99-172 QW sample implanted at (b) 6×10^{11} ions/cm ² , (c) 2×10^{12} ions/cm ² , (d) 5×10^{12} ions/cm ² , (e) 2×10^{13} ions/cm ² , (f) 5×10^{13} ions/cm ² and (g) and 1×10^{14} ions/cm ² but (a) non-intermixed sample. 107
Fig 4.13	Normalized absorbance spectra of growth-in-defect CBE00-120 sample annealed at different temperature for 30 sec. Each piece was annealed (B) at 625 C, (C) at 650 C, (D) at 675 C, (E) at 700 C, (F) at 725 C, and (G) at 750 C but (A) non-intermixed piece 108

	Page	
Fig 4.14	Normalized absorbance spectra of growth-in-defect CBE99-064 sample annealed at different temperature for 30 sec. Each piece was annealed (ii) at 625 C, (iii) at 650 C, (iv) at 675 C, (v) at 700 C, (vi) at 725 C, and (vii) at 750 C but (i) non-intermixed piece	109
Fig 4.15	Hh-lh splitting plotted as a function of hh energy shift for CBE99-172 QW samples created defects by implantation technique. Closed circles represent to experimental data from absorption measurement and solid line represent simulation data by varying k value	111
Fig 4.16	Hh-lh splitting plotted as a function of hh energy shift for CBE99064 QW samples created defected by growth-in-defect QWI technique. Closed circles represent to experimental data from absorption measurement and solid line represent simulation data by varying k value	112
Fig 4.17	Hh-lh splitting plotted as a function of hh energy shift for CBE00120 tensile QW samples created defected by growth-in-defect QWI technique. Closed circles represent to experimental data from absorption measurement and solid line represent simulation data by varying k value.	113
Fig 4.18	Phase space of $\text{In}_x\text{Ga}_{1-x}\text{As}_y\text{P}_{1-y}$ gaps at 4 K shown the relation of interdiffusion of group-III and group-V atoms.	114
Fig 4.19	Typical instrumental response from 6.36 nm FWHM input laser pulse at a wavelength of 728.5 nm as shown at the above corner. Temporal resolution is ~270 ps	117

- Fig 4.20 TRPL measurement performed at 4.2 K with pulse laser at repetition rate of 4 MHz on implanted sample (CBE99172) by varying implanted doses: (i) implanted dose at 6×10^{11} ions/cm² (at 1298 nm), (ii) implanted dose at 5×10^{12} ions/cm² (at 1286 nm), (iii) implanted dose at 5×10^{13} ions/cm² (at 1288 nm), and (iv) implanted dose at 1×10^{14} ions/cm² (at 1229 nm) 119
- Fig 4.21 Decay time of CBE99172 samples (from fig 4.20) by varying ion implanted dose from 6×10^{11} ions/cm² to 1×10^{14} ions/cm² 119
- Fig 4.22 Decay time of low-temperature grown sample (CBE99064) plotted as a function of energy shift measured by PL technique 121
- Fig 4.23 Temperature dependence TRPL on non-intermixed CBE99-172 sample (RTA at 700 C for 150-sec-total-time) by using 710-nm pulse laser. Dot and solid line are for guide-eye. 123
- Fig 4.24 Intensity PL by varying temperature for non-intermixed CBE99-172 samples by using 710-nm pulse laser. Dot line is guide-eye for merged of lower and higher energy peak by varying temperature. 123
- Fig 4.25 Log integrated intensity PL vs temperature dependence for non-intermixed CBE99-172 samples by using 980-nm laser diode at 1.89 mW. 124
- Fig 4.26 Temperature dependent TRPL of intermixed CBE99-172 sample implanted at 2×10^{12} ions/cm² (RTA at 700 C for 150-sec-total-time) by 710-nm CW laser. Dot and solid line are for guide-eye. 125
- Fig 4.27 Log integrated intensity PL vs temperature dependence for intermixed CBE99-172 sample implanted at 2×10^{12} ions/cm² (RTA at 700 C for 150-sec-total-time) by using 980-nm laser diode at 1.89 mW. Dot line is for guide-eye. 125

CHAPTER I

INTRODUCTION

Recently the monolithic integration of photonic device has become an important issue for the fabrication of emitter and receiver components that constitute part of telecommunication systems. To enhance the performance of modern telecommunication systems, it is required to increase operational bandwidth, to reduce demands on the drive circuits that provide external modulation, and to increase the functionality of device. The increasing demands for optoelectronic circuits are based on high reliability and lower manufacturing costs. Furthermore, a large number of groups worldwide over the last few years have produced several applications. For instance, J.J. He and co-workers [1] have reported about an independent optical amplifier based on polarization. They have reported that if the interdiffusion rate of the anions is larger than that of the cations, the blue shift in the ground state heavy hole transition energy after implantation and annealing is greater than the light hole state blue shift, bringing the two bands together. Current voltage measurements indicate that junction characteristics are well maintained after implantation. Furthermore, the modification of refractive index is caused by increasing bandgap in QW material. In structures containing only a few QWs, this refractive index change will have only a small effect on the optical propagation constant. But the optical overlap between the intermixed well and the optical wave can be large enough to give useful changes in the refractive index in MQW structure. The change of refractive index is useful to provide either optical confinement [2] [3], gratings, or even laser reflectors [4] [5].

With this in mind, we can establish the most important requirement for monolithically integrated optoelectronic devices of differing functionalities on the same wafer without regrowing technology in order to achieve practical waveguiding PIC. Therefore, the following elements are required,

1. There must be large, controllable bandgap energy difference between the various devices in the PIC.

2. The losses in the integrated waveguide devices must be comparable to or lower than that present in the as-grown structure.
3. The electrical properties of the various devices must suffer zero or insignificant deterioration due to the processing techniques
4. There should be no substantial adverse effect on the operating lifetimes of the various devices in the PIC after processing.
5. Any other process-initiated change in the properties of the devices must be either neutral or advantageous to the PIC

The advantage of being able to tune the material provides a way to improve the performance of photodetectors and modulators. Attractive distributed-feedback and vertical cavity laser dynamics have been shown due to some unique device physics of the quantum well intermixing.

To reach the above goal, the selective area bandgap tuning as shown in fig 1.1 is one possible technique to build PICs. Three different devices are fabricated on the same substrate. Energy bandgap of laser is lower than that of modulator, which is lower than that of the waveguide. For example, laser diode is directed to selective waveguide through modulator in the plane of the wafer. The laser wavelength should be absorbed as little as possible to selective waveguide in order to minimize the amount of optical power loss. The property of light that is modulated generally depends upon the particular application and could involve modulating the amplitude of the optical signal, the phase of the signal, widths of pulses being sent etc. At present all modulation schemes in optical communications involve intensity modulation of the optical signal. Frequency modulation is not used due to the difficulties in maintaining phase correlations in lasers. There are two schemes used to modulate the optical signals in laser diodes. The first one is direct modulation in which an electronic circuit is designed to simply modulate the current injected into the device. Since the injected current controls the light output, one has the desired amplitude modulation. The second one is external modulation scheme. The light output passes through a material whose optical properties can be modified by an external means.

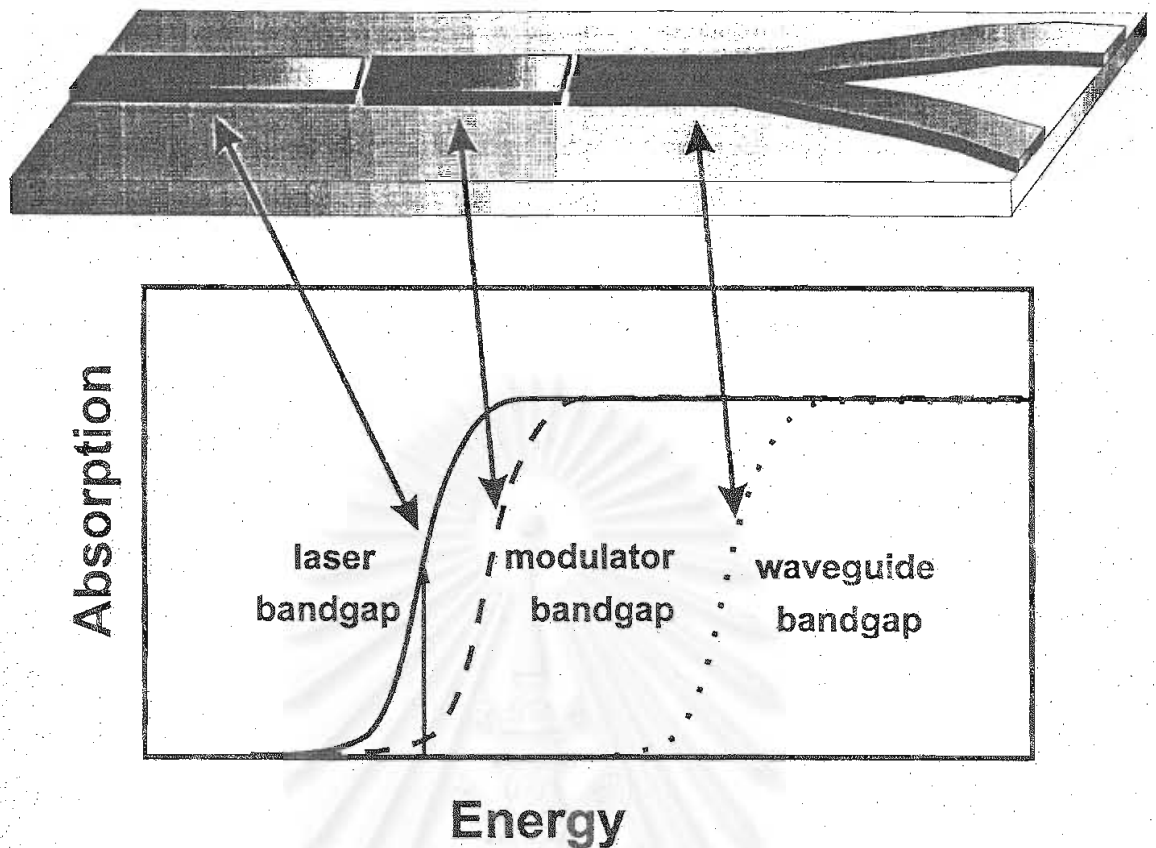


Fig 1.1 Schematic diagram of a generic PIC containing a laser diode is directed to splitter through electroabsorptive modulator.

1.1 Quantum Well Intermixing

Quantum Well Intermixing is a technique of fabricating integrated optoelectronic devices using spatially selective modification of quantum well shape after standard growth which, in turn, modifies QW bandgap energy. This diffused quantum well is a non-square quantum well produced by interdiffusion of constituent atoms through the heterointerface. In the literature, diffused quantum well is also referred to as quantum well mixing or intermixing and quantum well disordering. In this thesis, this process will be referred to as "*Quantum well intermixing*". It can be said that quantum well intermixing is a post growth processing technique, a method to modify the properties of semiconductor material after growth. For example, in InGaAs based on InP QWs material, the arsenic atoms in the QW region is exchanged with the phosphorous atoms in the barrier after intermixing process is employed. Also, Indium atoms in the QW are exchanged with Indium atoms in

the barrier region as represented in fig 1.2. Closed and opened circles represent atoms in the barrier and QW region, respectively. The intermixing of atoms in an interface area between QW and barrier results in modification of shape of the QW and shifted the energy gap. For III-V semiconductors, energy gap of intermixed QW becomes larger than that of non-intermixed QW. This shift in energy is called blue shift. Magnitude of blue shift can be influenced by many factors such as the difference in bandgap energy between the QW and the barrier material, thickness of QW, and the amount of strain presented in the QW and barrier material. Compositions can also affect the blue shift of the transition energy. QWI technique is quite simple due to the fact that it require only a single growth and rapid thermal annealing to modify. However, the large concentration gradient of atomic species across the QW/barrier interface is a limitation of this technique. Intermixing process in III-V semiconductor material may be depended on the movement of either only group-III atoms or only group-V atoms. Besides it can be up to moving of both group-III atoms and group-V atoms. As a result of this, diffusion process can be considered in two cases: self-diffusion rate and diffusion of impurities during intermixing. Self-diffusion rate is determined by both the diffusion rate of the defects and concentration of defects. At thermal equilibrium, amount of self-diffusion in high purity material is small. Diffusion of impurities during intermixing can be examined for two effects. First effect is that unintentional intermixing will take place in regions other than that implanted region. Second effect is that the volume concentration of the impurity falls during diffusion and eventually drop below the threshold concentration at which impurity enhances disordering take place.

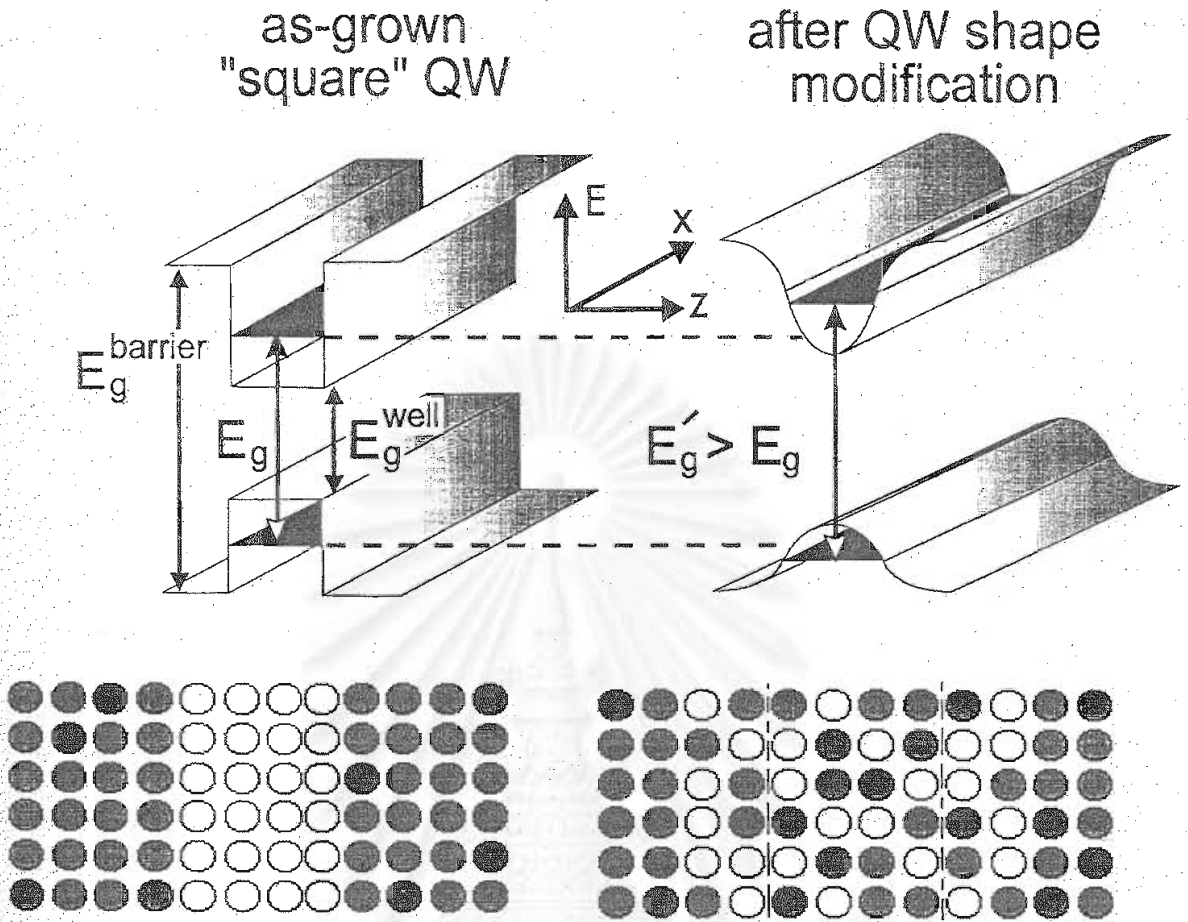


Fig 1.2 The conduction band and valence band potential energy profiles form as-grown rectangular single quantum well structure. E_g and E'_g denote the energy gap before and after intermixing process. Closed and opened circles represent atoms in the barrier region and QW region, respectively (before intermixing).

Bandgap modification by QWI technique is a powerful for monolithically integrating optoelectronic devices of varying functions on a single wafer because of three reasons. First reason is easy to implement and simple for fabrication of many complex photonic IC's. Then it is practically enough to be adopted by industry. Second reason is to accurate modify the QW materials bandgap and optical properties and to make use of these tuning ability to integrate several device structures to form photonic IC's. In practical, this allows a multi-section-integrated structure will be fabricated for wide bandwidth and multi-wavelength applications such as demonstrate its use for wavelength division multiplexing (WDM) in high bit rate communication

system. Final reason is that QWI techniques have no detrimental effect on either the optical, electrical, or lifetime properties of optoelectronic devices.

Furthermore, QWI also causes a change in refractive index [6]. Refractor index is useful to provide laser reflectors, optical confinement and grating. If the number active QW layer is a few, refractive index change will be negligible. Effect of polarization can be distinguished to dichroism and birefringence. Dichroism is arise from the selection rules governing optical absorption in a QW with either TE polarization exciting transition from both hh and lh confined state into the conduction band state or TM polarization exciting transition only from lh state to conduction band. Polarization is increased with enlarged intermixing process. Absorption edge occurs at longer wavelength for TE polarization than TM polarization.

I.2 Techniques for modifying interdiffusion rates in QWs.

Several approaches to integrate circuits based on QW active layers are emerging in order to achieve spatially selective control over the optical and electrical characteristics of different elements in the PICs. Regrown technique, varying the width of QWs across the wafer during a single stage of expitaxy, cap annealing disordering technique, growth on a patterned substrate, ion implantation induced QWI, growth-in-defect QWI and laser assisted disordering have all been investigated for that purpose. In this section, we briefly discuss the extent of the literature of each technique.

1. Cap annealing disordering technique

In this technique, either Si_2N_4 [7] or SiO_2 [8] [9] film is deposited on the surface of the wafer. Upon annealing, this cap selectively absorbs one species of atoms from the wafer. It thus causes creating vacancies and possibly other defect types above the QW region. Annealing procedure is applied to diffuse some defects through QW layer and promote interchange of atoms between barrier and QW material. For example, In GaAs-AlGaAs materials, SiO_2 [10] is known to induce out diffusion of Ga during annealing, and to generate

vacancies. These Ga vacancies then propagate down to the QW and enhance the intermixing of Ga and Al. Hence, the bandgap becomes larger in the well material by partial disordering of the two materials. An advantage of this technique is free of impurities such as silicon that can result in optical loss due to free carrier absorption. Moreover, it does not require regrown process.

2. Regrowth technique [11] [12]

A full wafer will be grown by current generation of vapor and beam growth techniques such as molecular beam epitaxy (MBE), chemical beam epitaxy (CBE), and metal-organic vapor phase epitaxy (MOVPE). And then the active layer is etched from certain regions of the sample before overgrowth of the structure with the same upper cladding layers is operated. In fact, this technique is not popular because the entire production process is complex, which will not provide cost-effective reliable products.

3. Growth on a patterned substrate [13]

Grown on a patterned substrate is one of useful techniques for the integration of optoelectronic components in a single growth step. Three techniques are generally made use of grown on a patterned substrate. A first technique is chemical etching process employed to create a pattern on the wafer determined by the characteristics of the mask. Second technique is grown by molecular beam epitaxy (MBE) together with variation in the growth rate on different crystallographic planes. Last technique is lithography technique. Lithography is the creation of a pattern in a resist layer, usually an organic polymer film that is spun on the surface of the substrate. The resist is exposed to electrons, ions or photons through a mask and the pattern on the mask is developed by selectively removing either the exposed areas of resist or unexposed areas. Development of the resist is achieved with a solvent that brings out the pattern on the mask due to the solubility difference created by the exposure. Controlling and manipulating pattern is the limitation of these techniques.

4. Laser assisted disordering

Laser induced QW intermixing is direct write process that can pattern impurity induced layer disordering. This technique employs a highly focused Ar^+ laser beam. For example, J.J. Dubowski and coworkers [14] fabricated AlGaAs-GaAs QW material and created defects by laser beam with speed at 85 microns/sec through the heterostructure sample encapsulated with a 90 nm layer of Si-Si₃N₄. The laser beam interaction region will result in a smooth cylindrical section on the micron scale. Annealing is then applied to drive the Si into the as-grown crystal, resulting in a local mixing of the crystal layers. However the laser assisted disordering can required high power densities to melt the material and can thus cause an undesirable redistribution of dopants out with the active region of the device. Absorption of the high energy pulse result in bond breaking and disruption to the lattice, leading to a localized increase in the density of point defects. Advantages of this technique are flexible process for optoelectronic device and circuit fabrication; however, a direct-write system is not an optimum configuration for many applications.

5. Ion implantation induced Quantum well intermixing.

Ion implantation technique is that direct injection of ionized and energetic atoms into a solid is operated in order to significantly enhance the interdiffusion rate, and control the lateral and vertical depth of diffusion. The ions injected will carry energies ranging from a few keV to several MeV, and implant doses from 10^{10} to more than 10^{15} ions/cm². Using small implantation energy, the damage introduced to the lattice structure will be reduced but with a decrease in the penetration depth, while with small dose of implants, there will be lesser enhancement of diffusion rate. Different combinations of ions and substrates are possible and the most commonly used ones are p-type ions, n-type ions, neutral type ions and constituent ions. It was found that the use of neutral ions could prevent the production of free carriers induced by the charged ions (n-type or p-type) which will introduce propagation loss and thus

reduce the refractive index of the intermixed QW materials. Rapid thermal annealing (RTA) is an essential step in impurity diffusion to promote its diffusion rate while impurity diffusion process undergoes a very slow rate on its own at conventional conditions. Most of the rapid annealing temperature is usually performed in the range from 400 °C to 1000 °C, and under a chemical environment with N₂ or even in vacuum to prevent oxidation to occur.

6. Growth-in-defect QWI.

In this technique, wafer is grown at standard temperature from substrate to QW layer and then grown temperature is subsequently decreasing to create defects above active QW layer. An annealing procedure is performed to diffuse defects through QW layer and promote interchange of atoms between QW and barrier.

In the following chapter in this thesis will emphasize in intermixing diffusion of InGaAs/InP QW structure introduced defects above QW layer by low-temperature growth and ion implantation techniques. Rapid thermal annealing (RTA) process is operated to diffuse defects down to QW layer. This process causes a local partial averaging of the energy bandgaps of the two materials comprising the quantum well and barrier, so the energy bandgap of the intermixed section is greater than that of the unmodified QW. A waveguide formed in the intermixed section will thus be transparent to the light generated in the laser formed from the unmixed layers. Interdiffusion coefficient – proportional to interdiffusion rate of group-III and group-V species- can be characterized by Photoluminescence and absorption measurement technique as well as simulation. Residual damage in the semiconductor material monitors by time-resolved photoluminescence (TRPL) technique. This will discuss in chapter 3 and chapter 4.

CHAPTER II

THEORY

The basic ideas and concepts for discussion of experimental results are introduced in this chapter. In section 2.1, band structure is previously introduced to understand structure of QW. To characterize properties of semiconductor, wave function and energy eigenvalue of material for infinite square well, finite square well and arbitrary well potential are subsequently solved in section 2.2. Then we discuss recombination lifetime of direct and indirect bandgap semiconductors in section 2.3. Discussion of effect of non-radiative center is also included in this section. Finally, the QWI simulation software used at National research Council of Canada is described in the last section of this chapter.

II.1 Band structure

High quality ultrathin heterostructure materials can be produced by means of epitaxial techniques such as molecular beam epitaxy (MBE), chemical beam epitaxy (CBE) or metal organic chemical vapor deposition (MOCVD). These techniques can be employed to grow quantum-confined semiconductor materials such as Quantum Well (QW), Quantum Wire (QWr) and Quantum Dot (QD) structures. In this study we will concentrate on QW structures, which are essentially composed of a thin low-energygap material surrounded by a thicker high-energygap material. Both layers are grown on a substrate as shown in figure 2.1 (a). Normally, the thickness of the barrier layer is larger than that of the QW that is less than 100 nm. If several repetitions of the QW and barrier layer have been deposited on a substrate, this would be called a multiple QW (MQW) semiconductor structure as shown in fig 2.1 (b).

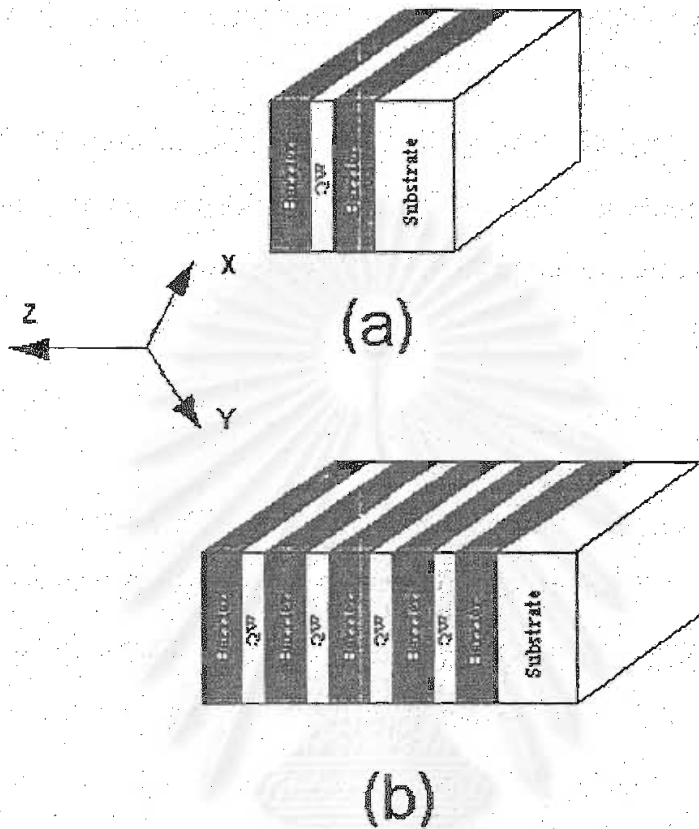


Fig 2.1 Schematic of band structure in real spaces of (a) single quantum well and (b) multiple QW.

Models to obtain realistic band structures of the above semiconductor structures can be separated in two main categories:

1. Methods which describe the entire valence and conduction bands.
2. Methods which are restricted to the bandedge near $\bar{k} = 0$.

For the first category, techniques such as the tight binding method, the pseudopotential method and orthogonalized plane wave method have been used to evaluate the band structure. Those techniques are widely used for describing real semiconductor; however, techniques in the second category such as perturbation techniques are simpler if one is only interested in phenomena near the bandedge. The reader can find more details about those types of

calculations in physics of semiconductors written by Jasprit Singh [22]. Effective mass theory, which is a valid description of states near the band edge, is employed to study QW states in this work [27]. According to Bloch's theorem, the electron wavefunction in a periodic potential is given by:

$$\Psi(\vec{r}) = \mu(\vec{r})\phi(\vec{r}) \quad (2.1)$$

where $\mu(\vec{r})$ is a function with the periodicity of the crystal lattice, and $\phi(\vec{r})$ is the envelope function determined by the boundary conditions. Using effective mass theory near the band edge, the Schrödinger equation for $\phi(\vec{r})$ can be written as:

$$\left[-\frac{\hbar^2}{2m^*_0} \nabla^2 + V(\vec{r}) \right] \phi_i(\vec{r}) = E\phi_i(\vec{r}) \quad (2.2)$$

where m^*_0 is electron effective mass in the crystal. i denote either electron or hole. E is the energy eigenvalue of wave function, $\phi(\vec{r})$, and $V(\vec{r})$ is periodic potential if the electrons move freely in 3-dimension of crystal that contained N periods in a total length $L = (Na)^3$ where a is lattice constant. The solution to this equation is given by equation (2.3) when the simplest potential is applied. We assume $V(\vec{r})$ is a small value and regard this term as a perturbation by comparison with the kinetic energy term.

$$\begin{aligned} \phi(\vec{r}) &= \frac{1}{\sqrt{V}} e^{i\vec{k} \cdot \vec{r}} ; \vec{k} = \ell_r \frac{2\pi}{Na} \hat{e}_i \\ E &= \frac{\hbar^2 |\vec{k}|^2}{2m^*_0} \end{aligned} \quad (2.3)$$

where ℓ_r and N are integer. This analysis can be applied either to electrons in the conduction band or to holes in the valence band provided that the corresponding effective masses are used. From the above energy spectrum, one can see that the energy dispersion relationship near the band edge ($\vec{k} = 0$) is quadratic for both conduction and valence band. This is illustrated in fig. 2.2 (a) with the valence band dispersion inverted as compared to that of the conduction band, in agreement with the definition of holes in a semiconductor. The energy difference between the lowest point in the conduction band, which

is called the conduction band edge, and the highest point in the valence band, which is called the valence band edge, is termed the energy gap. Conduction and valence band energy (E) are plotted as a function of momentum (\vec{k}) in figure 2.2 (a). Band diagram in figure 2.2(a) is plotted energy as a function of growth direction (in z-direction) in figure 2.2(b). In case of single QW, active QW layer (material A) sandwiched in between barrier layer (material B) is plotted in band diagram as shown in figure 2.2(c).

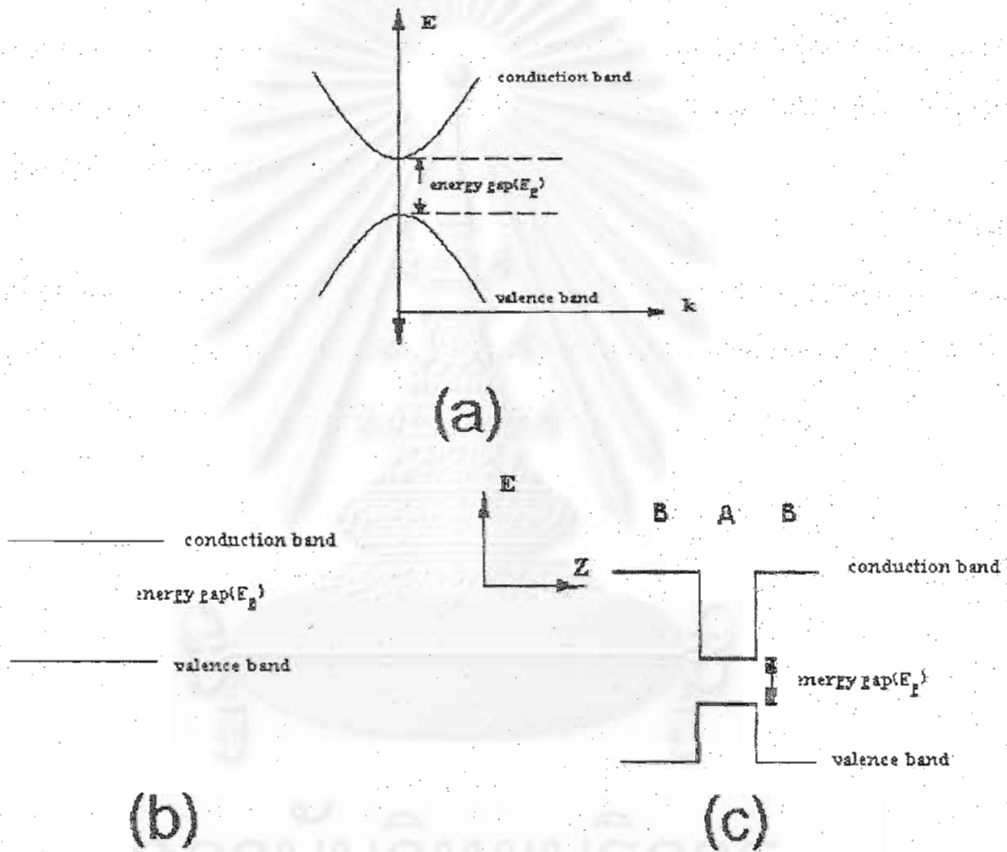


Fig 2.2 Conduction and valence band energy plotted as a function of momentum in figure (a) and as a function of energy in figure (b). For single QW, active QW layer (material A) sandwiched in between barrier layer (material B) is plotted a function of energy in figure (c).

Band diagram in fig 2.2(c) is one type alignment of semiconductor material. Generally alignment type of semiconductor material is classified into type-I and type-II alignments as shown in Fig 2.3. Electrons in the conduction band and holes in the valence band of type I alignment material in fig 2.3 (a)

are confined in QW region because the lowest energy point of the conduction band and the highest energy point of the valence band are in the QW region. So recombination process will mostly occur in this region. On the other hand, electrons in the conduction band of type II alignment as shown in Fig 2.3(b) are confined in QW region while holes in the valence band are confined in the barrier region. This spatial separation has consequences for the efficiency of recombination because electrons in the conduction band of QW region are difficult to recombine radiatively with holes in the valence band, which are not in the same region. This leads to two characteristic features. First characteristic is that the energy of the emitted photon is shifted to lower energies, compared with absorption photon energy by a quantity,

$$\Delta E = \Delta E_v \quad (2.4)$$

Second characteristic is that decay time of type II alignment is generally longer than that of type-I alignment because electrons in QW-conduction band tried to recombine with holes in the barrier-valence band.

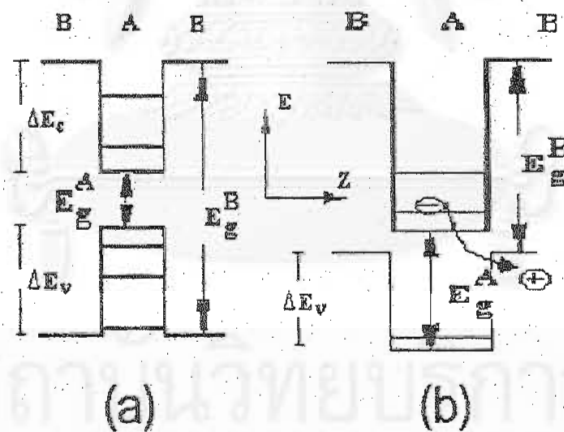


Fig 2.3 Schematic (a) type I alignment and (b) type II alignment of semiconductor QW material.

Band offset of type-I and type-II alignment in semiconductor QW material as shown in fig 2.3 can be explicitly defined in table 2.1. Normally, alignment type of material can be classified by Q value that is ratio of energy difference between QW and barrier layer for conduction (ΔE_c) to valence band (ΔE_v) as illustrated in equation (2.5). For the type-I alignment, energy difference

between QW and barrier region is positive in conduction band but negative in valence band. So Q value in the definition of equation (2.5) is negative as shown in table 2.1. On the other hand, energy difference between QW and barrier region in type-II alignment is negative for both conduction and valence band. So Q value is positive.

$$Q = \frac{\Delta E_c}{\Delta E_v} \quad (2.5)$$

Table 2.1 Energy band offset of type I, II alignment semiconductors. The zero of energy is chosen at the top of the valence band of material A.

Type I alignment	Type II alignment
$E_v^A - E_v^B = \Delta E_v > 0$	$E_v^A - E_v^B = \Delta E_v < 0$
$E_c^A - E_c^B = \Delta E_c < 0$	$E_c^A - E_c^B = \Delta E_c < 0$
	$\Delta E_v, \Delta E_c < E_g^B$
$\Delta E_v, \Delta E_c < E_g^B - E_g^A$	$\Delta E_v, \Delta E_c > E_g^B - E_g^A$
$Q = \text{negative}$	$Q = \text{positive}$

II.2 Quantum well energy level

Schrodinger equation in quantum mechanic is employed in order to characterize properties of semiconductor material. To treat QW potential, some ideas will be firstly presented in the simpler cases such as infinite- and finite-square well potential. Then arbitrary potential will be later described. Considered semiconductor is consisted of single quantum well with thin thickness (L_z). Electrons and holes are confined in grown direction (z-axis) and move freely in x-y plane. According to Schrodinger equation in equation (2.2), subscript i will be dropped as shown in equation (2.2),

$$\left[-\frac{\hbar^2}{2m^*} \nabla^2 + V(\vec{r}) \right] \varphi(\vec{r}) = E\varphi(\vec{r}) \quad (2.6)$$

Equation (2.6) excludes the effect of electron-hole coulomb interaction and assumed that the corresponding energy band is parabolic and non-degenerate.

II.2.1 infinite square well potential.

For Infinite Square well model as shown in fig 2.4, potential is:

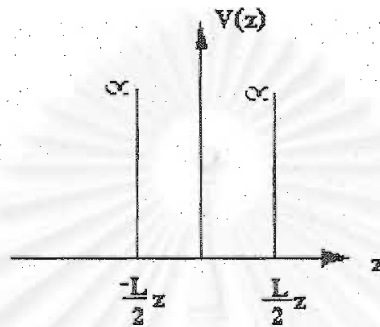


Fig 2.4 Schematic of infinite square well potential

$$V(z) = \begin{cases} 0 & \text{for } -\frac{L_z}{2} < z < \frac{L_z}{2} \\ \infty & \text{for } |z| > \frac{L_z}{2} \end{cases} \quad (2.7)$$

Wave function and periodic potential Schrodinger equation in eqn. (2.6) represents in Cartesian space.

$$\left[-\frac{\hbar^2}{2m^*} \nabla^2 + V(x, y, z) \right] \phi(x, y, z) = E\phi(x, y, z) \quad (2.8)$$

Wave function, $\phi(x, y, z)$, could be separated into $\zeta(x, y)$ and $\phi(z)$ to describe the motion of the particle in the planes of the film, and, to describe the motion of particle in the grown direction,

$$\phi(x, y, z) = \zeta(x, y) \phi(z) \quad (2.9)$$

From mathematics, ∇^2 in Cartesian space is represented,

$$\nabla^2 = \nabla_{\perp}^2 + \nabla_z^2 \quad (2.10)$$

where

$$\nabla_{\perp}^2 = \nabla_x^2 + \nabla_y^2 \quad (2.11)$$

Take equation (2.7), (2.9) and (2.10) into equation (2.8) then divide by $\zeta(x, y) \phi(z)$. As a result of this, new equation can be separated into two equations,

$$\left[-\frac{\hbar^2}{2m^*} \nabla_1^2 + V(x, y) \right] \zeta(x, y) = E_{\perp} \zeta(x, y) \quad (2.12)$$

$$\left[-\frac{\hbar^2}{2m^*} \nabla_z^2 + V(z) \right] \phi(z) = E_z \phi(z) \quad (2.13)$$

Equation (2.12) and (2.13) represents electron movement in the x-y plane and perpendicular direction, respectively. New energy eigenvalue (E) is defined to E_{\perp} and E_z . According to the structure of QW semiconductor, either electrons or holes are only confined in grown direction (z-direction), and moved freely in x-y plane. Wave function and energy eigenvalue in the x-y plane can be written as illustrated in equation (2.14) and equation (2.15), respectively. Potential of electron in grown direction is correspond to potential in equation (2.7).

$$\zeta(x, y) = C \exp[i(k_x x + k_y y)] \quad (2.14)$$

$$E_{\perp}(k) = \frac{\hbar^2}{2m^*} (k_x^2 + k_y^2) \quad (2.15)$$

where $k_x = \frac{2\pi}{L_x}$ and $k_y = \frac{2\pi}{L_y}$. Schrodinger equation in eqn. (2.13) together

with periodic potential in eqn. (2.7) is operated to obtain wave function and energy eigenvalue in confinement direction,

$$\phi(z) = A \sin k_x z + B \cos k_x z \quad (2.16)$$

where A and B are constant. Because the potential well is infinite, the particle can not move out of the well and the wave function outside the well vanishes. Since wave function has to continue everywhere, $\phi(z)$ must approach zero at the boundary.

$$\phi\left(z = \frac{L_z}{2}\right)^- = \phi\left(z = \frac{L_z}{2}\right)^+ = 0 \quad (2.17)$$

$$\phi\left(z = -\frac{L_z}{2}\right)^- = \phi\left(z = -\frac{L_z}{2}\right)^+ = 0 \quad (2.18)$$

According to continuity of current density at interface area, derivative of the wave function $\frac{1}{m^*} \frac{\partial \phi(z)}{\partial z}$ is required but it is not very important in this type of

potential well due to non-defined wave function outside the QW. Since this infinite potential well is symmetry. Wave function is satisfied symmetric conditions (as shown in equation (2.19), equation (2.20)).

$$\zeta(z) = \zeta(-z) \quad \text{for the even state} \quad (2.19)$$

$$\zeta(z) = -\zeta(-z) \quad \text{for the odd state} \quad (2.20)$$

Taking symmetric condition and continuity of current density at boundary into equation (2.16). Wave function and eigenvalue are:

For even state,

$$\phi^+(z) = \sqrt{\frac{2}{L_z}} \cos \frac{2\pi(j_e - 1/2)}{L_z} z, \quad j_e = 1, 2, 3, \dots \quad (2.21)$$

$$E_z^+ = \frac{4(j_e - 1/2)^2 \pi^2 \hbar^2}{2m_0^* L_z^2}, \quad j_e = 1, 2, 3, \dots \quad (2.22)$$

For odd state,

$$\phi^-(z) = \sqrt{\frac{2}{L_z}} \sin \frac{2\pi(j_o)}{L_z} z, \quad j_o = 1, 2, 3, \dots \quad (2.23)$$

$$E_z^- = \frac{4(j_o)^2 \pi^2 \hbar^2}{2m_0^* L_z^2}, \quad j_o = 1, 2, 3, \dots \quad (2.24)$$

As an above result, the lowest energy and state is at $j_e = 1$, even state. The next higher energy state is at $j_o = 1$ (odd state), $j_e = 2$ (even state), $j_o = 2$ (odd state) and so on. These wave functions of each state are shown in figure 2.5.

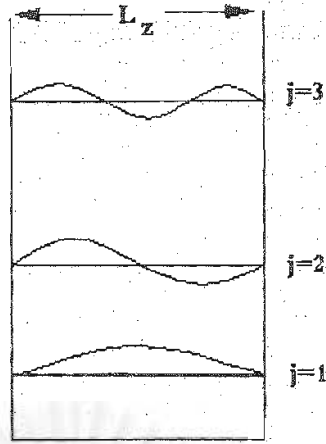


Fig 2.5 Wave function and state in infinite square well

Summing up the contributions in the x-y plane (equation (2.15)) and the z direction (equation (2.22), equation (2.24)), the total energy becomes:

$$E = \frac{\hbar^2}{2m_0^*} \left(\frac{j^2 \pi^2}{L_z^2} + k_x^2 + k_y^2 \right), \quad j = 1, 2, 3, \quad (2.25)$$

Wave function in three dimensions is,

$$\varphi(x, y, z) = C \exp[ik(k_x x + k_y y)] \left\{ \sqrt{\frac{2}{L_z}} \cos \frac{2\pi(j_e - 1/2)}{L_z} z + \sqrt{\frac{2}{L_z}} \sin \frac{2\pi(j_o)}{L_z} z \right\}$$

$$j_e \text{ and } j_o = 1, 2, 3, \dots \quad (2.26)$$

II.2.2 finite square well potential

For the time being, infinite-square well potential, the simplest potential well, was calculated. Now a bit more complicate potential well will be considered. Finite-square well potential, close to real structure of semiconductor material, is the interesting one. To treat this problem semiconductor heterostructure is consisting of a single layer of material A sandwiched in between two layers of material B, which has a larger band gap energy than that of material A. The potential well have a depth of ϕ_0 , along z direction. Electron or hole can move freely in x-y plane but is confined in z direction as infinite square-well potential in section 2.2.1. To simplify the

problem, non-degenerate state is considered. The square well potential of finite depth display in figure 2.6 and the potential define

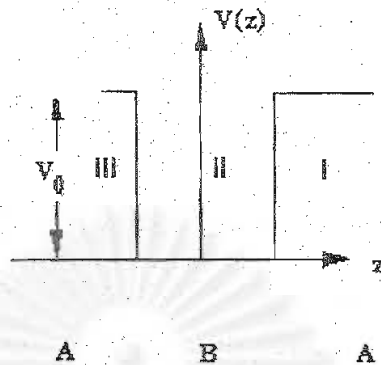


Fig 2.6 A finite-square well potential of width L_z and depth V_0

$$V(z) = \begin{cases} 0 & z \leq -\frac{L_z}{2} \\ V_0 & -\frac{L_z}{2} < z < \frac{L_z}{2} \\ 0 & z \geq \frac{L_z}{2} \end{cases} \quad (2.27)$$

To solve wave function and energy eigenvalue of finite square-well, the motion of either electrons or holes is described by a Schrodinger equation, equation (2.2).

$$\left(-\frac{\hbar^2}{2m_0^*} \nabla^2 + V(\vec{r}) \right) \varphi(\vec{r}) = E\varphi(\vec{r}) \quad (2.28)$$

where m_0^* is electron or hole effective mass and $V(\vec{r})$ is periodic potential. Also the electron and hole wave function take approximately the form

$$\varphi(\vec{r}) = \xi(x, y)\chi(z) \quad (2.29)$$

where z is the growth direction. $\xi(x, y)$ is wave function in x and y direction. and envelope wave function and $\chi(z)$ is wave function in z direction.

Substitute equation (2.29) into equation (2.28):

$$\left(\frac{\hbar^2}{2m_0^*} \nabla^2 + V(\vec{r}) \right) \xi(x, y)\chi(z) = E\xi(x, y)\chi(z) \quad (2.30)$$

let

$$\nabla^2 = \nabla_r^2 + \frac{\partial^2}{\partial z^2}, \quad \nabla_r^2 = \frac{\partial^2}{\partial x^2} + \frac{\partial^2}{\partial y^2} \quad (2.31)$$

$$E = E_r + E_z \quad (2.32)$$

Substitute equation (2.31) and equation (2.32) into equation (2.30),

$$\frac{-\hbar^2}{2m_0} \nabla_r^2 \xi(x, y) = E_r \xi(x, y) \quad (2.33)$$

$$\left(\frac{\hbar^2}{2m_0} \frac{\partial^2}{\partial z^2} + V(z) \right) \chi(z) = E_z \chi(z) \quad (2.34)$$

As a matter of fact motion of carriers in equation (2.33) is similar to those of equation (2.12). According to our previous mention electrons or holes are confined in the grown direction, z-direction, equation (2.34) is considered. From fig 2.6 potential is considered in each region. Depth of potential in region I and III are V_0 while depth of potential in region II is zero. Schrodinger equation may be written in each region as:

In region II,

$$\frac{\partial^2}{\partial z^2} \chi_{II}(z) + \frac{2m_e \varepsilon_z}{\hbar^2} \chi_{II}(z) = 0 \quad (2.35)$$

The motion of carrier in region II is described:

$$\chi_{II}(z) = A \sin k_z z + B \cos k_z z \quad (2.36)$$

$$k_z^2 = \frac{-2mE_z}{\hbar^2} \quad (2.37)$$

In region III and I,

$$\frac{\partial^2}{\partial z^2} \chi_{III,I}(z) - \frac{2m}{\hbar^2} (V_0 - E_z) \chi_{III,I}(z) = 0 \quad (2.38)$$

let

$$K_z^2 = \frac{2m}{\hbar^2} (V_0 - E_z) \quad (2.39)$$

substitute equation (2.39) into equation (2.38),

$$\frac{\partial^2}{\partial z^2} \chi_{III,I}(z) - K_z^2 \chi_{III,I}(z) = 0 \quad (2.40)$$

In our case, wave function inside the quantum well is mainly considered from equation (2.37). To solve this, wavefunction should be finite for $|z| \rightarrow \alpha$. Also the solution in region I and region III are,

Region I,

$$\chi_I(z) = C \exp(-K_z z) \quad (2.41)$$

Region III,

$$\chi_{III}(z) = D \exp(K_z z) \quad (2.42)$$

To investigate A, B, C, D parameters, we require,

(i) Symmetry of the wave functions because the potential is symmetric.

Even states,

$$\chi(z) = \chi(-z) \quad (2.43)$$

Also $C=D$ and $A=0$. Even wave function is

$$\chi^+(z) = \begin{cases} C \exp[-K_z^+ z] & z > \frac{L_z}{2} \\ B \cos[k_z^+ z] & |z| \leq \frac{L_z}{2} \\ C \exp[+K_z^+ z] & z < -\frac{L_z}{2} \end{cases} \quad (2.44)$$

Odd states,

$$\chi(z) = -\chi(-z) \quad (2.45)$$

also $C=D$ and $B=0$. Odd wave function is,

$$\chi^-(z) = \begin{cases} C \exp[-K_z^- z] & z > \frac{L_z}{2} \\ A \sin[k_z^- z] & |z| \leq \frac{L_z}{2} \\ C \exp[+K_z^- z] & z < -\frac{L_z}{2} \end{cases} \quad (2.46)$$

(ii) Continuity of the wave function.

$$\chi_{III}(z = -\frac{L_z}{2}) = \chi_{II}(z = -\frac{L_z}{2}) \quad (2.47)$$

$$\frac{\partial}{\partial z} \chi_{III}(z = -\frac{L_z}{2}) = \frac{\partial}{\partial z} \chi_{II}(z = -\frac{L_z}{2}) \quad (2.48)$$

$$\chi_{II}(z = \frac{L_z}{2}) = \chi_I(z = \frac{L_z}{2}) \quad (2.49)$$

$$\frac{\partial}{\partial z} \chi_{II}(z = \frac{L_z}{2}) = \frac{\partial}{\partial z} \chi_I(z = \frac{L_z}{2}) \quad (2.50)$$

For the even state:

From (2.47):

$$C \exp\left[K_z^+ \left(\frac{L_z}{2}\right)\right] = B \cos\left[-k_z^+ \left(\frac{L_z}{2}\right)\right]$$

(2.51)

From (2.48):

$$K_z^+ C \exp\left[K_z^+ \frac{L_z}{2}\right] = -B k_z^+ \sin\left[k_z^+ \frac{L_z}{2}\right]$$

(2.52)

$$\frac{(2.52)}{(2.51)}: \quad k_z^+ \tan\left(k_z^+ \frac{L_z}{2}\right) = K_z^+ \quad (2.53)$$

The same result can be used boundary condition in equation (2.49) and equation (2.50). Substitute k_z and K_z in equation (2.53);

$$\sqrt{\frac{2m}{\hbar^2} E_z^+} \tan\left[-\frac{L_z}{2} \sqrt{\frac{2m}{\hbar^2} E_z^+}\right] = \sqrt{\frac{2m}{\hbar^2} (V_0 - E_z^+)}$$

$$\tan\left[-L_z \sqrt{\frac{m E_z^+}{2\hbar^2}}\right] = \sqrt{\frac{V_0 - E_z^+}{E_z^+}} \quad (2.54)$$

The solution of this equation can not determine algebraically. graphical solution will use to investigate, as shown in Fig 2.7.

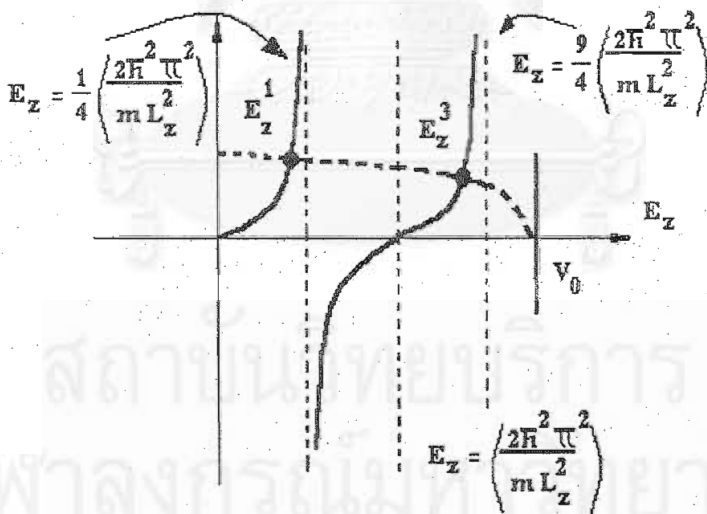


Fig 2.7 Graphical solution of equation (2.54) giving the allowed even bound-state energies. Dot line is represented the right handside of equation (2.54) and solid line is represented the left handside of equation (2.54)

The intersection of two curves is the even bound state in the quantum well. In the figure 2.7 is shown that two even bound states exist. The lowest bound-state energy is labeled E_z^1 and the higher energy is labeled E_z^3 . If the

potential energy is decreased below $\frac{2\pi^2\hbar^2}{mL_z^2}$, then number of bound state is existed only one. On the other hand, the V_0 is increased; number of bound state is more existed.

Odd states

Substitute equation (2.47), (2.48), (2.49) and (2.50) into equation (2.46)

$$A \sin \left[(k_z^-)(L_z) \right] = C \exp \left[(-K_z^-)(-\frac{L_z}{2}) \right] \quad (2.55)$$

$$Ak_z^- \cos \left[(k_z^-)(L_z) \right] = -CK_z^- \exp \left[(-K_z^-)(-\frac{L_z}{2}) \right] \quad (2.56)$$

$$\frac{(2.56)}{(2.55)}; \quad k_z^- \cot \left[k_z^- \frac{L_z}{2} \right] = -K_z^- \quad (2.57)$$

Take $k_z^-; K_z^-$ place in equation (2.57),

$$-\cot \left[L_z \sqrt{\frac{m}{2\hbar^2} \epsilon_z} \right] = \sqrt{\frac{V_0 - \epsilon_z^-}{\epsilon_z^-}} \quad (2.58)$$

To solve equation (2.58), graphical method is applied instead of algebra method, which is illustrated in Fig 2.8

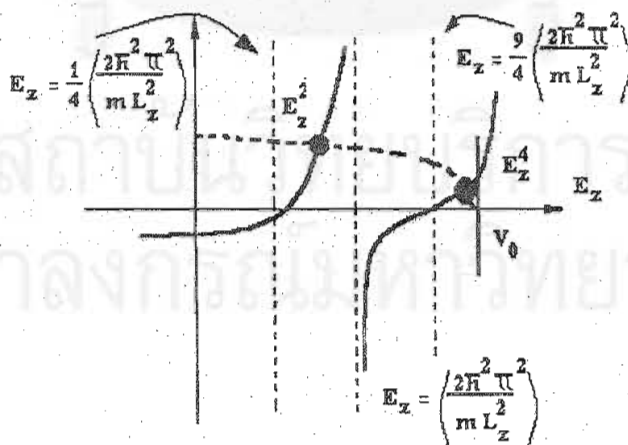


Fig 2.8 graphical solution of equation (2.58) giving the allowed odd bound-state energies. The dash line represents solution of right handside of equation (2.58) and the solid line is represent left handside of equation (2.58).

Figure 2.7 and figure 2.8 reveal the number of state that $E_z^1 < E_z^2 < E_z^3 < E_z^4$.
 From the above, the number of state is depended on V_0 .

II.2.3 Arbitrary well potential.

Now we get some idea how to get wave function and energy state of carrier by algebra and graphical method. For the arbitrary well as shown in figure 2.9 (a) is difficult to obtain wave function and energy state of carrier such as holes and electrons by algebra method. So simulating method will perform this kind of well potential. In this thesis will use stimulation created by institute of microstructural science (IMS) at national research council of Canada (NRC). This simulation is based on self-atom exchange. For example, Ga in QW -group-III atoms- will exchange only with In in barrier -group-III atoms- and As -group-V atoms- exchange with P in barrier -group-V atoms- for $\text{In}_x\text{Ga}_{1-x}\text{As}/\text{InP}$ semiconductor material as shown in figure 2.9(b). Mathematical details will be described in greater details in section 2.5.2.

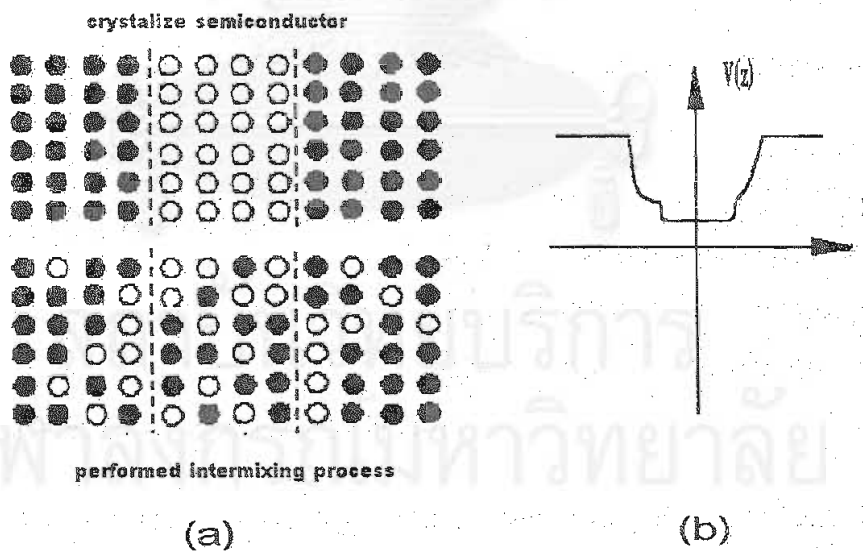


Fig 2.9 Closed and opened circles represent atoms in the QW and barrier region of crystalline semiconductor as shown above figure (a). After intermixing process is performed, those atoms exchange between interface area as shown below figure (b). This causes gradually change shape of QW potential as shown in figure (b), which is one example of arbitrary QW potential.

II.3. Direct- and indirect-gap Semiconductor.

Two main groups of semiconductors are direct- and indirect-gap semiconductor materials. When the conduction band minimum of semiconductor occurs at the same point in \bar{k} space as the valence band maximum as shown in Fig 2.10 (a), this type of material is called direct-gap semiconductors. If the minimum of the conduction band occurs at a different point in \bar{k} space than the maximum of the valence band as illustrate in Fig 2.11 (b), this material is called indirect-gap semiconductors.

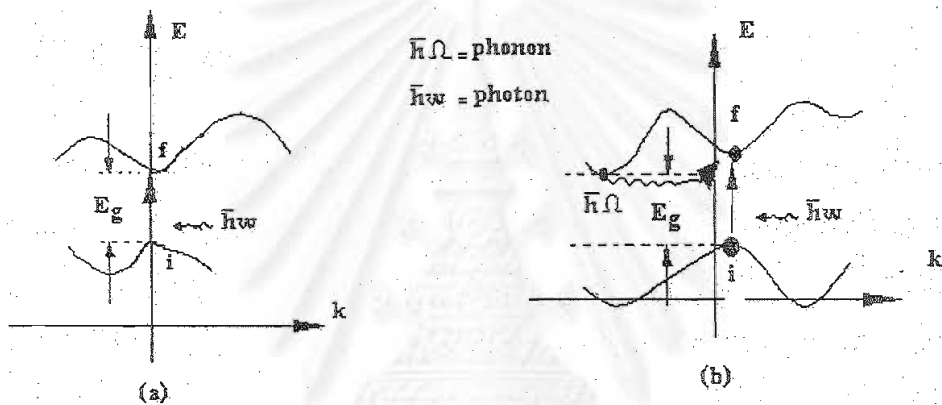


Fig 2.10 Schematic of (a) direct-gap and (b) indirect-gap semiconductors in \bar{k} space.

Conservation of momentum and energy is important rule for absorption or emissions of photons in direct- and indirect- gap semiconductor material. Direct-gap semiconductor needs only photon in absorption or emission process. On the other hand, indirect-gap semiconductor requires phonon to conserve moment and energy. It is illustrated in table 2.2.

Table 2.2 Conservation of energy and momentum of direct and indirect transition.

	Direct transition	Indirect transition
Energy conservation	$E_i + \hbar\omega = E_f$	$E_i + \hbar\omega \pm \hbar\Omega = E_f$
Momentum conservation	$\bar{k}_i + \bar{q} = \bar{k}_f$	$\bar{k}_f = \bar{k}_i + \bar{K}$

where i and f are referred to initial and final state. \bar{q} and \bar{K} are wave vector of photon and phonon, respectively. E_i and E_f are the initial and final energies of the electron. \bar{k}_i and \bar{k}_f are the initial and final wave factor of the electron, respectively. $\bar{h}\omega$ and $\bar{h}\Omega$ are then energy of photon and phonon, respectively. If the excitation energy of light is less than the QW energygap, it is absorbed as little as to QW layer. Only vertical transition between valence and conduction band is allowed. However, it is possible to have direct transition in indirect-gap semiconductor at higher photon energies than the indirect transitions.

II.4.Recombination

The operation of almost all opto-electronic devices is based on the creation and annihilation of electron-hole pairs. The simplest way to create electron-hole pair is to irradiate the semiconductor compound with photon having sufficient energy. Energy of photon should be greater than energy gap between conduction and valence band. The photon will impart its energy to the carrier in the valence band (electron) and raise them to the conduction band. This process is called 'Absorption'. The reversed process, that of electron- and hole- recombination, is associated with the pair giving up its excess energy. This process is called 'recombination process'. Recombination process can classify to radiative and non-radiative recombination. Radiative recombination is occurred because photons are emitted during recombination process. On the other hand, non-radiative recombination process doesn't emit photons. In this section, results of recombination in direct and indirect band-to-band recombination as previously illustrated in section II.4.1 and subsequently examined effect of non-radiative centers on the lifetime in section II.4.2.

II.4.1 Recombination process

In equilibrium semiconductor without any incident photon or injection of electron, the carrier densities can be calculated from equilibrium fermi level. When excess carriers are created, non-equilibrium conditions are generated. One can define non-equilibrium distribution function for electrons ($f_n(E)$) and for holes ($f_p(E)$) by using fermi-direct distribution as,

$$f_n(E) = \frac{1}{1 + \exp\left(\frac{E - E_{fn}}{k_B T}\right)} \quad (2.59)$$

$$f_p(E) = \frac{1}{1 + \exp\left(\frac{E - E_{fp}}{k_B T}\right)} \quad (2.60)$$

These distribution functions define E_{fn} and E_{fp} are the quasi-fermi levels for electrons and holes, respectively. k_B is Boltzman constant and T is temperature. While excess carriers are created, those carriers are recombined and photon is emitted. New equilibrium is generated and quasi-fermi levels can be represented as $E_{fn} = E_{fp} = E_f$. The difference ($E_{fn} - E_{fp}$) is a measurement of the derivation from equilibrium. If $\exp\left[\frac{E - E_{fn}}{k_B T}\right]$ and

$\exp\left[\frac{E - E_{fp}}{k_B T}\right]$ are extremely greater than one, fermi-direct distribution function will be,

$$f_n(E) \cong \exp\left[\frac{E_{fn} - E}{k_B T}\right] \quad (2.61)$$

$$f_p(E) \cong \exp\left[\frac{E - E_{fp}}{k_B T}\right] \quad (2.62)$$

and the non-equilibrium carrier concentrations of electrons (n) and holes (p) are given by,

$$n = N_c \exp \left[\frac{E_{fn} - E_c}{k_B T} \right] \quad (2.63)$$

$$p = N_v \exp \left[\frac{E_v - E_{fp}}{k_B T} \right] \quad (2.64)$$

Since the concepts of quasi-fermi level provide a means to take into account changes of carrier concentration as a function of position in a semiconductor. For example, it is assumed that an n-type semiconductor with an equilibrium electron density, n_0 , is uniformly irradiated with intrinsic photoexcitation (above band gap lights). So as to produce electron-hole pairs (Δn) with a generation rate, G . The non-equilibrium electron (n) and hole (p) concentrations are given by,

$$n = \Delta n + n_0 \quad (2.65)$$

$$p = \Delta n + \frac{n_i^2}{n_0} \quad (2.66)$$

The density of excess carriers created in a semiconductor is eventually recombined until reach equilibrium or steady state. Condition of equilibrium state is that recombination rate (R) equal to the generation rate,

$$G = R \quad (2.67)$$

Generation and recombination processes involved transition of carrier across the energy bandgap can be referred to obtain carrier-lifetime of either direct or indirect bandgap semiconductors. In order to simply examine recombination and carrier lifetime, band-to-band recombination structure is considered here. Direct band-to-band recombination is firstly illustrated in section II.4.1.1 and subsequently indirect band-to-band recombination in section II.4.1.2.

II.4.1.1 Direct band-to-band recombination.

Recombination of electron-hole pairs in direct semiconductor is happened at the valence band maximum and the conduction band minimum occur in the zone center ($\bar{k} = 0$) and does not require a change in momentum or

the involvement of a phonon as shown in figure 2.11. In order to obtain recombination rate and carrier lifetime, the one-electron approximation and $E - \bar{k}$ relation in both the conduction and valence bands is required. Wave

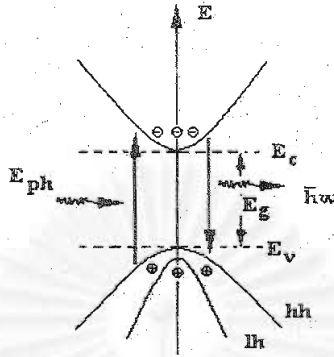


Fig 2.11 Illustration of band-to band of absorption and recombination process in direct-gap semiconductor

function in equation (2.1) can be rewritten in matrix from,

$$\psi(\vec{r}) = \mu(\vec{r})\phi(\vec{r}) = |n, \vec{k}\rangle$$

where n indicate to wave function in either conduction or valence band. In the present case, the upper state $|2\rangle$ belongs to the conduction band. Writing $|c\vec{k}_2\rangle$ for $|2\rangle$ and noting that the state functions are described by one particle block functions appropriate for the conduction band,

$$|2\rangle = |c, \vec{k}_c\rangle = U_c(\vec{r})\exp[i\vec{k}_c \cdot \vec{r}] \quad (2.68)$$

Similarly, the wave function for the lower state $|1\rangle$ is that for a valence band, hole.

$$|1\rangle = |v, \vec{k}_h\rangle = U_v(\vec{r})\exp[i\vec{k}_h \cdot \vec{r}] \quad (2.69)$$

Where $U_v(\vec{r})$ and $U_c(\vec{r})$ are the cell-periodic parts of the wave functions having, respectively, P-like and S-like atomic character it is assumed that a valence band electron of wave vector \vec{k}_h is taken to a conduction band state of wave vector \vec{k}_c via the absorption of a photon of wave vector \vec{k}_λ . The spontaneous emission rate for transition between two states $|2\rangle$ and $|1\rangle$ is expressed,

$$R_{sp}(\bar{h}\omega) = \frac{2\pi}{\bar{h}} \left(\frac{eA_0}{m_0} \right)^2 \sum_{1,2} \langle |p_{12}|^2 \rangle G(\bar{h}\omega) f_2 (1-f_1) \delta(E_{12} - \bar{h}\omega) \quad (2.70)$$

Where $A_0 = \left(\frac{\bar{h}}{2\varepsilon_0 \eta^2 v \omega} \right)^{\frac{1}{2}}$, m_0 is electron mass in free space. e is electron charge. η is refractive index of semiconductor material and V is volume. $G(\bar{h}\omega)$ is optical density of states, $G(\bar{h}\omega) = \frac{\eta^3 (\bar{h}\omega)^2}{\pi^2 c^3 \bar{h}^3}$. f_2 is probability. Now we can obtain

$$\begin{aligned} p_{12} &= \langle c\bar{k}_2 / \exp(i\bar{k} \cdot \bar{r}) \bar{E}_\lambda \cdot \bar{p} / v\bar{k}_h \rangle \\ &= \int_{crystal} U_c^*(\bar{k}_e, \bar{r}) \exp[-i\bar{k}_e \cdot \bar{r}] \exp[i\bar{k}_\lambda \cdot \bar{r}] \bar{E}_\lambda \cdot \bar{p} U_v(\bar{k}_h, \bar{r}) \exp[i\bar{k}_h \cdot \bar{r}] d^3\bar{r} \quad (2.71) \end{aligned}$$

The integration over the whole crystal volume is first divided into partial integration over the individual unit cells. The contribution from each cell is estimated by noting the nature of wave function as shown in Fig 2.12. A schematic representation of the electronic wave function in one dimension is shown in Fig2.12 (b) while the periodic potential is shown in fig 2.12(a). The eigenstate is the product of the cell-periodic part U_k shown in Fig 2.12(c) and of a plane wave $\exp[i\bar{k} \cdot \bar{r}]$ as in Fig 2.12(d). The cell-periodic part is rapidly varying and has appreciable values only near the core of the atom. On the contrary, the plane waves are slowly varying many unit cells since \bar{k} is small. Thus in evaluating the integral expressed by equation (2.72) over the ℓ^{th} unit cell, the exponential function are replaced by $\exp[i\bar{k} \cdot \bar{R}_\ell]$ where \bar{R}_ℓ is the position vector of the ℓ^{th} cell, and are taken outside the integral. Equation (2.71) can be rewritten as,

$$p_{12} = \int_{cell} U_c^*(\bar{k}_e, \bar{r}) \bar{E}_\lambda \cdot [\bar{p} U_v(\bar{k}_h, \bar{r}) + i\bar{h} (i\bar{k}_h) U_v(\bar{k}_h, \bar{r})] d^3\bar{r} \sum_{\ell} \exp[i(\bar{k}_h + \bar{k}_\lambda - \bar{k}_e) \cdot \bar{R}_\ell] \quad (2.72)$$

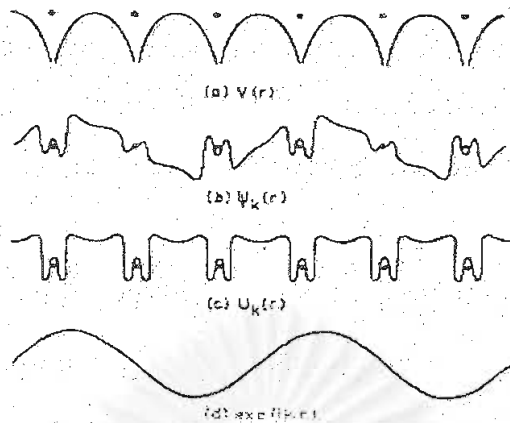


Fig 2.12 Schematic representation of Bloch functions in semiconductors (a) periodic potential, (b) full wave function, (c) cell-periodic part $U_{\vec{k}}$ and (d) plane wave part.

The last sum in equation (2.72) is non-zero when

$$\vec{k}_h + \vec{k}_\lambda - \vec{k}_e = N\vec{K}_m, \quad N = 0, 1, 2, \dots \quad (2.73)$$

Where N is an integer and \vec{K}_m is a reciprocal lattice vector. Since both \vec{k}_h and \vec{k}_e lie in the first Brillouin zone, the conditions for conservation of wave number (or momentum) for the electrons represents,

$$\vec{k}_e = \vec{k}_h + \vec{k}_\lambda \quad (2.74)$$

According to the wave vector \vec{k}_λ associated with the photon is small compared to both \vec{k}_e and \vec{k}_h . Therefore, to a good approximation, we may write $\vec{k}_\lambda = 0$ and express the conservation as

$$\vec{k}_e = \vec{k}_h \quad (2.75)$$

Equation (2.72) can be rewritten as,

$$\begin{aligned} p_{12} &= \delta_{\vec{k}_e, \vec{k}_h} \int_{cell} U_c^*(\vec{k}_e, \vec{r}) \vec{E}_\lambda \cdot \vec{p} U_v(\vec{k}_h, \vec{r}) d^3\vec{r} + \delta_{\vec{k}_e, \vec{k}_h} \frac{\hbar}{i} \vec{E}_\lambda \cdot \vec{k}_e \int U_c^*(\vec{k}_e, \vec{r}) U_v(\vec{k}_h, \vec{r}) d^3\vec{r} \\ &= \delta_{\vec{k}_e, \vec{k}_h} \left[p_{cv}^a + i\vec{E}_\lambda \cdot \vec{k}_e p_{cv}^f \right] \end{aligned} \quad (2.76)$$

Where \vec{k} -conservation has been assumed to be valid. Now, the orthogonality of U_c and U_v at $\vec{k} = 0$ makes the second term in equation (2.76) equal to zero.

$$p_{12} = \delta_{\bar{k}_e, \bar{k}_h} p_{cv}^a = \delta_{\bar{k}_e, \bar{k}_h} \int_{\text{cell}} U_c^*(\bar{k}_e, \bar{r}) \bar{E}_\lambda \cdot \bar{p} U_v(\bar{k}_h, \bar{r}) d^3\bar{r} \quad (2.77)$$

In equation (2.76), the superscripts a and f refer, respectively to "allowed" and "forbidden" transitions. Under the usual circumstances, the allowed transitions out weigh the forbidden ones. However, when, due to symmetry, the conditions p_{cv}^a vanish, the second term determines the transition probability. Since the wave functions corresponding to light hole and split-off valence bands contain admixture S-like wave functions for $\bar{k} = 0$, there is thus a non-zero contribution to the optical matrix element that is proportional to \bar{k} . The spontaneous emission rate in equation (2.70) can be expressed for allowed transition as

$$R_{sp} = \frac{2\pi}{\hbar} \left(\frac{eA_0}{m_0} \right)^2 \sum_{\bar{k}_e, \bar{k}_h} \langle |\bar{p}_{cv}|^2 \rangle \delta_{\bar{k}_e, \bar{k}_h} G(\hbar\omega) f_e(\bar{k}_e) f_h'(\bar{k}_h) \delta[E_c(\bar{k}_e) - E_v(\bar{k}_h) - \hbar\omega] \quad (2.78)$$

$\langle |\bar{p}_{cv}|^2 \rangle$ term is the average value of the squared momentum matrix element and the light wave assume to have random polarization. $f_h'(\bar{k}_h)$ is the empty state. The distribution functions f_e and f_h is, in general, expressed by fermi distributions, with respective quasi-fermi levels. In the following, we shall assume that the quasi-fermi levels for electrons and holes are away from the respective band edges by more than $k_B T$, so that they may be expressed by Boltzman distributions as follows,

$$f_e(\bar{k}_h) = \exp \left[- \frac{E_c(\bar{k}_h) - F_e}{k_B T} \right] \quad (2.79)$$

$$f_h(\bar{k}_h) = \exp \left[\frac{E_v(\bar{k}_h) - F_h}{k_B T} \right] \quad (2.80)$$

Writing $\Delta F = F_e - F_h$ and noting that $E_c(\bar{k}_h) - E_v(\bar{k}_h) = \hbar\omega$, we may obtain

$$f_e(\bar{k}_h) f_h'(\bar{k}_h) = \exp \left[- \frac{\hbar\omega - E_g}{k_B T} \right] \exp \left[- \frac{E_g - \Delta F}{k_B T} \right] \quad (2.81)$$

substitute equation (2.81) into equation (2.78)

$$R_{sp}(\hbar\omega) = C(\hbar\omega, T) \exp \left[- \frac{(E_g - \Delta F)}{k_B T} \right] (\mu_{hh})^{\frac{3}{2}} (\hbar\omega - E_g)^{\frac{1}{2}} \exp \left[- \frac{(\hbar\omega - E_g)}{k_B T} \right] \quad (2.82)$$

where μ_{hh} indicates the reduced mass involving conduction (c) band and hh valence band effective masses.

$$C(\bar{h}\omega, T) = \frac{e^2 \eta \bar{h} \omega \langle |p_{cv}|^2 \rangle}{2\pi^3 c^3 m_0^2 \epsilon_0 \bar{h}^2} \left(\frac{2}{\bar{h}^2} \right)^{\frac{3}{2}} \quad (2.83)$$

According to quasi-fermi levels are related to the electron and hole densities n and p , respectively.

$$n = 2 \left(\frac{m_e k_B T}{2\pi \bar{h}^2} \right)^{\frac{3}{2}} \exp \left[-\frac{E_g - F_e}{k_B T} \right] \quad (2.84)$$

$$p = 2 \left(\frac{m_{hh} k_B T}{2\pi \bar{h}^2} \right)^{\frac{3}{2}} \exp \left[\frac{-F_h}{k_B T} \right] \quad (2.85)$$

The production of n and p ,

$$np = 4 \left(\frac{k_B T}{2\pi \bar{h}^2} \right)^3 m_e^{\frac{3}{2}} m_{hh}^{\frac{3}{2}} \exp \left[-\frac{E_g - \Delta F}{k_B T} \right]$$

$$\exp \left[-\frac{E_g - \Delta F}{k_B T} \right] = \frac{np}{4 \left(\frac{k_B T}{2\pi \bar{h}^2} \right)^3 m_e^{\frac{3}{2}} m_{hh}^{\frac{3}{2}}} \quad (2.86)$$

Substitute equation (2.86) to equation (2.82);

$$R_{sp}(\bar{h}\omega) = \left[\frac{2\pi}{(\pi k_B T)^{\frac{3}{2}}} \right] C(\bar{h}\omega, T) np \left[\frac{\mu_{hh}}{m_e m_{hh}} \right]^{\frac{3}{2}} (\bar{h}\omega - E_g)^{\frac{1}{2}} \exp \left[-\frac{(\bar{h}\omega - E_g)}{k_B T} \right] \quad (2.87)$$

Where

$$C(\bar{h}\omega, T) = \frac{e^2 \eta \bar{h} \omega}{2\pi c^3 m_0^2 \epsilon_0 \bar{h}^2} \left(\frac{2\pi \bar{h}^2}{k_B T} \right)^{\frac{3}{2}} \langle |p_{cv}|^2 \rangle \quad (2.88)$$

The total spontaneous emission rate is obtained by integrating $R_{sp}(\bar{h}\omega)$ over all photon energies. For this purpose $C(\bar{h}\omega, T)$ is assumed to be sufficiently slow varying to be approximated by a constant over the region where

$(\bar{h}\omega - E_g)^{\frac{1}{2}} \exp \left[-\frac{(\bar{h}\omega - E_g)}{k_B T} \right]$ is appreciable. The required integral is of the

form $\int_0^a x^{\frac{1}{2}} e^{-x} dx = \sqrt{\frac{\pi}{2}}$. Thus,

$$R_{sp} = \int_0^a R_{sp}(\bar{h}\omega) d\bar{h}\omega$$

$$= npC \left(\hbar \omega, T \right) \left(\frac{1}{m_e + m_{hh}} \right)^{\frac{3}{2}} \quad (2.89)$$

Now we are already known band-to-band recombination rate in case of excess carriers from equation (2.89).

Next question in our mind is how recombination rate can be referred to carrier lifetime. Here we will previously shown this at equilibrium state by using equation (2.67) and subsequently observe lifetime of excess carriers. At Equilibrium State, the generating rate (G) equals to the recombination rate (R_{sp}^0) is proportional to the product of thermal equilibrium value of electron and hole density ($n_0 p_0$):

$$G = R_{sp}^0 = B_r n_0 p_0 \quad (2.90)$$

where B_r is proportionality constant. When excess carriers decay, the instantaneous electron density obeys the rate equation

$$\frac{dn}{dt} = -R_{sp} + G = -B_r (np - n_0 p_0) \quad (2.91)$$

writing $n = n_0 + \delta n$, $p = p_0 + \delta p$, and noting that $\delta n = \delta p$, we obtain

$$\frac{d}{dt} \delta n = -B_r (n_0 + p_0 + \delta n) \delta n = -\frac{1}{\tau_r} \delta n \quad (2.92)$$

The solution is,

$$\delta n(t) = \Delta n \exp\left(-\frac{t}{\tau_r}\right) \quad (2.93)$$

where Δn is the initial excess electron concentration and τ_r is the lifetime of excess electron given by

$$\tau_r = [B_r (n_0 + p_0 + \delta n)]^{-1} \quad (2.94)$$

At low injection levels, δn may be neglected, so that the lifetime is given by

$$\tau_r = [B_r (n_0 + p_0)]^{-1} \quad (2.95)$$

Equation (2.90) can rewrite by dropping the "0" index,

$$B_r = \frac{R_{sp}}{np} \quad (2.96)$$

According to equation (2.89) and (2.96), radiative excess-carrier lifetime of band-to-band recombination is,

$$B_r = \frac{R_{sp}}{np} = C(\bar{h}\omega, T) \left(\frac{1}{m_e + m_{hh}} \right)^{\frac{3}{2}}$$

$$= \frac{e^2 \eta \bar{h} \omega}{2\pi^3 m_0^2 \epsilon_0 \bar{h}^2} \left(\frac{2\pi \bar{h}^2}{k_B T} \right)^{\frac{3}{2}} \langle |p_{cv}|^2 \rangle \left(\frac{1}{m_e + m_{hh}} \right)^{\frac{3}{2}} \quad (2.97)$$

and

$$\frac{1}{\tau_r} = (n_0 + p_0) \left\{ \frac{e^2 \eta \bar{h} \omega}{2\pi^3 m_0^2 \epsilon_0 \bar{h}^2} \left(\frac{2\pi \bar{h}^2}{k_B T} \right)^{\frac{3}{2}} \langle |p_{cv}|^2 \rangle \left(\frac{1}{m_e + m_{hh}} \right)^{\frac{3}{2}} \right\} \quad (2.98)$$

To sum up, we found that an electron raised to the conduction band by photon absorption in direct bandgap semiconductor material dwell there for a very short time and recombine again with holes in the valence band to emit light of energy equal to bandgap. So the probability of radiative recombination is very high in direct-gap semiconductor material.

II.4.1.2 Indirect band-to-band recombination.

Absorption and recombination in indirect-gap semiconductors are quite different from those process in direct-gap semiconductors because the conduction band minima or valence band maxima are not at $\bar{k} = 0$ as shown in fig 2.13 and require a change in momentum or the involvement of a phonon.

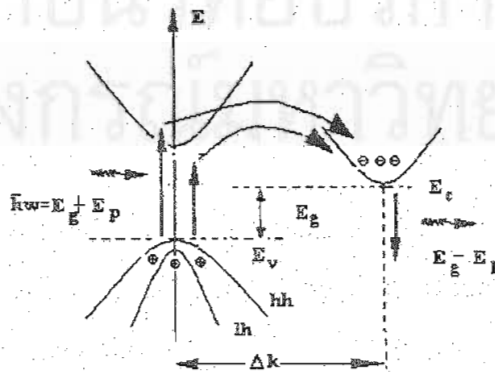


Fig 2.13 Illustration of band-to band of absorption and recombination process in indirect-gap semiconductor.

Thus an electron dwelling in the conduction band minimum at $\bar{k} \neq 0$ can not directly recombine with a hole at $\bar{k} = 0$ until a phonon with the right energy and momentum is available. So recombination of electron and hole in an indirect gap semiconductor is composed of two-step process. First-step process is that photon required is for conservation of energy in the $E - \bar{k}$ diagram. Second-step process is that phonon required for conservation of momentum and electron to land in the indirect conduction band. Therefore, the transition for recombination of electron-hole pair is given by second-order perturbation theory as shown,

$$r_2(\bar{k}) = \frac{2\pi}{\hbar} \sum_f \sum_n \left\{ \frac{|\langle f | H | n \rangle|^2 |\langle n | H | i \rangle|^2}{E_i - E_n} \right\} \delta(E_f - E_i) \quad (2.99)$$

where H is the perturbation term of photon (H_{cv}) and phonon (H_{ep}) in schrodinger equation, $H = H_{cv} + H_{ep}$. $|i\rangle, |f\rangle$ and $|n\rangle$ are initial, final and intermediate state, respectively. According to equation (2.78) and (2.99), spontaneous emission rate at photon energy ($\hbar\omega$) in an indirect gap semiconductor occurred between one the equivalent conduction band minima at \bar{k}_0 and the valence band maximum at $\bar{k} = 0$ via phonon participation is,

$$R_{sp}(\hbar\omega) = \frac{2\pi}{\hbar} G(\hbar\omega) \sum_{E_v, E_c} |H_{cv}^2|^2 \int \left\{ (\bar{n}_q + 1) \exp\left[-\frac{(E_v - E_c - \Delta F)}{k_B T}\right] \delta(E_v - E_c + \hbar\omega + k_B \theta) \right. \\ \left. + n_q \exp\left[-\frac{(E_v - E_c - \Delta F)}{k_B T}\right] \delta(E_v - E_c + \hbar\omega - k_B \theta) \right\} \rho_c(E_c) \rho_v(E_v) dE_c dE_v \quad (2.100)$$

where $f, f_h = \exp\left[-\frac{E_c - E_v - \Delta F}{k_B T}\right]$ and the second-order matrix element involving the radiation field and the phonon field as perturbation. Details of this examination can see in book written by P.K. Basu[25]. This equation is included a summation over the intermediate states. $\rho_c(E_c)$ is density-of-states functions for the conduction band,

$$\rho_c(E_c) = \sum_{c=1}^{N_c} \frac{m_L^{1/2} m_T}{(2\pi)^2} \left(\frac{2}{\hbar^2} \right)^{3/2} (E_c - E_g)^{1/2} \quad (2.101)$$

where N_c is the number of equivalent minima, m_L and m_T is isotropic effective mass in conduction band. $\rho_v(E_v)$ is valence band density-of-states function,

$$\rho_v(E_v) = \sum_{v=h,\ell} \left(\frac{2m_v}{\hbar^2} \right)^{3/2} (E_v)^{1/2} \quad (2.102)$$

where m_v = isotropic effective mass in valence band

$$G(\bar{h}\omega) = \frac{\eta^2 (\bar{h}\omega)^2}{(\pi c)^2 \bar{h}^3 \left(\frac{c}{n} \right)} \quad (2.103)$$

$$|H_{cv}^2|^2 = \frac{e^2 \bar{h}}{2\epsilon m_0^2 \omega} \langle |p_{cv}^2|^2 \rangle \quad (2.104)$$

$\langle |p_{cv}^2|^2 \rangle$ is the product of,

1. the averaged momentum matrix element for optical transitions between $\bar{k} = 0$ states.
2. The matrix element for transitions from $|c\bar{k}_0\rangle$ states to $|m\bar{k}_0\rangle$ states by phonon or other agents.
3. The inverse of the energy difference between intermediate (m) states and initial (i) states.

Substitute equation (2.101), (2.102), (2.103), (2.104) into equation (2.100),

$$\begin{aligned} R_{sp}(\bar{h}\omega) &= \frac{2\pi}{\hbar} \frac{\eta^2 (\bar{h}\omega)^2}{(\pi c)^2 \bar{h}^3 \left(\frac{c}{n} \right)} \sum \frac{e^2 \bar{h}}{2\epsilon m_0^2 \omega} \langle |p_{cv}^2|^2 \rangle \int \int_{E_v, E_c} \left\{ (\bar{n}_q + 1) \exp \left[-\frac{(E_v - E_c - \Delta F)}{k_B T} \right] \right\} \\ &\quad \times \delta(E_v - E_c + \bar{h}\omega + k_B \theta) + n_q \exp \left[-\frac{(E_v - E_c - \Delta F)}{k_B T} \right] \delta(E_v - E_c + \bar{h}\omega + k_B \theta) \\ &\quad \times \sum_{c=1}^{N_c} \frac{m_L^{1/2} m_T}{(2\pi)^2} \left(\frac{2}{\hbar^2} \right)^{3/2} (E_c - E_g)^{1/2} \sum_{v=h,\ell} \left(\frac{2m_v}{\hbar^2} \right)^{3/2} (E_v)^{1/2} dE_c dE_v \end{aligned} \quad (2.105)$$

using this relation,

$$\sum_{c=1}^{N_c} \frac{\left(m_L^{1/2} m_T\right)}{(2\pi)^2} \left(\frac{2}{\hbar^2}\right)^{3/2} \sum_{v=h\hbar, \ell\hbar} \frac{1}{(2\pi)^2} \exp\left[\frac{E_g - \Delta F}{k_B T}\right] = \frac{np}{\pi(k_B T)^3} \quad (2.106)$$

and

$$\int_{E_c, E_v} \int \exp\left[-\frac{(E_c - E_v - \Delta F)}{k_B T}\right] (E_c - E_g)^{1/2} E_v^{1/2} \delta(E_v - E_c + \hbar\omega + k_B\theta) dE_v dE_c \\ = \frac{\pi}{8} (\hbar\omega + k_B\theta - E_g)^2 \exp\left[-\frac{(\hbar\omega + k_B\theta - \Delta F)}{k_B T}\right] \quad (2.107)$$

$$R_{sp}(\hbar\omega) = np \left(\frac{2e^2}{4\pi\epsilon_0 \hbar c}\right) \left(\frac{1}{\hbar c^2 m_0^2}\right) \left[\left\langle |p_{cv}^{(2)}|^2 \right\rangle n\hbar\omega\right] \frac{1}{2} \frac{1}{(k_B T)^3} \\ \times \left\{ \sum_{c=1}^{N_c} \frac{\left(m_L^{1/2} m_T\right)}{4\pi^2} \left[\frac{2}{\hbar^2}\right]^{3/2} \sum_{v=h, \ell} \left[\frac{2m_v}{\hbar^2}\right]^{3/2} \right\} \exp\left[-\frac{E_g - \Delta F}{k_B T}\right] \\ \times \left\{ \frac{(\hbar\omega + k_B\theta - E_g)^2}{\left[1 - \exp\left(\frac{-\theta}{T}\right)\right]} \exp\left[-\frac{(\hbar\omega + k_B\theta - E_g)}{k_B T}\right] + \frac{(\hbar\omega - k_B\theta - E_g)^2}{\left[\exp\left(\frac{\theta}{T}\right) - 1\right]} \exp\left[-\frac{(\hbar\omega - k_B\theta - E_g)}{k_B T}\right] \right\} \quad (2.108)$$

The total spontaneous emission rate R_{sp} may be obtained by integral R_{sp} in equation (2.108) over all photon energies. Similarly, carrier lifetime of indirect band-to-band recombination can be obtained by using equation (2.95) (2.96) and (2.108) as shown,

$$\frac{1}{\tau} = (n_0 + p_0 + \delta n_0) \left(\frac{e^2}{2\pi\epsilon_0 \hbar^2 c^3 m_0^2}\right) \left\langle |p_{CB}^{(2)}|^2 \right\rangle n\hbar\omega \frac{\exp\left[\frac{\theta}{T}\right] + 1}{\exp\left[\frac{\theta}{T}\right] - 1} \quad (2.109)$$

As a result of carrier lifetime of direct and indirect band-to-band recombination, it is evidence that radiative lifetime in the direct band-to-band recombination is shorter than that of the indirect band-to-band recombination because phonons is required in indirect band-to-band recombination in order to keep conservation of momentum. Furthermore, the possibility of radiative recombination is very high in direct semiconductors. The competing non-

radiative process reduces the probability of radiative recombination in indirect semiconductors.

II.4.2 Effect of non-radiative centers on the lifetime.

Generally defects can be naturally introduced in semiconductor material during the growth process or possibly introduced after growth. These introduced defects can be impurity atoms, vacancy lattice, substitutional and interstitial impurity atoms, anti-site atoms and other imperfections. Defects naturally created during growth process possibly combine together and become neutral atoms. For example, interstitial atoms fall into vacancy site. If defects introduced after growth process have enough kinetic energy, it will recombine non-radiatively with exciton. Intermediate energy level in figure 2.14 can be trap or non-recombination-center state.

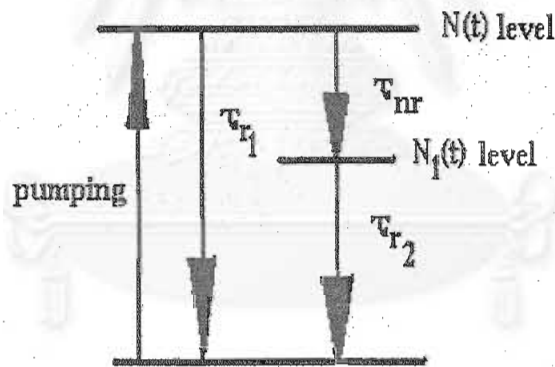


Fig 2.14 Band diagram of impurity semiconductor material, which intermediate state represents either non-radiative recombination center or trap state with the number of defects as $N_1(t)$. The number of carriers in the conduction band is denoted by $N(t)$.

In figure 2.14, electrons in conduction band possibly recombine with hole in valence band in two channels. First channel is that electrons are directly recombined with holes in valence band by radiative lifetime, τ_r . Second channel is that electrons are recombined with holes in valence band through

intermediate state, $N_1(t)$. This recombination process will involve both non-radiative (τ_{nr}) and radiative (τ_r). So evolution of $N(t)$ as a function of time is performed to obtain radiative and non-radiative lifetime,

$$\frac{dN(t)}{dt} = -\frac{N(t)}{\tau_r} - \frac{N(t)}{\tau_{nr}} \quad (2.110)$$

This equation is assumed that excess carriers are generated N_0 at the beginning time ($t = 0$). To solve number of excess carriers in conduction band, integration is operated to both size,

$$\int \frac{dN(t)}{N(t)} = \int -\left(\frac{1}{\tau_r} + \frac{1}{\tau_{nr}}\right) dt \quad (2.111)$$

$$N(t) = C \exp\left[-\left(\frac{1}{\tau_r} + \frac{1}{\tau_{nr}}\right)t\right] \quad (2.112)$$

Take initial condition, $N(t = 0) = N_0$, to (2.112)

$$N(t) = N_0 \exp\left[-\left(\frac{1}{\tau_r} + \frac{1}{\tau_{nr}}\right)t\right] \quad (2.113)$$

According to relation of intensity,

$$I(t) = \frac{N(t)}{\tau_{r1}} \quad (2.114)$$

so,

$$I(t) = \frac{N_0}{\tau_{r1}} \exp\left[-\left(\frac{1}{\tau_r} + \frac{1}{\tau_{nr}}\right)t\right] \quad (2.115)$$

Intensity in equation (2.115) is plotted as a function of time as shown in figure 2.15. Number of excess carrier (N_0) is assumed to 1×10^{24} atoms/cm³ at beginning time ($t = 0$). Slope of graph indicates the combination of both radiative and non-radiative recombination rate as shown in equation (2.116).

$$\frac{1}{\tau_m} = \frac{1}{\tau_r} + \frac{1}{\tau_{nr}} \quad (2.116)$$

where τ_m is measured lifetime. This lifetime can observed from slope of graph. τ_r and τ_{nr} are radiative and non-radiative lifetime (refer to lifetime in

figure 2.14). According to equation (2.116), radiative lifetime is much longer than non-radiative lifetime, measured lifetime will be short. Oppositely if non-radiative lifetime is dominant, measured lifetime is long.

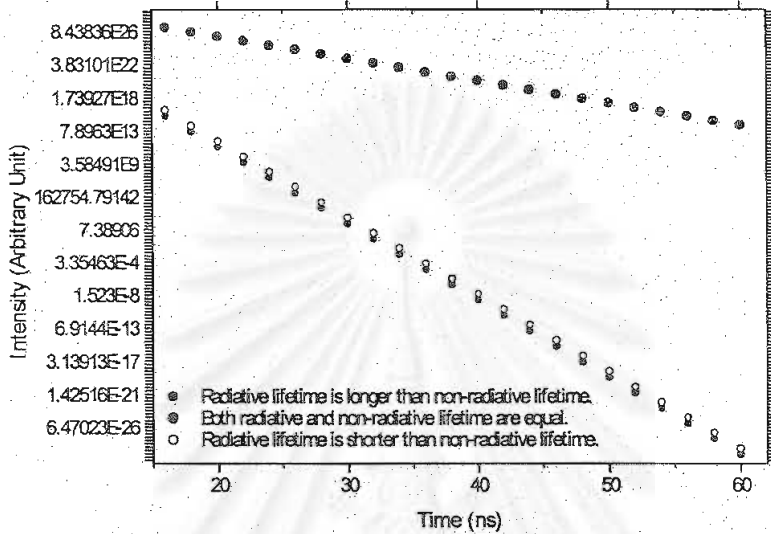


Fig 2.15 Schematic of intensity as a function of time. Number of carriers at beginning time is 1×10^{24} atoms/cm³.

This kind of recombination can be found from two independent populations that corresponds to three conditions: 1-two populations of carriers isolated from each other, 2- each carrier population emits at the same energy, and 3- each carrier population has a different lifetime. For example, two QWs are grown on the same sample but first and second QW have different composition and well width. Those two QWs are emitted photon at the same energy and different lifetime.

Furthermore, Concentrations of carriers ($N_1(t)$) in intermediate state in figure 2.14 states can be determined by relation in equation (2.117) occurs from defects in the crystalline semiconductors is examined,

$$\frac{dN_1(t)}{dt} = \frac{N(t)}{\tau_{nr}} - \frac{N_1(t)}{\tau_{r_2}} \quad (2.117)$$

To obtain $N_1(t)$, we will assume,

$$N_1(t) = C \exp \left[-\frac{t}{\tau_{nr}} \right] + f(t) \quad (2.118)$$

where C is constant

Derivative of equation (2.118),

$$\frac{dN_1(t)}{dt} = -\frac{C}{\tau_{nr}} \exp \left[-\frac{t}{\tau_{nr}} \right] + \frac{df(t)}{dt}$$

Substitute equation (2.118) and derivation of equation (2.118) into equation (2.117),

$$\frac{df(t)}{dt} + \frac{f(t)}{\tau_{r_2}} = \frac{N(t)}{\tau_{nr}} + C \left(\frac{1}{\tau_{nr}} - \frac{1}{\tau_{r_2}} \right) \exp \left[-\frac{t}{\tau_{nr}} \right] \quad (2.119)$$

If we set the right of equation is zero,

$$C = \frac{-\frac{N_0}{\tau_{nr}} \exp \left[-\frac{1}{\tau_{r_1}} \right]}{\frac{1}{\tau_{nr}} - \frac{1}{\tau_{r_2}}} \quad (2.120)$$

On the left of equation is,

$$\frac{df(t)}{dt} + \frac{f(t)}{\tau_{r_2}} = 0$$

$$f(t) = C' \exp \left[-\frac{t}{\tau_{r_2}} \right] \quad (2.121)$$

According to initial condition, $N(t=0) = N_0$. Take this initial condition to equation (2.118),

$$N_1(t=0) = C + f(t=0) \quad (2.122)$$

$f(t)$ at $t=0$ is taken to equation (2.121),

$$f(t=0) = C'$$

also

$$N_1(t=0) = C + C' = 0$$

$$N_1(t=0) = \frac{-\frac{N_0}{\tau_{nr}} \exp \left[-\frac{1}{\tau_{r_1}} \right]}{\frac{1}{\tau_{nr}} - \frac{1}{\tau_{r_2}}} + C' = 0 \quad (2.123)$$

$$C' = \frac{\frac{N_0}{\tau_{nr}} \exp\left[-\frac{t}{\tau_{r_1}}\right]}{\frac{1}{\tau_{nr}} - \frac{1}{\tau_{r_2}}} \quad (2.124)$$

also

$$N_1(t) = \frac{N_0}{\tau_{nr} \left[\frac{1}{\tau_{nr}} - \frac{1}{\tau_{r_2}} \right]} \left\{ -\exp\left[-\frac{t}{\tau_{r_1}} - \frac{t}{\tau_{nr}}\right] + \exp\left[-\frac{t}{\tau_{r_2}} - \frac{t}{\tau_{r_1}}\right] \right\} \quad (2.125)$$

Concentrations of carriers in intermediate state can be obtained as shown in equation (2.125). This concentrations of carriers is combination of rising and decay exponential decay.

II.5. Quantum Well Intermixing simulation

A diffusion phenomenon is important role to introduce simulated program. Other people have performed interdiffusion simulation model in III-V semiconductor compound. For example, K. M. Mukai, M. Sugawara and S. Yamazaki [29] have derived a formula that describe interdiffusion profiles of quantum wells and shown how the formula accurately model interdiffusion in quantum wells of lattice-matched $\text{In}_x\text{Ga}_{1-x}\text{As}_y\text{P}_{1-y}$ and $\text{Al}_x\text{Ga}_{1-x}\text{As}$ alloy semiconductors. Their formula explains how quantum energy shifts due to interdiffusion vary with annealing time and annealing temperature in various wide well layers of both $\text{In}_x\text{Ga}_{1-x}\text{As}_y\text{P}_{1-y}/\text{InP}$ and $\text{GaAs}/\text{Al}_x\text{Ga}_{1-x}\text{As}$ quantum wells. Or B. L. Weiss, Y. chan and co-workers [30] have presented a model for the optical properties of interdiffused InGaAs/InP quantum well structures investigated in a two-phase group V interdiffusion. This is characterized by three parameters: the interdiffusion coefficient in the barrier layer, the well layer, and the concentration ratio of diffused species at the well/barrier interface. Simulated model used in this thesis is produced by Dr. Goef Ares at National Research Council of Canada (NRC), Canada. Atoms in the barrier region will diffuse to QW region and some atoms may diffuse from the QW to

barrier region also. This can cause change of composition in QW and barrier region. Diffusion is a result to atomic hopping in combination with a concentration gradient. Simulation software written at NRC is assumed that exchange atom is happened on its species. For example, group-III atoms are exchange with group-III atoms. Group-V atoms will similarly interchange only with other group-V atoms. Detail of simulation is given in section 5.2 and 5.3. We firstly introduce Fick's law, which is the important role in diffusion process, in section 5.1. Fick's law describes that the flux of atoms will be towards the region with the lower concentration.

II.5.1 diffusion phenomena.

Atomic diffusion influences many non-equilibrium, particularly exposing to high temperatures. Diffusion of defects is efficient from a source deposited on the surface such as implantation process. Subsequently, the defects are activated by a thermal treatment. Diffusion process heals the implantation damage and places the implanted atom in substitutional sites. However, serious problem can arise because diffusion broadens the implanted profile. It follows that diffusion of the defects must be controlled in order to obtain the junction depth and profile. Generally Native point defects are involved in virtually every process during which an atom incorporated in the lattice of a semiconductor moves to another lattice site. Some example of diffusion paths in an elemental crystal is introduced such as diffusion interstitial, diffusing vacancy, concerted exchange of dopant, interstitial kick-out and etc. It is illustrated in Fig 2.16

barrier region also. This can cause change of composition in QW and barrier region. Diffusion is a result to atomic hopping in combination with a concentration gradient. Simulation software written at NRC is assumed that exchange atom is happened on its species. For example, group-III atoms are exchange with group-III atoms. Group-V atoms will similarly interchange only with other group-V atoms. Detail of simulation is given in section 5.2 and 5.3. We firstly introduce Fick's law, which is the important role in diffusion process, in section 5.1. Fick's law describes that the flux of atoms will be towards the region with the lower concentration.

II.5.1 diffusion phenomena.

Atomic diffusion influences many non-equilibrium, particularly exposing to high temperatures. Diffusion of defects is efficient from a source deposited on the surface such as implantation process. Subsequently, the defects are activated by a thermal treatment. Diffusion process heals the implantation damage and places the implanted atom in substitutional sites. However, serious problem can arise because diffusion broadens the implanted profile. It follows that diffusion of the defects must be controlled in order to obtain the junction depth and profile. Generally Native point defects are involved in virtually every process during which an atom incorporated in the lattice of a semiconductor moves to another lattice site. Some example of diffusion paths in an elemental crystal is introduced such as diffusion interstitial, diffusing vacancy, concerted exchange of dopant, interstitial kick-out and etc. It is illustrated in Fig 2.16

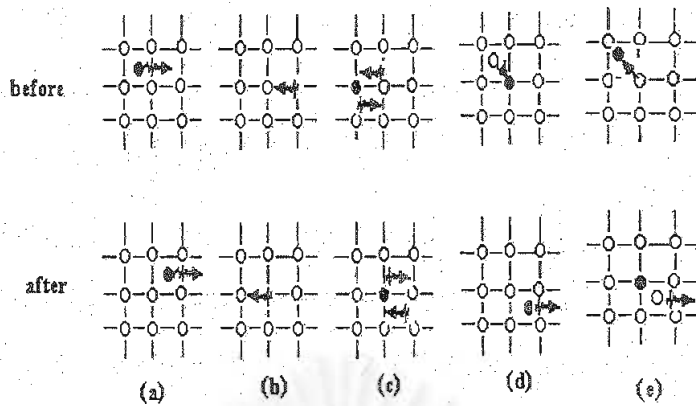


Fig 2.16 Diffusion path in an element crystal is introduced (a) diffusion interstitial, (b) diffusing vacancy, (c) concerted exchange of dopant, (d) interstitial kick-out and (e) interstitial kick-in. Opened circle is host atom and closed circle is defect.

This diffusion mediated by point defect is responsible for a number of important effects, for instance, these encountered during fabrication of microelectronic device.

Diffusion of atoms occupying lattice site in a semiconductor is governed by chemistry temperature, Fermi level (charge states), electric fields, pressure, strain fields, supersaturation of point defects (the ratio between their actual and equilibrium concentrations), and reaction rate between point defects (pairing, annihilation, clustering) as well as between point and extended defects (surface recombination, precipitation).

Let $C(\vec{r})$ stand for space distribution of concentration of identical particles, for example, interstitial, vacancies, or substitutional doping atoms dissolved in a bulk crystal. Assume that the particles can move in homogeneous crystal. The equilibrium distribution is thus $C(\vec{r}) = C^* = \text{const}(\vec{r})$. Inhomogeneities in $C(\vec{r})$ cause diffusion fluxes $J(\vec{r})$: the particles move against the concentration gradient $\text{grad } C$, so that the system eventually homogenizes.

Rejecting higher terms in the Taylor expansion of $J[C(\vec{r})]$, we get the Fick's law:

$$\vec{J}(\vec{r}) = -D\vec{\nabla}C(\vec{r}) \quad (2.126)$$

or if the concentration gradient is always directed along axis x (one dimensional case)

$$\vec{J}(\vec{r}) = -D \frac{\partial C(x)}{\partial x} \quad (2.127)$$

where D is diffusion coefficient which describes the ability of a particle to move: an average particle with diffusion coefficient (D) is displaced during time t by \sqrt{Dt} . Another example of diffusion coefficient are,

1. When the particle migrates with no energy barrier, as in gas,

$$D = \frac{1}{3} \langle v \rangle \langle \ell \rangle \quad (2.128)$$

where $\langle v \rangle$ is the thermal velocity and $\langle \ell \rangle$ is the mean free path of the particle

2. When there is an energy barrier for diffusion, as in a crystal, it is more appropriate to write D as

$$D = \lambda^2 \nu = \frac{a_0^2}{6} \nu_0 \exp\left[-\frac{G_m}{kT}\right] \quad (2.129)$$

where λ is a characteristic length (of the magnitude of the lattice spacing a_0) and ν is an effective jump rate. The relation between the jump distance λ and a_0 depends on the crystal lattice and on atomistic details of the diffusion process. The jump rate ν is proportional to a characteristic "attempt frequency" ν_0 is activated with the migration enthalpy $H_m = E_m + pV_m$, where E_m and V_m are the changes in the internal energy and crystal volume invoked by moving the particle from the stable site to the barrier site on the migration path. The Gibbs free energy of migration is $G_m = H_m - TS_m$; the migration entropy S_m accounts for equivalent jump paths and for entropy changes on the path.

The Fick's law in equation (2.126) leads in a natural way to the diffusion equation which describes the time evolution of C . Second Fick's law can be written since the change in number of the mobile particles in the volume dV , equal to $dCdV$, is brought by the local incoming and outgoing

particle fluxes \bar{J} during time dt , we can apply the law of mass action (continuity equation) to obtain:

$$\begin{aligned}\frac{\partial C}{\partial t} &= -\text{div}\bar{J} \\ &= \nabla(-D\nabla C) + g - a\end{aligned}\quad (2.130)$$

where g and a are rate with which the particles are locally generated and annihilated (for example, Frenkel pair generation and recombination). Equation (2.130) can be written in one-dimension:

$$\frac{\partial C}{\partial t} = \frac{\partial}{\partial x} \left(D \frac{\partial C}{\partial x} \right) + g - a \quad (2.131)$$

If the system is truly homogeneous, D is constant and,

$$\frac{\partial C}{\partial t} = D(\nabla^2 C) + g - a \quad (2.132)$$

(in one dimension)
$$\frac{\partial C}{\partial t} = D \frac{\partial^2 C}{\partial x^2} + g - a$$

when generation and recombination reaction are in equilibrium [$g = a = \text{const}$] or at least locally [$g(\bar{r}) = a(\bar{r})$], and then

$$\frac{\partial C}{\partial t} = D \frac{\partial^2 C}{\partial x^2} \quad (2.133)$$

This equation is Fick's second law. The relationship can also, of course, be expressed in terms of cylindrical or spherical co-ordinates. In order to solve Fick's second law in equation (2.133), boundary condition determined by the physical conditions is taken. So physical conditions of the experiment in realistic semiconductor such as III-V semiconductor using at NRC contribute to,

1. The thickness of material is much greater than $(Dt)^{1/2}$.
2. The diffusion coefficient is not a constant value, but as a function of concentration. For example D is only depended on concentration when the diffusion takes place at a single temperature, $D = D(c)$.

For the first physical condition, diffusion solution may be expressed in equation (2.134),

$$C = \frac{C_0}{2} \left[\operatorname{erf} \left(\frac{h+z}{2\sqrt{Dt}} \right) + \operatorname{erf} \left(\frac{h-z}{2\sqrt{Dt}} \right) \right] \quad (2.134)$$

where h is half the width of the layer and erf is the error function, an indefinite integral which comes about from the sum of several Gaussians (occurring by summing the thin film gaussians), as defined by:

$$\operatorname{erf}(\mu) = \frac{2}{\sqrt{\pi}} \int_0^{\mu} \exp(-\eta^2) d\eta \quad (2.135)$$

The second physical condition is counted to solve diffusion rate as non-fickian law. Information of $D(C)$ is required. It is hard to analyze directly non-fickian equation, especially in case of III-V semiconductors. Since the compositional profile in most quantum well interdiffusion studies is not directly accessible. It is standard to assume that the interdiffusion is Fickian, which contribute to first physical condition. Work done by Fujii and co-workers [31] [32] is one example of using Fick's second law and first physical condition. They obtained diffusion of InGaAs-InP semiconductors. Their assumption based on the diffusion of the phosphorus atoms in the barrier and wells by Fick's second law. The diffusion coefficients in the barrier and well assumed to be separate and different. The limitation of their assumption was the diffusion of phosphorus across the interface so flux of phosphorus atoms crossing the boundary between the barrier and the well is necessary to define. This was explained in terms of the addition potential energy, owing to the increase in strain, when an arsenic atom diffuses from the well into the barrier or a phosphorus atom from the barrier into the well [33] [34] [35].

II.5.2 Simulation for III-V semiconductors.

A program written by Dr. Goef Aers of NRC becomes a standard tool for our group while studying QWI. It allows us to determine the compositional profiles of the interdiffused QW based on the different interdiffusion models and to calculate the transition energies for the as-grown and interdiffused QW.

This program is a very important tool in QWI studies because it provides a link between physical changes to the QW and the resultant optical changes.

Square well, error function and statistical function models are used to simulate and to get physical meaning in the semiconductor material. All of these models are assumed that group 3 and 5 sublattices intermix separately. The square well model retains independent square well compositional profiles. This requires the intermixing on each sublattice to be strongly dependent on the composition on the sublattice with a much larger diffusion constant in the QW well than the barrier material. The error function model has independent error function compositional profiles. This model is a bit more complicated and more parameters are included to give more control. The defaults should work well in most cases. The error function "intermixing length" defines the intermixing. However, the statistical function model yields a composition profile that is flat with the original well, has a discontinuity at the original boundary and falls off according to a diffusion length in the barrier.

This program is friendly to the user. The user may fill these parameters. The parameters separate in 3 parts. The first part is defined for the as-grown system. In this part, the user needs to fill 4 parameters such as structure, substrate, QW and barrier composition, and QW and barrier width. Structure can be chosen as QW or superlattice. Substrate is either InP or GaAs. QW and barrier composition can be filled as either by percent of Ga and As or by strain (not in percent). The second part gives general parameters, which are independent of the intermixing model chosen. In this part, the user requires the number of intermixing steps, exciton binding energy, temperature and the number of intermixing steps. The number of intermixing steps is how many points for the calculation of photoluminescence (PL) shift as a function of intermixing. If it is set as zero, it will only correspond to a calculation for as-grown QW. Exciton binding energy is set a few meV at 4 K in order to precisely define this energy. Temperature can be chosen either at 4 K or at 300 K. Since the materials are warm at 300 K, exciton binding energy has been set to zero. The number of intermixing steps is a point for the calculation of Photoluminescence (PL) shift as a function of intermixing. The

default is zero corresponding to a calculation for the as-grown QW only. Third part fills the interdiffusion length step sizes for the group III and group V sublattices for chosen model.

After submission, the information is sent to a unix server and the calculations are performed. A new web page is then presented to you with a short summary of the results including as-grown structure information and heavy/light hole transitions followed by a short-form output for each intermixing step. Note that energy unit and well width unit are in meV and angstroms. Electron and hole confinement energies are with respect to the band edge at the center of the QW.

Simulation yields barrier gap, electron energy with respect to QW center, hh energy with respect to QW center hh_1 , hh energy with respect to QW center hh_2 , hh energy with respect to QW center hh_3 , starting hh transition energy, e-well QW center barrier height, hh-well QW center barrier height and starting hh QW center energy gap as shown in fig 2.17.

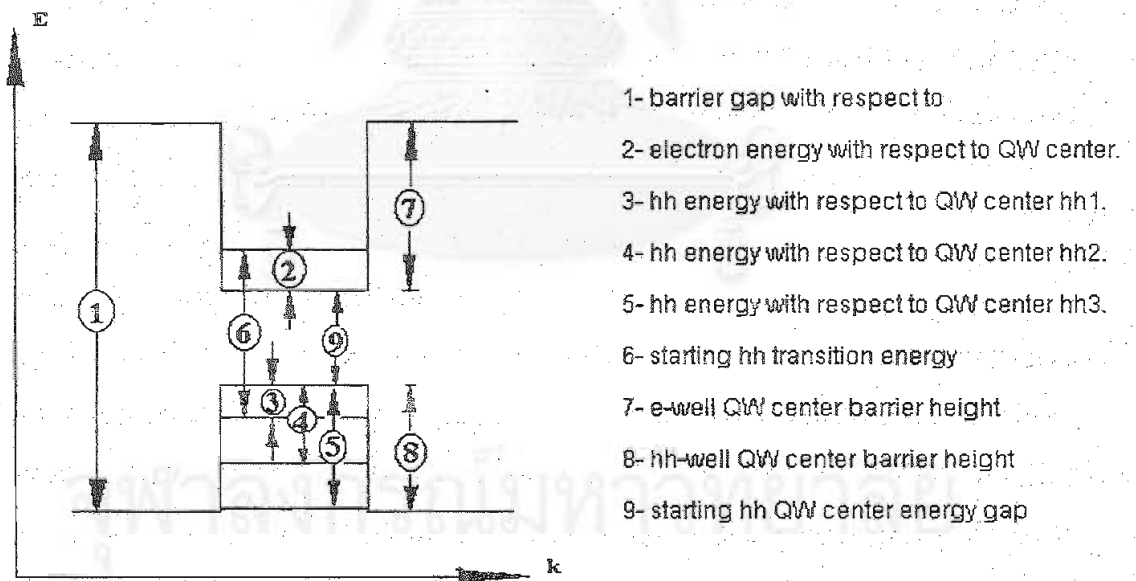


Fig 2.17 Band diagram of given parameter in program written by Dr. Goef Ares at National Research Council of Canada (NRC).

Simulation is strongly considered interdiffusion coefficient and strain effect in order to lead us reaching physically realistic semiconductor material.

1. Interdiffusion coefficient.

It is generally accepted that with regards to diffusion, each sublattice of III-V semiconductor structure operates independently. For example, InGaAs QW based on InP barrier interface, As and P, which in group V species, exchange together while Exchange of Ga and In will be similar in group III species. This mean if we know diffusion rate of specie of the same group specie, we will know the diffusion rate of other one. So it is useful to define the ratio of the interdiffusion length of each sublattice by

$$k = \frac{\Delta_{I(V)}}{\Delta_{I(III)}} \quad \text{for error function model} \quad (2.136)$$

$$k = \frac{\Delta_{L(V)}}{\Delta_{L(III)}} \quad \text{for square well model} \quad (2.137)$$

where Δ_{III} and Δ_V are the interdiffusion lengths of each sublattice.

Equation (2.136) and equation (2.137) give physical definition in group III-V semiconductors. For example, k value is limited to infinity. Group-V species move freely while group-III species is not moving. S.W. Ryu and co-worker [36] investigated interdiffusion behaviors with and without SiO₂:P capping in InGaAs based on InP superlattice. On the other end of the spectrum, k value is limited to zero. Group-V species is not moving while group-III species is moving freely. D.G. Deppe and N. Holonyak [37] have found that interdiffusion of only group-III atoms on Al_xGa_{1-x}As based on GaAs quantum well heterostructures was dominant. If k value is specific value (for example, $k = 10$), group-V atom species will move faster than group III atom species ten times. For example, Wai-chee Shiu and J. Michallef [38] have presented and discussed the result of error function distribution modeling the effects of different interdiffusion rates on the group-III and group-V sublattices on the confinement profile and the subband edge structure. The effects of strain and disordering compositional profile were considered to moving of those group-III and group-V atoms. Also H. Chen and co-worker [39] have

been reported that significant strain development observed across the InGaAs/InP QW structure is attributed to a group V to group-III interdiffusion length ratio of about 1.7.

2. Strain

In essence it is related to the growth of an epitaxial layer with a slight degree of lattice mismatch from and on a thick substrate. The lattice mismatch produces a strain on the grown overlayer and alters the physical properties. However, under controlled growth the crystallinity and long-range order are maintained over the whole structure including the epilayer. Since the crystal morphology is maintained throughout, the growth is known as pseudomorphic growth. If an epitaxial layer, whose lattice constant is close to but not equal to the lattice constant of the substrate, is grown carefully, then the growth may give rise to coherent strain as opposed to incoherent growth of polycrystalline or amorphous layers. There exists a critical thickness of the epilayer below which the film is thermodynamically stable and no misfit dislocation exists in the interface. Removal of the close lattice constant matching constraint greatly extends the number of superlattice material systems that can be considered. The first benefit is that materials with a wide range of bandgaps can be grown. In addition, the strain arising out of lattice constant mismatch may cause interesting changes in physical properties through deformation potential effects. Strain changes the bandgaps of the constituent materials and removes the degeneracy of heavy and light hole valence bands at $\vec{k} = 0$

Epitaxial layer is grown over a substrate as shown in figure 2.18. Along the boundary plane, a common 2D cell structure is maintained in such growth.



Fig 2.18 Growth of an epilayer on a perfectly lattice-matched substrate.

The case of growth of a film with lattice constant (a_F) on a substrate of lattice constant (a_S) is now of concern. The situation is shown schematically in Fig 2.19. The strain between two materials is defined as

$$\varepsilon = \frac{a_F - a_S}{a_S} \quad (2.138)$$

If one is to grow a monolayer of the film on the substrate and to keep the lattice constant unaltered then, as shown in Fig. 2.19(b), after every $\frac{1}{\varepsilon}$ bonds either a bond is missing or an extra bond appears as indicated. Although the picture is shown in one dimension, it should occur in a plane. We thus get a row of missing or extra bonds in the form of edge dislocations. The growth of

Tensile strain Compressive strain

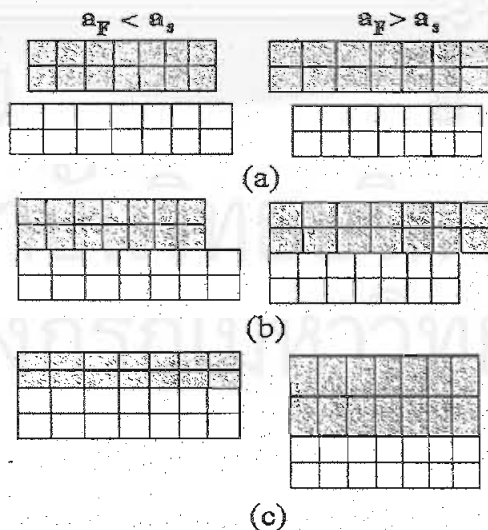


Fig 2.19 Schematic diagram depicting growth of a lattice-mismatched epilayer on a substrate. (a) Epilayer and substrate shown isolated; (b) extra bonds appearing or bonds missing to keep the lattice constant unaltered; (c) growth of strained layer with in-plane coherent strain.

an epilayer may occur in a different way as shown in Fig 2.23(c). Here all the atoms in the interface between the substrate and the epilayer are perfectly matched. This is accomplished if the overlayer is subject to compressive in-plane stresses along the x- and y-directions when $a_F > a_s$ and to tensile in-plane biaxial strains when $a_F < a_s$.

From the above description of strain, equation (2.138) is occurred in each layer of semiconductor material. However, in realistic QW semiconductor material is composed of several layer, mean strain is defined,

$$\bar{\varepsilon} = \sum_N \left[\frac{\varepsilon_1 w_1 + \varepsilon_2 w_2 + \varepsilon_3 w_3 + \dots}{w_1 + w_2 + w_3 + \dots} \right] \quad (2.139)$$

where $\varepsilon_1, \varepsilon_2, \varepsilon_3, \dots$ is strain in different layer and $w_1 + w_2 + w_3 + \dots$ is weight strain in different layer. N is a mount of layer. Mean strain is also probed by X-ray measurement. This way is probed all layers near the surface of the sample. So it is possible that X-ray measurement doesn't reach active QW layer if this layer is too deep. Strain used in the simulation software package at NRC takes into account the strain in each layer separately.

For $k > 1$, compressive spikes will develop at the QW/barrier interfaces, with tensile strain developing in the well center. The opposite strain profile occurs for $k < 1$. Even a QW intermixed using square well approximation will have strain development if $k \neq 1$. This is because the square of the group-III sublattice will have a different width than the square profile of the group-V sublattice, resulting in interface layers of a mixed composition.

For the InP system, there are no definitive studies illuminating diffusion mechanisms. Additionally, InP-based interdiffusion studies are in general more difficult to analyze. The reason can explain that there is the possibility of interdiffusion on both sublattices. For InP-based structures, most of the technologically interesting structures have differences in both the group-III and the group-V constituents at the QW/barrier interface, thus interdiffusion rates of both sublattices are required. And, there are only small range of InGaAsP compositions which are lattice matched to InP, thus, even if an structure starts

off lattice matched, the quaternary alloys that develop, depending on the k value might not be lattice matched.

II.5.3 Theoretical background for simulation.

The program generally assumes a single QW surrounded by infinitely wide barriers, and for all structures studied in this thesis, this is a reasonable assumption. If the barriers are narrow and/or significant amounts of diffusion occur, such that “communication” between neighboring QWs in a QW stack is expected, the equivalent calculations using a superlattice structure are also available in the program.

II.5.3.1 Compositional profiles

The compositional profiles for the group-III sublattice and group-V sublattice are calculated independently. For the square well model, the approach is rather different but also straightforward. Again, the equation is calculated independently for the group-III and group-V sublattices. For a given change in the group-III and group-V well widths, given by $\{\Delta_{L(III)}, \Delta_{L(V)}\}$ the concentration within the QW is simply determined by maintaining a constant amount of diffusant (i.e. the product of concentration times well width is kept constant), as given by:

$$C_{(III/V)} = C_{B(III/V)} + \frac{(C_{QW(III/V)} - C_{B(III/V)}) \cdot L_z}{L_z + \Delta_{L(III/V)}} \quad (2.140)$$

where $C_{III/V}$ now indicates the final Ga or As concentration in the well. $\Delta_{L(III/V)}$ indicates the change in width of the group-III or group-V square profile, and $C_{QW(III/V)}$ and $C_{B(III/V)}$ indicate the starting concentrations of Ga and As in the well and barrier, respectively.

For Fickian diffusion or the error function model, equation (2.134) is operated. The group-III solution is expressed in terms of concentration of Ga as a function of z position, and is calculated for each required $\Delta_{i(III)}$ step.

Similarly, the group-V solution is expressed in terms of concentration of As as a function of z position, and is calculated for each required $\Delta_{i(V)}$ step.

$$C_{(III/V)}(z) = C_{B(III/V)} + \frac{C_{QW(III/V)} - C_{B(III/V)}}{2} \left[\operatorname{erf} \left(\frac{\frac{L_z}{2} + z}{2\Delta_{i(III/V)}} \right) + \operatorname{erf} \left(\frac{\frac{L_z}{2} - z}{2\Delta_{i(III/V)}} \right) \right] \quad (2.141)$$

Here $C_{III/V}$ indicates the Ga or As concentration at a given position Z , and $\Delta_{i(III/V)}$ indicates the group-III or group V interdiffusion length, and $C_{QW(III/V)}$ and $C_{B(III/V)}$ are the as-grown concentrations of Ga or As in the well and barrier, respectively.

II.5.3.2 Quantum states for a lattice-matched square QW.

Now that we have composition as a function of z position, we will make use of band structure parameters of the various compositions in order to determine the resultant transition energies. In this subsection we will start with a review of the problem of a simple unstrained square QW, before adding the complexities of strain and arbitrarily shaped QWs. Figure 2.20 gives a schematic representation of the problem. An important simplification that is used throughout these calculations is that only the Γ point of the Brillouin zone is considered ($\vec{k} = 0$), where there is no mixing between the valence bands.

Ten band structure parameters of the materials must be known:

- bandgap of the unstrained bulk material for both the QW and barrier, $E_{g(QW)}$ and $E_{g(B)}$
- effective mass for each carrier in the QW and barrier, $m^*_{j(QW)}$ and $m^*_{j(B)}$, where j represent e (electron), hh (heavy hole) or lh (light hole)
- the absolute valence band energies of the QW and barrier materials, $E_{V(QW)}$ and $E_{V(B)}$ (in order to know the band offset between the two materials)

In the program, these ten parameters are determined for a quaternary $In_{1-x}Ga_xAs_yP_{1-y}$ of any $0 \leq x, y \leq 1$ by interpolation between empirical values for

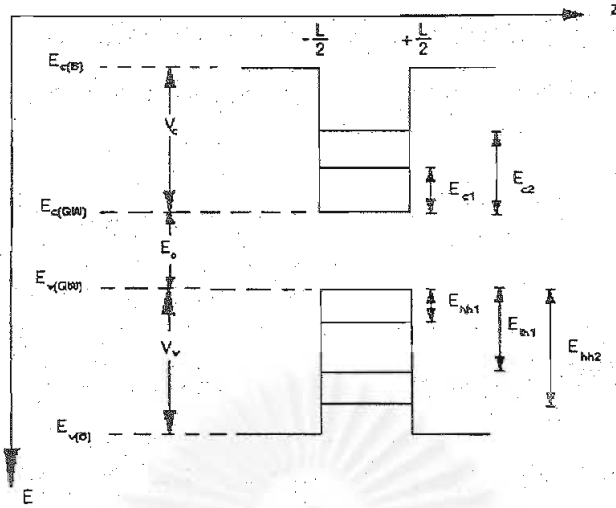


Fig 2.20 square quantum well energy levels

the four binaries InAs, InP, GaAs, and GaP. Details of the values and the interpolation scheme are described in the appendix A. The confinement potential in the z direction for the conduction, V_C , and valence bands, V_V , are determined from the differences in band energies of the well and barrier materials, as follows:

$$V_C = \begin{cases} E_{c(B)} - E_{c(QW)} = (E_{v(B)} + E_{g(B)}) - (E_{v(QW)} + E_{g(QW)}) & \text{for } |z| \geq L_z/2 \\ 0 & \text{for } |z| < L_z/2 \end{cases} \quad (2.142)$$

$$V_V = \begin{cases} E_{v(QW)} - E_{v(B)} & \text{for } |z| \geq L_z/2 \\ 0 & \text{for } |z| < L_z/2 \end{cases}$$

We now have the basic setup for particles confined to square potential wells in the z direction. In general, the wave function of the particle must satisfy the Schrödinger's equation:

$$\left(-\frac{\hbar^2}{2} \frac{\partial}{\partial z} \frac{1}{m_j^*(z)} \frac{\partial}{\partial z} + V_j(z) \right) \Phi_{j,n} = E_{j,n} \Phi_{j,n} \quad (2.143)$$

where j and n denote layer index and energy level index, respectively. For the simple square well $V_j(z)$ has two constant values (QW and barrier) for each carrier. Within the QW the solution for equation (2.143) is a sum of forward and backward travelling plane waves, while in the barriers, in the case of

$E_{j,n} < V_j$, the general solution is a sum of exponential (with appropriate coefficients set to zero in order to have physically correct solution on each side of the QW):

$$\begin{aligned}\Phi_{j,n(B)} &= \alpha_1 \cdot e^{+k_B z} + \alpha_2 \cdot e^{-k_B z} \\ \Phi_{j,n(QW)} &= \beta_1 \cdot e^{+ik_{QW} Z} + \beta_2 \cdot e^{-ik_{QW} Z}\end{aligned}\quad (2.144)$$

$$\text{where } k_B = \sqrt{\frac{2m_j^*(B)}{\hbar^2}(V_j - E_{j,n})} \quad \text{and} \quad k_{QW} = \sqrt{\frac{2m_j^*(QW)}{\hbar^2} E_{j,n}}$$

The quantization, or eigen energies ($E_{j,n}$) for this particle in a box problem will be obtained by applying appropriate boundary conditions to equation (2.144), that is, the continuity of wave functions and of the flux are continuous at the well/barrier interface. More details is in book written by Gerald Bastard [40]. This yields three transcendental equation (one for each carrier) of the form $f(E_{j,n}, m_j^*, L_z, V_j) = 0$ which can be solved graphically or numerically (analytic solution is only possible in the case of $V_j = \infty$). Note that $V_j = V_c$ for the electron problem, and $V_j = V_v$ for both heavy and light hole problems, but due to the two different masses of the holes, the final quantum energies of heavy and light holes states will be different (for a given n , the heavy hole quantization energies are smaller).

The effect of the quantum confinement is to increase the bandgap energy. In the X and Y directions the particles are free, and thus the total energy of each particle will be:

$$\begin{aligned}E &= E_{xy} + E_z \\ &= \frac{\hbar^2(k_x^2 + k_y^2)}{2m_j^*} + E_{j,n}\end{aligned}\quad (2.145)$$

where k_x and k_y are the wave vector in the x-y plane of the QW.

II.5.3.3 Effects of strain.

Lattice strain may be grown into a heterostructure, or may develop during interdiffusion. Strain occurs whenever the bulk lattice constant of the

InGaAsP alloy is different than that of InP. Since the quaternary layer is thin, it will conform to the InP substrate in the x and y directions, but undergo a tetragonal deformation in the z direction. These changes to the lattice structure result in changes to the energy of the electronic bonds and thus to the band energies of the thin layer in comparison to the bulk values for the same alloy. The changes are significant, and must be taken into account. An additional six material parameters are required for the calculation of the strained band energies, E_j' , from the unstrained band energy, E_j :

- a) the bulk lattice constant of the quaternary, a
- b) the elastic coefficients, C_{11} and C_{12} of the quaternary
- c) the hydrostatic and shear deformation potentials, A_C , A_V , and B of the quaternary

These six parameters are also calculated for a quaternary $\text{In}_{1-x}\text{Ga}_x\text{As}_y\text{P}_{1-y}$ of any $0 \leq x, y \leq 1$ using an interpolation scheme (included in the appendix A). The stress in the layer is biaxial in the xy plane, which can also be considered to be a hydrostatic stress minus a uniaxial stress in the z direction. A tensile (negative) hydrostatic stress affect all carrier bands, raising the conduction band and lowering both valence bands about the Γ point by an amounts P_C and P_V respectively. The uniaxial portion of the stress shifts the two valence (hole) bands in opposite directions and by different amounts, thereby lifting the degeneracy of the heavy hole and light hole in a bulk layer. This will result in different confinement potentials V_j for each of the three carriers in the z direction, again found using equation (2.143) but using the following equations for the strained bands E_j' instead of the unstrained bands E_j (these equations are only valid for the Γ point and for growth on [001] substrates) :

$$\begin{aligned}
 E_C' &= E_C - P_C \\
 E_{hh}' &= E_V + P_V - Q \\
 E_{lh}' &= E_V + P_V + \frac{1}{2} \left(Q - \Delta_o + \sqrt{\Delta_o^2 + 2\Delta_o Q + 9Q^2} \right)
 \end{aligned} \tag{2.146}$$

where Δ_o is the spin orbit splitting energy. The dependence of the E_{lh}' on Δ_o occurs because of the coupling between these two valence bands in biaxially

strained material. The hydrostatic deformation potentials, P_V and P_C , and the shear deformation potential, Q , are determined from:

$$\begin{aligned} P_C &= A_c(\varepsilon_{xx} + \varepsilon_{yy} + \varepsilon_{zz}) \\ P_V &= -A_v(\varepsilon_{xx} + \varepsilon_{yy} + \varepsilon_{zz}) \\ Q &= -\frac{B}{2}(\varepsilon_{xx} + \varepsilon_{yy} - 2\varepsilon_{zz}) \end{aligned} \quad (2.147)$$

where the strains in each of the three directions are defined by

$$\varepsilon_{xx} = \varepsilon_{yy} = \frac{a_0 - a}{a}, \quad \varepsilon_{zz} = -2 \frac{C_{12}}{C_{11}} \varepsilon_{xx} \quad (1.148)$$

where a_0 is the substrate lattice constant. These calculations treat the strain as a small perturbation, thus they are only valid for small strains (up to ~2%). A good reference for the effect of strain on semiconductor bands is by Chao and Chuang[41].

II.5.3.4 Quantum states for an arbitrarily shaped QW.

In an interdiffused QW, the composition and resultant E_g' vary continuously as a function of z -direction in the interdiffused QW for the error function model, and are multi-valued in the case of the square well model. In the program, the final quantization energies are determined using a transfer matrix approach (in fact, the earlier as-grown square well is also solved using the same algorithm, although it could be solved using the particle in a box solution). The potential profile is divided up into p thin regions where the V_j and m_j^* is assumed to be constant within each region. In the each p region the wave function solution to the Schrödinger equation can be written as a sum of two opposite travelling plane waves:

$$\begin{aligned} \Phi_{j,n}^P &= \beta_+^P \cdot e^{+ik^P z} + \beta_-^P \cdot e^{-ik^P z} \\ \text{where } k^P &= \sqrt{\frac{2m_j^* P}{\hbar^2} (E_{j,n} - V_j^P)} \end{aligned} \quad (2.149)$$

The use of complex arithmetic allows the general treatment of the case where $E_{j,n} > V_j^P$ (plane wave) and $E_{j,n} < V_j^P$ (decaying function). By applying the two

boundary conditions at the interface between each region, the coefficient β_+^p , β_-^p in each region can be related to those in an adjacent region by a 2x2 matrix. These matrices are multiplied together to relate the wave functions at each end of the system ($p=0$ and $p=P$) by:

$$\begin{bmatrix} \beta_+^0 & \beta_-^0 \end{bmatrix} = \begin{bmatrix} M_{11} & M_{12} \\ M_{21} & M_{22} \end{bmatrix} \begin{bmatrix} \beta_+^P \\ \beta_-^P \end{bmatrix} \quad (2.150)$$

where the matrix elements depend on the k^p 's (and thus on $E_{j,n}$). One of the two equations, one gets from multiplying out the matrices of eqn. 2.150 is

$$\beta_+^0 = M_{11}\beta_+^P + M_{12}\beta_-^P \quad (2.151)$$

Since the wave functions at each end (at $p=0$ and $p=P$) must decay for a physical solution, one can set $\beta_-^P = \beta_+^0 = 0$. Then, since β_+^0 must have a finite value, equation (2.151) will only be valid if $M_{11}=0$. The shooting method is applied to find valid choices of $E_{j,n}$ that will satisfy $M_{11}=0$. This is accomplished by using a linear grid of trial values for $E_{j,n}$, (chosen as many equally spaced values between the range of 0 and V_j). Each trial value of $E_{j,n}$ is used to calculate M_{11} . Wherever a change in the sign of M_{11} occurs following a stepwise increase in $E_{j,n}$, a valid choice of $E_{j,n}$ exists. Further trial values of $E_{j,n}$'s falling within that step are evaluated using a bisection method, repeated until a satisfactory accuracy is accomplished.

II.5.3.5 Optical transition energies.

The optical emission energies can now be determined by adding the appropriate quantization energies, $E_{j,n}$, to the calculated bandgap. For example, the energies of the first electron to heavy hole transition, and first electron to light hole transition are

$$e1 \rightarrow hh1 = E'_{g(QW)} + E_{e1} + E_{hh1} - E_x \quad (2.152)$$

$$e1 \rightarrow lh1 = E'_{g(QW)} + E_{e1} + E_{lh1} - E_x$$

where E_x is the binding energy of the exciton in the QW, typically a few meV and $E'_{g(QW)}$ is the bandgap at the center of the interdiffused QW. E_x has been fixed to $E_x=7$ meV for 4K calculations and $E_x=0$ for 300K calculations in this

thesis. Variations of E_x due to its dependence on well width and composition are expected to be small (the order of a few meV) for the magnitude of changes to width or compositions occurring during intermixing.

II.5.3.6 Use of the results for QWI studies.

The entire calculation of the eigen energies is repeated several times for a range of interdiffusion steps. One can then derive information such blueshift, ΔE , of the lowest transition (e.g. $e1 \rightarrow hh1$) as a function of interdiffusion length for a given interdiffusion model and k value. By repeating the process calculations for several different k values one can look for the best match to experimental values. However, interdiffusion length is not usually experimentally accessible parameter, thus additional experimental information must instead be used sought if a model is to be determined. Knowledge of a second optical parameter (e.g. shift of the $e1 \rightarrow lh1$) or direct information as to the composition are necessary in order to reduce the number of unknowns. These approaches are used in the thesis to determine valid models. Alternatively, if a model and k value are assumed, one can extract a Δ_i or Δ_L value from a measured ΔE . Another approach that can be useful is to compare the shifts in different structures which have nominally been intermixed the same amount (thus assuming the same Δ_i/Δ_L for all the QWs). This would be useful for studying the effects of composition or strain on the intermixing process, but the challenge is being confident that the interdiffusion lengths are the same in all the QWs.

II.5.3.7 Accuracy of the modeling.

The calculations of the compositional profiles for both error function is exact, and thus is as accurate as their underlying assumptions. As was discussed previously, the assumption of Fickian behaviour is unproven and is somewhat doubtful, and this is why two different interdiffusion models are

considered here. Calculations of the material parameters E_g , Δ_0 , m^*_j , a , C_{11} , C_{12} , A_v , A_c , B , all rely on empirical polynomial fits, as described in the appendix B. The expected errors on E_g is only a few meV, or $\pm 0.2\%$, and on lattice constant a it is $\pm 0.0005 \text{ \AA}$ or 0.01% , while the error on the other parameters (which are more difficult to measure) could be as high as $\pm 10\%$. The absolute valence band energy (relative to an average crystal potential) and thus the band offsets between different materials is a more difficult parameter to measure experimentally and thus there is an expected error might be more in the range of $\pm 20\%$. However, the calculated quantization energies are not very sensitive to differences in the offsets, especially in the case when the value for the offset in the bands is ~ 0.4 to $0.6 \times \Delta E_g$, as is the case for the materials under study here. As a whole, we expect that these calculations provide transition energies, which are accurate to within about 5 meV, for a given interdiffusion assumption. Experimentally, we observe variations across samples of up to 5 meV. Thus, the accuracy of the calculations are sufficient for our studies, as long as we consider blueshift of the order of 10 meV or greater.

A major simplification of these calculations is that we assume the bandstructure is direct, and only the zone-center ($k_{xy}=0$) transitions are calculated. As tensile strain develops, off-zone-center maxima in the "light hole" band can become the highest energy point. Light hole is put in quotations here because it would actually be a mixed-hole band when not at the zone-center. The actual transition energy in such material could have an indirect character and a lower transition energy than that calculated by the program. However, the discrepancy in terms of energies will likely be small, since this off-zone-center maxima is calculated to be only ~ 10 meV different than the zone-center maxima for the materials studied here. But optical properties, which depend on carrier overlap, such as carrier lifetimes, could be dramatically altered. This additional complication must be realized when significant tensile strains (of the order 1-2%) in the QW center occur, in particular when examining large blueshift and $k \gg 1$. This scenario may occur

in a few of the samples in this thesis (InGaAs/InP structures where ΔE is the order of 150 meV or larger).

II.5.3.8 Comments on as-grown QWs.

Epitaxial growth is fairly well controlled process, giving accuracy in the QW width of ± 0.5 nm, and compositions within $\pm 1\%$. Predicted transition energies from the nominal structure can be compared with PL measurements. Discrepancies between the calculation and experiment are used to refine the values for the QW width and composition. Additional characterization is also beneficial to further confirm the exact structure. High-resolution transmission electron microscopy (TEM) can determine QW thickness to ± 0.5 nm, while high resolution X-ray diffraction (XRD) can also be helpful to assess structure periodicity and mean strains. Results are also fed back to the growers in order to maintain predictable growths. As-grown QWs are not perfectly square, as there are usually one to three monolayers (0.29-0.87 nm) of mixed alloy material at the interfaces between the QW and barrier. Their presence will account for minor discrepancies between the results of TEM, PL and X-ray diffraction and calculations based on a perfect square well. In fact, X-ray is an excellent technique for determining the exact nature of the interfaces [42]. But most importantly for this thesis, their presence can be mostly ignored when considering interdiffusion. This is because they are 10 to 20 times narrower than the QW, and thus even when short interdiffusion lengths are considered, they have negligible effects, as confirmed by more detailed calculations. However, these interface layers may have a great impact on the time-resolved photoluminescence properties if some type-II alignment or indirect gap nature develops as a result of the presence of these layers.

CHAPTER III

EXPERIMENTAL TECHNIQUES

III.1 Characterization techniques.

Optical spectroscopy of semiconductors is a useful tool to study the properties of III-V semiconductors. It has helped to shape the concepts of energy gaps, impurity states and resonant states among others. In both intrinsic luminescence and near-gap absorption, the main features of the spectrum can be associated with the magnitude of the energy gap. So in this chapter the details of the following techniques will be revealed: photoluminescence (PL), time-resolved photoluminescence (TRPL) and absorption measurement. General ideas of those set-up measurements can be found in the book written by D.K. Scrode [43] and G.W. Ewing [44]. Those techniques have been setup at national research council of Canada (NRC). Rapid thermal annealing (RTA) process is a powerful technique to enhance the bandgap shifts in InGaAs/InP heterostructure with created excess defects. Thus RTA will also be described. Furthermore, a description of the simulation software called transport of ion in Matter (TRIM) used for investigating suitable implantation energy will also be included in this chapter.

III.1.1 Photoluminescence (PL).

Generally PL is the optical radiation emitted by a material resulting from its non-equilibrium state caused by an external light excitation. PL provides a non-destructive technique for determination of certain impurities in semiconductors and for detection of shallow-level impurities. But it can also be applied to certain deep-level impurities. However, in this thesis PL is

mainly employed to measure the change of energy gap in InGaAs/InP heterostructure after intermixing.

A typical PL measurement system consists of an excitation source, a variable-temperature cryostat with a sample holder assembly, a high-resolution scanning spectrometer, and a detection system. Low-temperature measurements are necessary to obtain the fullest spectroscopic information by minimizing thermally-activated non-radiative recombination processes and thermal line broadening. The thermal distribution of carriers excited into a band contributes a width of approximately $\frac{kT}{2}$ (~ 1.8 meV at $T = 4.2$ K) to an emission line originating from that band. This makes it necessary to cool the sample to reduce the width. The sample is excited with an optical source, typically a laser with $\hbar\nu > E_g$, generating electron-hole pairs (ehp's) that recombine by one of several mechanisms. For a radiative recombination process, a photon with $\hbar\nu \approx E_g$ will be emitted. The emitted light from the sample is analyzed by a spectrometer and detected by a photo-detector. Spectra may be recorded directly as either a single point PL or a mapping PL (X-Y recorder). We will illustrate a single point PL as well as a mapping PL setup at IMS, NRC in Canada in the following section.

III.1.1.1 Single point PL system.

According to fig 3.1(a), sample is mounted on a copper block using two strips of teflon tape in a manner which does not strain the samples. Then this copper block is put in the sample chamber of a liquid Helium cryostat. During the experiment, liquid helium is slowly injected in the sample space below the sample and evaporates near the sample in such a way that the sample is normally in contact with He heat exchange gas at 4.2 K. The temperature of the sample can be varied using a heater mounted on the copper block holding the sample and the temperature can be monitored via a sensor also placed on the copper block. Thus the sample temperature can be varied from 4.2 K to

300 K. The excitation source consists of a steady-state laser which is focused onto the surface of the sample using a focusing lens as shown in the black bold line of fig 3.1(a). The laser excitation sources available for this system are,

- Ar⁺ gas laser - mainly using wavelength at 514 nm - is able to provide high powers, which can be up to 12 W. The laser beam is typically focused to a 50 micron diameter spot on the sample surface. Ar⁺ laser provides light in blue-green range. At those wavelengths, light is absorbed in our InP-based sample within the first few 100 nanometers from the surface.
- He-Ne gas laser which emits at 632.8-nm with 3 mW of power.

Neutral density filter may be used to diminish the intensity of excited source if the power of excited source is too strong. Generally the focusing Lens used had a small numerical aperture which provided a spot size of 50-100 microns on the sample surface. Electron-hole pairs are generated in the sample after the excitation source hits the sample as illustrated in fig 3.1(b). Electrons and holes recombine radiatively and photons are emitted in a half sphere as shown in Fig 3.1(a). A collection Lens is used to collimate the light emitted from the sample and this beam is steered in free space towards a spectrometer. Photon signal was detected and analysed by a Bomem MB-160 FTIR spectrometer [45] [46] [47]. Subsequently this signal was sent to computer in order to plot intensity as a function of either energy or wavelength. A long-wave pass filter is used in front of spectrometer in order to block any laser light from entering the port. Neutral density filters may be used again in this path to reduce the signal intensity at the spectrometer port.

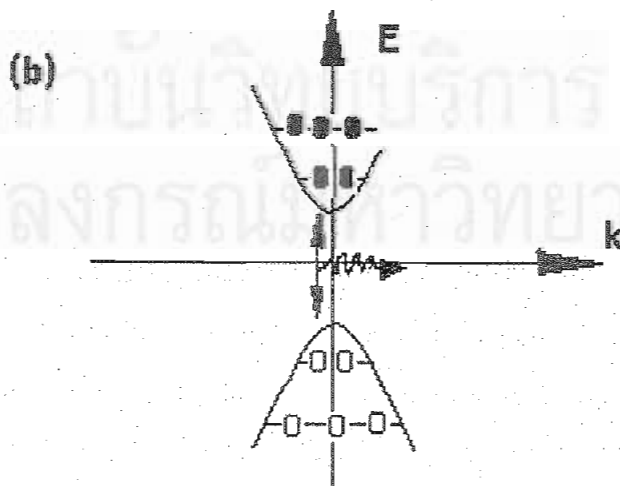
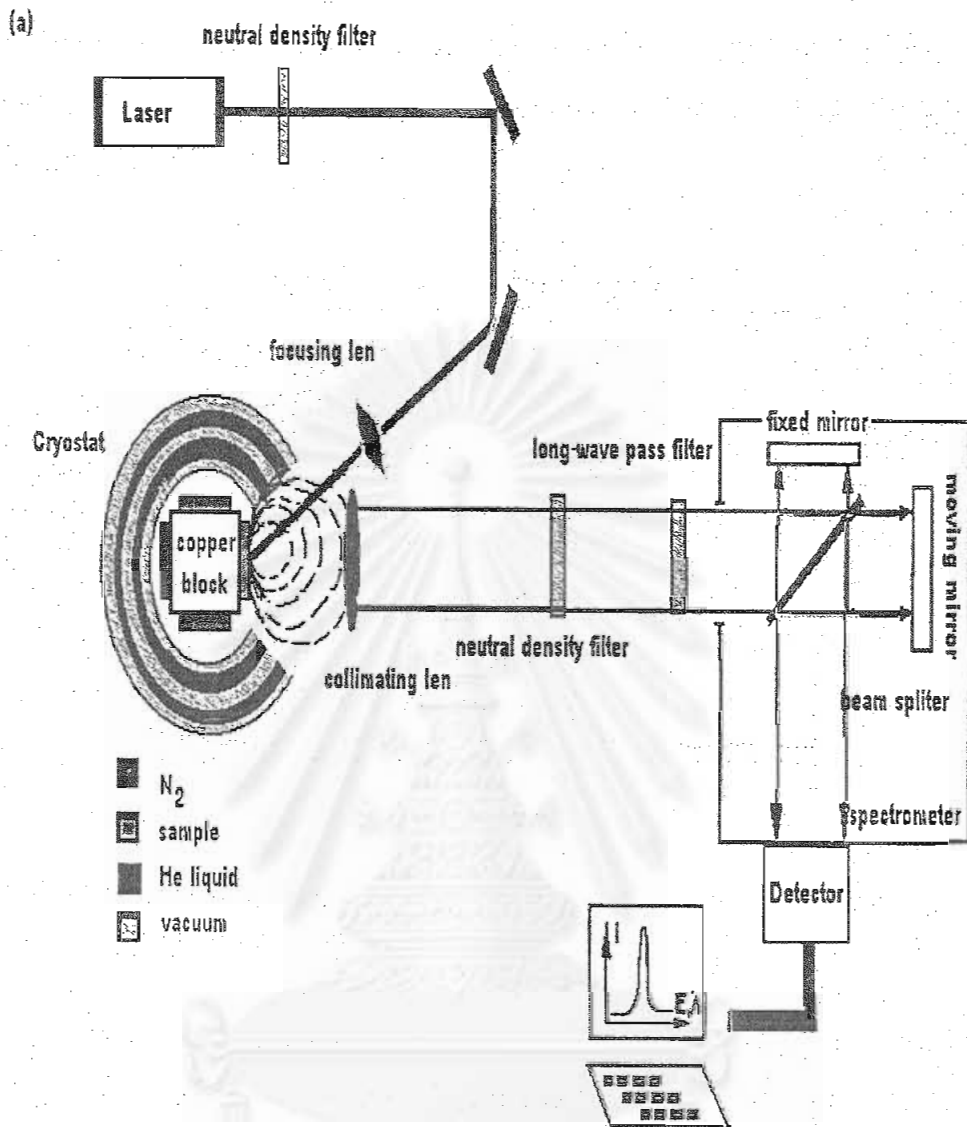


Fig 3.1 Schematic of (a) single point PL system at IMS, NRC in Canada and (b) recombination processes in semiconductors.

In figure 3.2, PL spectra shift to lower energy while temperature is rising. The explanation is that temperature shifts the energy state in QW region. Moreover, the PL spectra is broaden at higher temperature because exciton's kinetic energy.

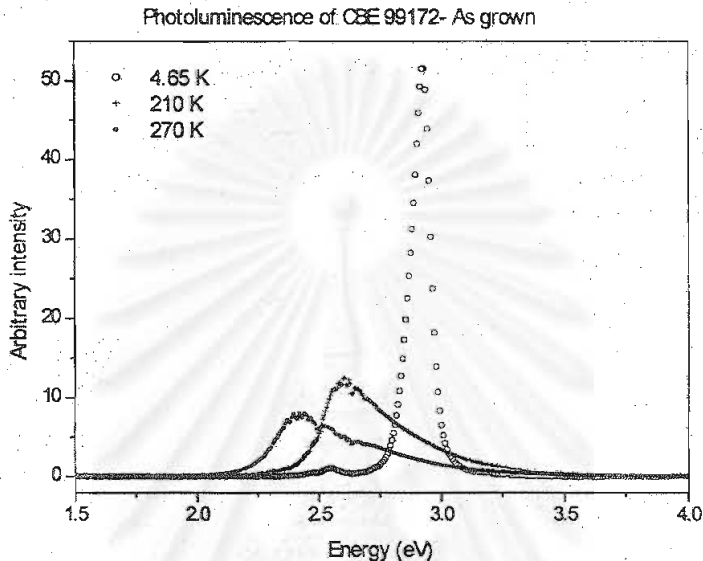


Fig 3.2 Photoluminescence of an non-intermixed InGaAs/InP QW sample at varying temperature.

PL mapping is similar experiment set-up to single PL system but PL mapping can monitor uniformity of semiconductor. PL mapping will show in the following section.

III.1.1.2 Mapping PL system.

To investigate the uniformity of the samples and get better averaging of the effect of the intermixing process across the sample surface, an automated PL mapping system was built where the sample is placed on x-y stage. It is logistically difficult to use a cryostat in this set-up, so samples were uncooled (temperature about 300 K). The sample sits face-up on a x-y stage controlled by custom written software as shown in figure 3.3. The optical excitation source used typically consists of 980 nm semiconductor laser diode operating

from 0-50 mW. In this thesis, 980-nm laser diode with 20 mW was normally applied as excitation laser source in the mapping PL system. The light from

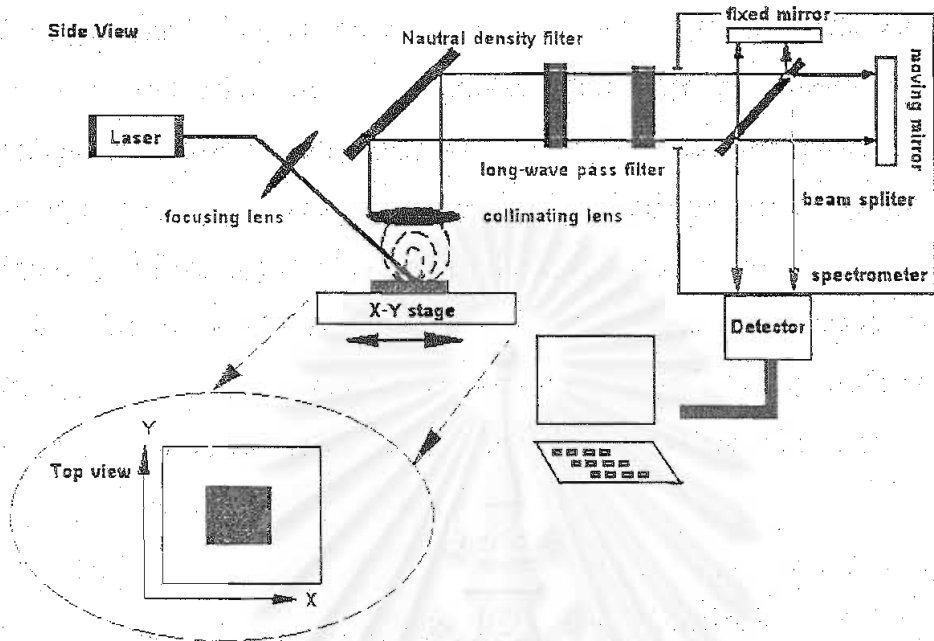


Fig 3.3 Schematic of mapping PL system at NRC.

the laser diode is collimated and directed to the sample through a focusing lens. The spot size is less than 250 microns. Similar to single PL system, photons are emitted from the sample, and collected through collimating lens. The collected PL is directed to the entrance port of a Bomen MB-160 FTIR spectrometer [50][51][52] equipped with a TE cooled InGaAs detector sensitive in the spectral range of 800-1650 nm. The spectral resolution was usually set at 32 cm^{-1} (4 meV), but it could be as low as 2 cm^{-1} (0.25 meV). After the first PL spectrum is recorded, a step in x or y is performed by the translation stages and a new PL spectrum is recorded at that point. Typically the step sizes in x and y direction is set at 500 microns. After repeating this process over a predetermined area, a complete PL spectrum similar to that presented in figure 3.2 is obtained for each measurement point on the surface. Data processing is then performed so that the computer will display either PL peak intensity or PL peak energy as a function of x-y position. Fig 3.4 shows

an example of a PL mapping experiment performed on 6 pieces of 5x5 mm InGaAs multiple QW samples. In fig 3.4 (a) PL peak energy (wavelength) is displayed as a function of x-y position. According to the color code displayed on the right hand side, in the center of most of the samples the main peak is centered around 1410 nm, which shows that very good uniformity of the optical properties is obtained across these 6 samples. A second PL peak is detected at the edge of the samples centered around 1563 nm. Fig 3.4(b) shows the intensity of the detected peak as a function of position. It can be seen that there is a bit of variability between the different samples with some regions emitting almost twice as much as some others. Typically, a small sample can be mapped in about one hour, while 2 inches wafer takes overnight.

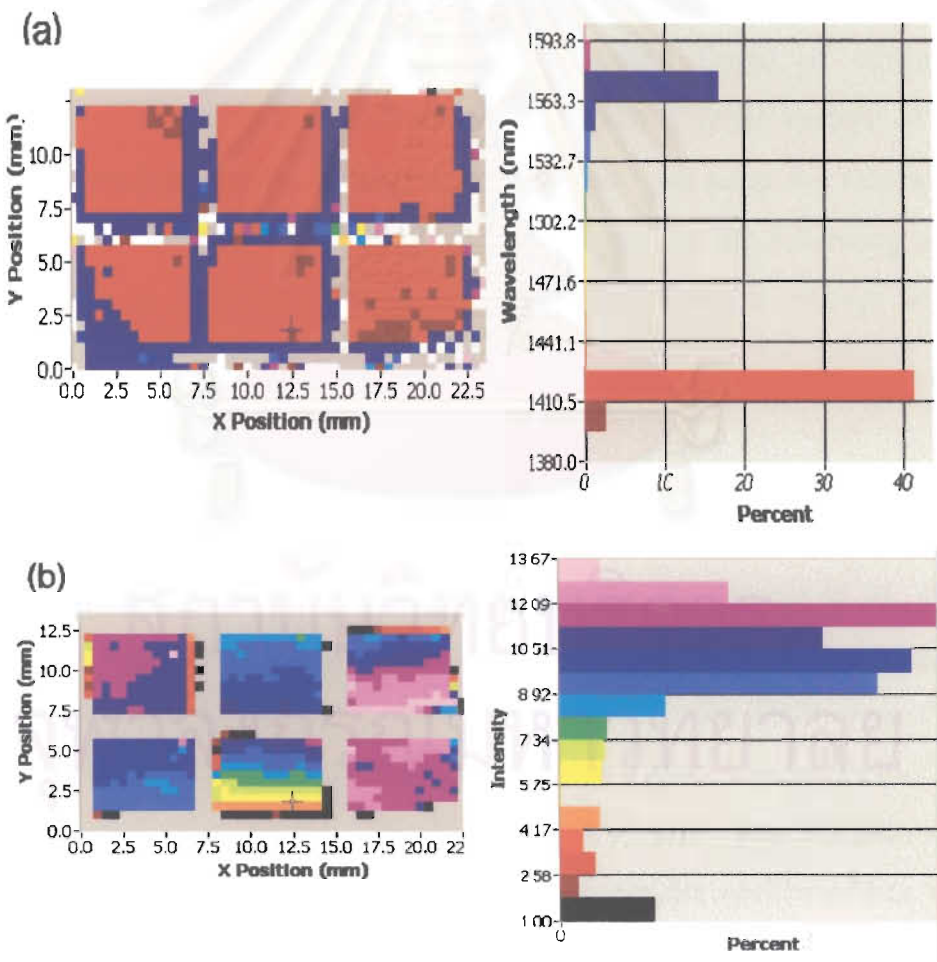


Fig 3.4 spectral data is displayed (a) intensity as a function of x-y position and (b) emitted photon energy (wavelength) as a function of x-y position.

III.1.2 Time-resolved Photoluminescence (TRPL).

The PL techniques discussed so far are time-averaged techniques in which the sample excitation is continuous and the signal detection apparatus averages the signal over periods of time much longer than the natural time scales of the system being probed. By using short laser pulses instead of continuous excitation coupled with time-sensitive light detection equipment one can obtain information about the temporal evolution of the light emission in the sample. This evolution is in turn related to the carrier dynamics in the sample probed. For example, these time-resolved measurements can be of use to probe the energy relaxation of quasi-particles such as excitons in QWs [53] [54][55][56] to probe hot phonon distributions and the lifetime of electron-hole liquids and plasmas[57], and to measure trapping times of carriers by impurities or other crystalline defects. There exist a great variety of time-resolved PL measurements, and the technique that was used for this work is referred to as time-correlated single photon counting. In the following section this technique is described along with the experimental set-up used to implement it and perform the measurements.

System set-up and functioning

Figure 3.5 shows a diagram representing the time-resolved PL system that was used to perform the time-resolved experiments in the range of 1.3-1.7 microns. In contrast to the steady-state PL experiments, for TRPL experiments the laser source must be pulsed. The pulsed laser system used with the TRPL system consisted of a 12 W CW AR+ ion laser pumping a mode-locked Titanium doped Sapphire (Ti:Saph) laser providing pulse widths of less than 2 ps at a repetition rate of 82 MHz. This repetition rate must be reduced to 4 MHz or less by a pulse picking system (Pockel cell and synchronous countdown) because repetition rate at 82 MHz is too fast for the finite reset time of the electronic components in the system (TAC, CFD etc.) During the

experiment, an autocorrelator is used as shown in fig 3.5 (a) in order to monitor the shape and width of the laser pulses. Proper traces on the autocorrelator indicate that the mode-locked laser system operates properly.

To perform the actual experiment, the laser pulse train obtained from the laser system is sent onto the sample which is placed in a liquid Helium cryostat and immersed in a He heat exchange gas maintained at 4.2 K or higher temperature as shown in figure 3.5. Typically about 1 mW of averaged laser powers is used. When a pulse impinges on the surface of the sample, a carrier population (excitons) is instantaneously created in the QW, which provides the initial population as described in chapter II section II.4.2. This population will decay with a lifetime dictated by the conditions present in the sample during the experiment. As the population decays, so is the signal emitted from the sample and as one thus obtains a light pulse from the sample with a lifetime dictated by the carrier lifetime inside the sample. The goal of this experiment is to obtain the temporal shape of the light pulse emitted from the sample.

To achieve this result, the TRPL measurement [58] is based on a time to amplitude converter (TAC) which provides the time correlation between the PL emission and the excitation laser pulse. The laser pulses are focused on the sample surface using a focusing lens as in the steady-state PL system. The sample signal is collected by a collimating lens and steered towards a detection system consisting of a Chezny-Turner double grating spectrometer with an InGaAs photomultiplier tube (PMT) placed at the exit slits of the spectrometer. The Hamamatsu InGaAs PMT can detect photons in the range 400 nm – 1700 nm. Because of the low bandgap of the InGaAs, the photocathode was cooled down to ~80 C using liquid nitrogen in order to minimize thermal noise. The detection system typically consists of a monochromator (spectrometer) and a single or multi-channel detector. Photomultiplier tubes, pn-junction diodes, and charge-coupled devices (CCDs) are popular detector types for luminescence spectroscopy. Before reaching the detection system, the PL can be attenuated with neutral density filters, and the laser light scattered from the surface of the sample is blocked using a long-wave pass filter. A focusing lens

with numerical aperture matched to that of the spectrometer focuses the infrared emission from the sample onto the entrance slits of the spectrometer. The spectral resolution of the detection system depends on the slit width selected and can be at least as good as 1.0 nm. Usually, the detection wavelength is selected to coincide with the PL peak emission of the QW sample being measured. For each photon detected on the surface of its photocathode, the InGaAs PMT generates an electrical pulse with a rise time of 3 ns. This pulse is amplified and sent to a constant fraction discriminator (CFD) to select a reference point on the electrical pulse to increase the time resolution of the system beyond the 3 ns rise time of the generated pulse. The output of the CFD consists in a square electrical pulse of set duration (a few microseconds) with a very sharp leading edge. This leading edge is used as an input to a time-to-amplitude converter (TAC). When the TAC becomes available, electrical

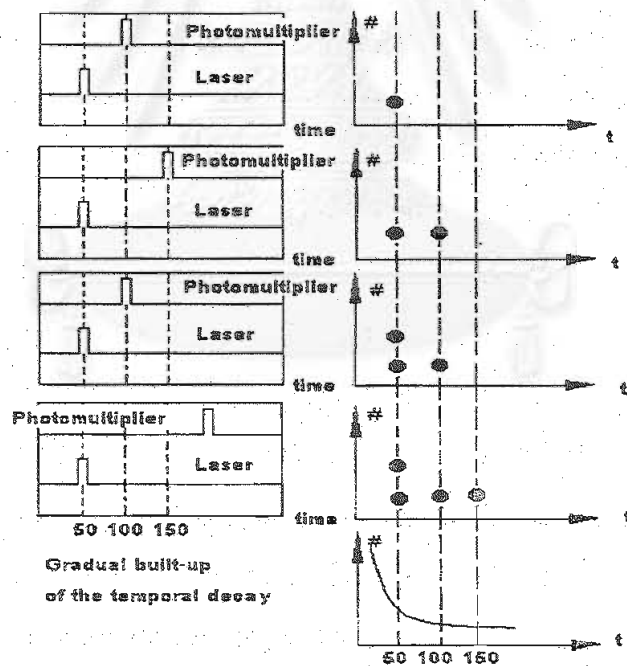


Fig 3.6 Principle of operation of a single-photon correlation. The temporal decay is gradually built up by making successive conversions of the time elapsed between the incident laser pulse and the detected luminescence photon.

pulse coming from the InGaAs PMT is interpreted as a START signal, and a capacitor is charged linearly as a function of time from a constant current source until a STOP pulse is detected. The stop pulse is derived from a fraction of the incoming laser pulse which is sent to a photodiode (see figure 3.5a) to derive an electrical pulse from the laser pulse. This pulse is amplified and sent through an adjustable delay line to account for the optical path and detector reaction time in the other arm of the detection system. This pulse is fed to a CFD and then to the TAC as a stop pulse, and the time difference between the START and STOP pulses determines the accumulated charge on the capacitor, and the TAC generates an analog voltage in the range of 0 – 10 V proportional to the charge stored in the capacitor. The ramping time to charge the capacitor from 0 – 10 V can be selected to be as low as 20 ns and as large as several milliseconds. The output voltage generated by the TAC is digitized and stored in a multi-channel analyzer (MCA) where the channel number corresponds to the amplitude of the TAC voltage output, hence to the elapsed time. Before the next event can be recorded, there is a time delay for discharging the capacitor and resetting the TAC. During this time period the TAC can not accept any START signals. The next PL photon starts the TAC and laser pulse stops it, resulting in an additional count in a channel of the MCA. This successive sequence of events being recorded is illustrated in figure 3.6. By repeating this process, the decay spectrum will slowly built up.

The system response for the TRPL set-up can be obtained by using an ultra-sort (δ -function like) light pulse into the start arm of the experimental set-up. This pulse must be correlated with the laser pulse and the easiest way to derive a light pulse with these properties is to make use of the laser light scattered from the surface of the sample. By removing the long-wave pass filter and setting the detection wavelength of the spectrometer to be equal to the laser wavelength, one creates the above conditions. After installation of the InGaAs PMT, this test was performed to characterize the temporal response of the system. These results will be presented in chapter IV.

III.1.3 Absorption measurements.

In order to gain information on the energy position of both the heavy- and light-hole $n=1$ transitions, absorption techniques are employed. The splitting between heavy- and light-hole transition together with simulation program, which details in section II.5 of chapter II, can be specifically used to determine a k -value. Generally light traversing a semiconductor decreases in intensity along the propagation direction due to absorption processes. Let us consider a simple example that a light beam propagating along the z -direction which enters an absorbing semiconductor at $z=0$. The light intensity can then be written as

$$I = I_0 \exp[-\alpha z]$$

where α is the absorption coefficient and I_0 is the light intensity at $z=0$. Different physical processes give rise to different absorption coefficients for the absorption of photon in semiconductors. As a result of this, our experimental set-up at national research council of Canada (NRC) requested two times measurement in order to produce the absorption spectra. Figure 3.7 shows schematics of the transmission set-up used to perform the experiments. A broad band white light source of the Bomem's FTIR spectrometer produced light in the range from 500 nm (2.4797 eV) to 1.7 microns (0.729 eV). This white light is collimated, attenuated by passing through a 200-micron pinhole, and passed into a Michelson Interferometer. The recombined light beam at the output of the interferometer is shone through the sample mounted in a continuous flow variable temperature cryostat. Samples were cleaved in a square 5x5 mm and wrapped in Teflon tape to hold the pieces on a copper block with holes so that the broad band white light can pass through and reach the detector. Then this copper block will place in cold finger cryostat so that the samples can be kept at temperatures of 5 – 6 K during the experiment, as measured from a temperature sensor placed on the copper block. Small amounts

of thermal compound were used to improve the thermal conductivity between the sample and the copper. After going through the sample, the light is sent onto a TE cooled InGaAs detector and the light intensity detected is recorded as a function of position of the moving mirror (see fig 3.7). This produces an interferogram on which a fast Fourier transform is performed to obtain the spectrum as a function of wavelength (or energy). Since the QW is very thin

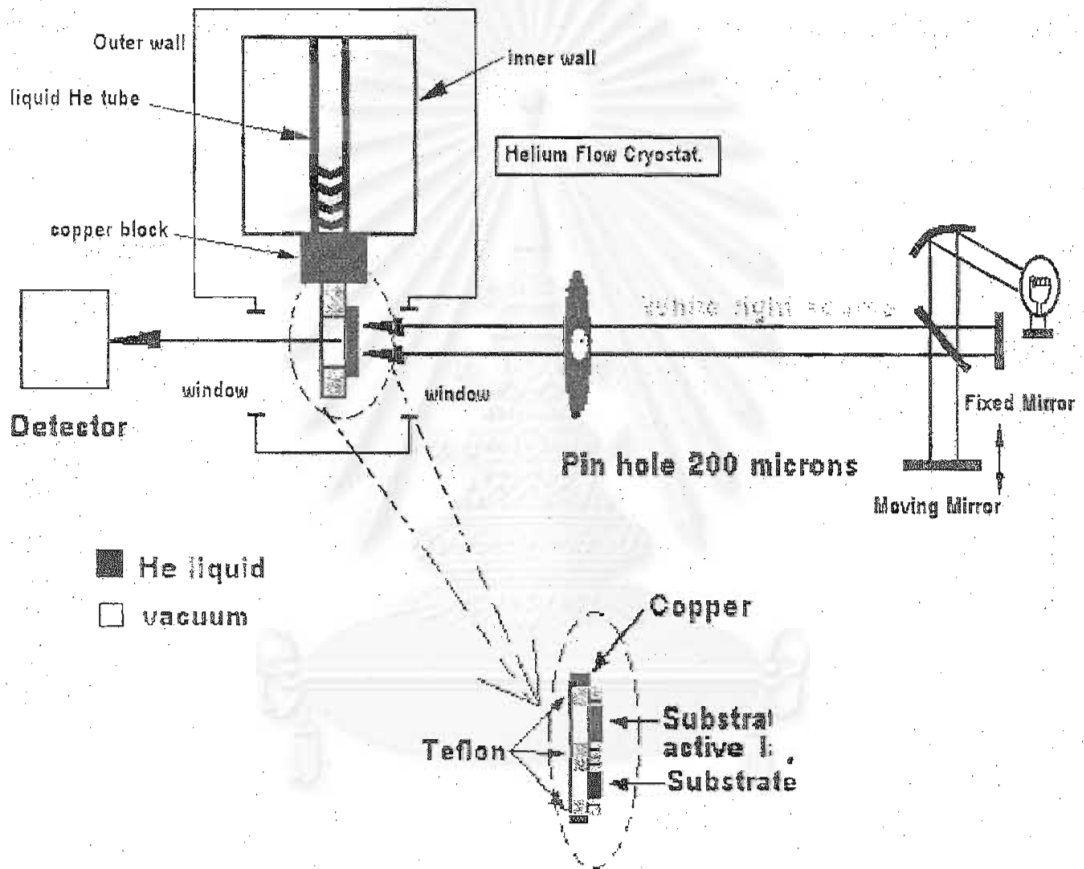


Fig 3.7 Setup absorption measurement technique at national research council of Canada (NRC).

compared to the substrate (QW to substrate thickness ratio is in the order of 10^{-4}), the absorption of the substrate in the sample completely dominates the resulting spectrum. Figure 3.8 a) compares the result obtained for an InGaAs QW sample grown on an InP substrate, with the result obtained for a virgin InP substrate. The effect of the presence of the QW cannot be resolved just by comparing these two spectra. However, when dividing the signal obtained from the QW sample by that of the substrate-only sample, one effectively removes

the absorption background due to the substrate and absorption features from the QW can be resolved as shown in fig. 3.8 b). Below 950 meV, there is very little light absorbed in the QW since the photon energy is below the energygap of the QW layers. At slightly higher energies, the absorption increases until it reaches a peak when the photon energy is resonant with the first heavy-hole QW transition at around 970 meV. The absorption decreases if the photon energy is increased passed the hh resonance, and a second peak is observed at the light-hole resonance around 1020 meV. The next resonance around 1150 meV may originate from higher confined states of the QW.

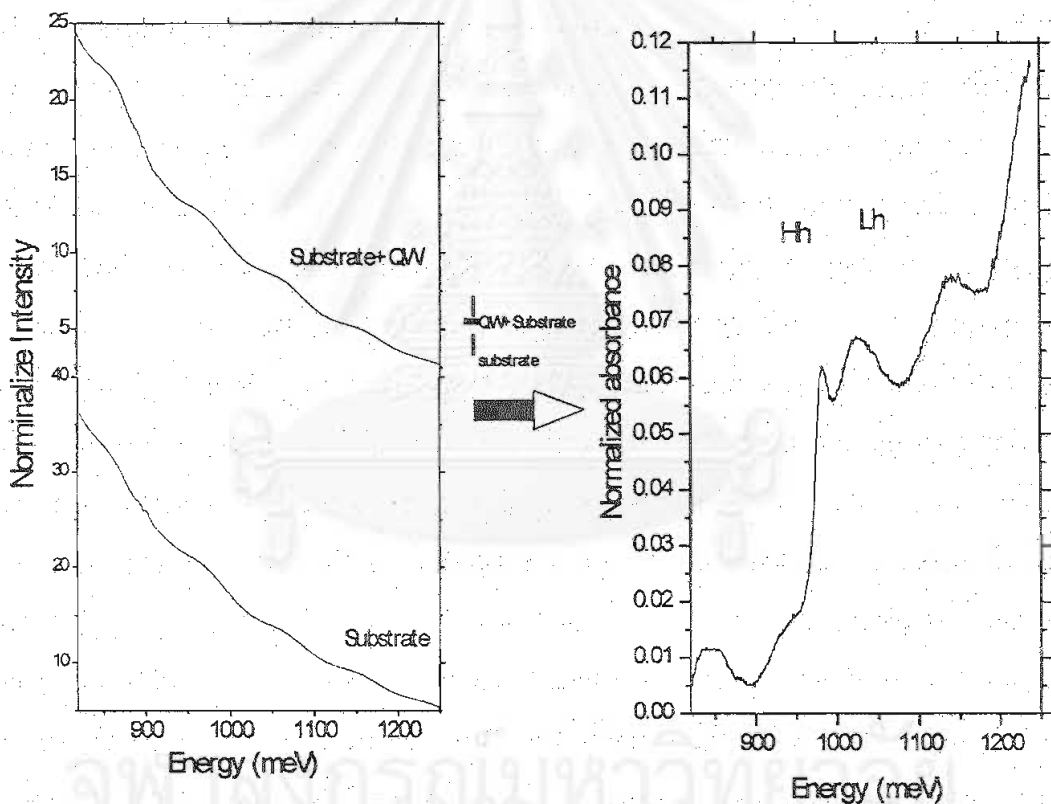


Fig 3.8 schematic of absorbance spectrum obtained by dividing spectrum from QW and substrate sample by spectrum from substrate. Light- and heavy- hole $n=1$ transitions are obtained.

III.2 Rapid Thermal Annealing method (RTA)

Quantum well intermixing of III-V semiconductor compounds has been studied for several years. Annealing method plays a very important role to get a right information. Now we would introduce some annealing method and specify the most regularly used annealing in this thesis. There are several widely annealing methods for III-V semiconductors such as encapsulating the sample with a dielectric, As overpressure, ultra-fast heating and capless method. In *Encapsulating the sample with a dielectric cap technique* [61] [62], the encapsulation is performed to prevent degradation of the surface of the sample. This method requires the furnace to be large to accommodate the entire plumbing requirement. However, disadvantage of this method are (i) induced stresses during the annealing thermal expansion mismatch, (ii) long heating time because of large thermal mass of the furnace, and (iii) slow turn around because of the need to completely flush the P-containing gas after the anneal and before removing the wafer. Moreover, purity of gas and clean gas line is required in order to minimize contamination on the surface of sample. Other technique is *As-overpressure*. [63] This technique is required to introduce alkyl compound such as PH_3 or AsH_3 into heating chamber or to transport phosphorus vapor into chamber in order to suppress P or As loss from the InP or GaAs, respectively. This method allows for controlled variation in the group-V overpressure, but logistically it is usually only available for anneals performed within the growth chamber. *Ultra-Fast heating technique* is another way to anneal the sample. Either laser or e-beam with pulse width less 10^{-6} sec is used to anneal the InP for a very short period. Only the sample surface is heated while the rest of the wafer is essentially at room temperature. This method has proven inappropriate for III-V semiconductors for three basic reasons. First reason is that there can be significant evaporation of the surface even during these short pulse widths. The melt depth is typically about 1 microns, and the regrowth is by liquid phase epitaxy. Second reason is that post-laser annealing thermal cycling leads to large reductions in implanted

dopant carrier concentration. This is a result of the release of a high density of "quenched in" defects created during quench from the melt temperature. The instability of the carrier concentration to subsequent low temperature (about 400 C) annealing precludes the use of pulsed laser annealing for device applications. Another practical drawback of pulse heating method such as laser or e-beam annealing is that complete wafers can not be annealed without a cumbersome step and repeat process since the spot size are generally only a few nm in diameter. *Capless technique* [64] is a technique in which the target wafer is placed face-to-face with another uncapped wafer, and the ensemble is rapidly heated up in a short time. Proximity can be non-reactive material such as Si substrate or III-V semiconductors such as InP or GaAs substrate. Susceptor is also used in this case, especially for large wafer (~1-2 inch diameter). InP wafer is one of the most commonly used for research studies in III-V semiconductors. Using III-V semiconductors as a proximity cap provides a better group-V overpressure than using Si as a proximity cap. This is especially important for anneals above about 650 C but the III-V capping substrates degrade with use and need to be replaced on a regular basis. GaAs proximity caps can be used for 5-10 anneals, while InP proximity caps could be used 2-5 times before a degradation of the surface. In this thesis, we will emphasize on using III-V compound wafers as a proximity cap. We will deeply detail the rapid thermal annealing (RTA) setup system and the sample preparation procedure for RTA in the following section.

Rapid thermal annealing with InP or GaAs proximity cap is one of the well-known methods to allow defects to diffuse from the damaged region through the QWs. Oven is mainly use for annealing sample. The oven made by AG associates is a small oven that heats the samples from the light given off by high-voltage tungsten halogen lamps. A schematic is given in fig 3.9. There are two banks of lamps, one above and below the sample chamber. The chamber walls are made of high purity quartz, and the sample is held in the center of the chamber using a quartz tray. Several small samples can be placed at the same time on a carrier wafer that is supported by the tray. The oven

specifications claim linear ramp-ups in temperature from 10 C/s to 300 C/s, and hold a steady state value to within ± 1 C. Ideally a RTA will heat-up and quench samples very rapidly such that there is no influence of the ramp-up and down times on physical processes. However, very rapid heating and cooling may induce thermal stresses on large diameter wafers, due to the

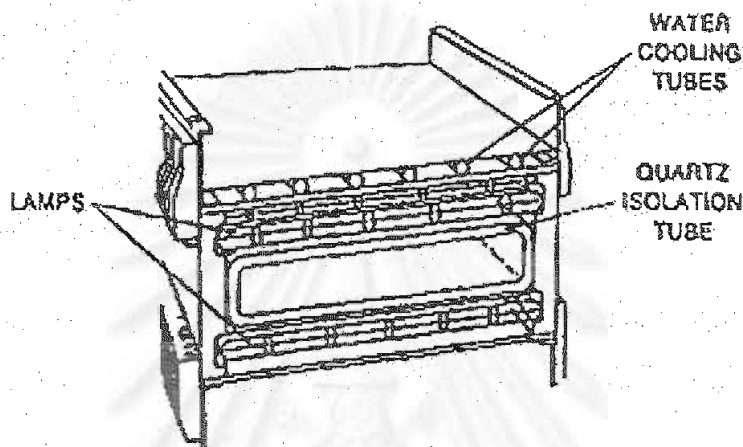
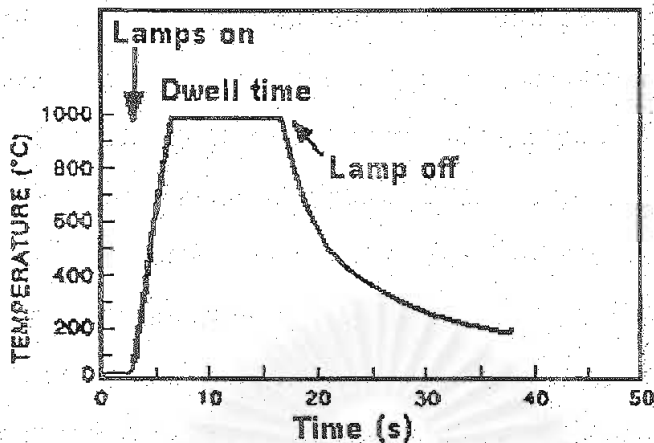


Fig 3.9 Inside view of a commercially available RTA furnace. The wafer is inserted into the quartz isolation tube and heated by infrared and visible radiation from the lamps arranged on each side of the isolation tube.

differences in the heat loss at the edges of the sample compared with the center. Although the samples in this thesis were much smaller (size of our sample is 5x5 mm) and thus these stresses should not be an issue, relatively slow rates were employed such that the results would be transferable to full wafers. Thus values of the order of 20 C/s were employed for ramp-up, while the ramp-down, which is quite non-linear, also averaged about 20 C/sec during the first 100 C drop. This typical time-temperature profile of a sample during RTA is illustrated in Fig 3.10.

Thermo-couples (TC) with embedded junction (using appropriate cement) exposed to the chamber gas are used as shown in fig 3.11. These TCs give accurate measurements for temperatures below about 1050 C. The bare wires are protected using soft weave ceramic



Figs 3.10 Typical time-temperature profile of a sample during rapidly thermal annealing (RTA) which using in this thesis.

tubing. The two ends are connected to chromel and alumel leads integrated within the oven door. The voltage across these is converted to a temperature by circuitry in thermal to the oven.

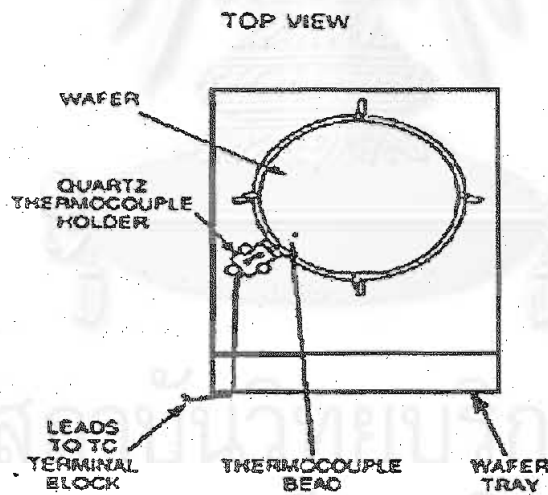


Fig 3.11 Thermocouple using in this thesis.

Pre-conditioning the oven was an important step to take before samples were loading into the oven in order to confirm that operating correctly work and to greatly increase the reproducibility. During the annealing process, ovens are purged with a non-reactive gas (VLSI grade N_2 was used). Outside the chamber, water and air cooling systems keep the rest of the unit cool.

In order to further reduce thermal gradients across small samples, as well as prevent loss of group-V species at the sample's edges, additional III-V sacrificial material was used to surround the samples during anneals. With use of a border, the uniformity of a shifted sample was typically governed by non-uniformity in the starting material. Although the composition of the border was not important, its thickness was found to be an important parameter. If the border is thinner than the sample, the proximity cap will be supported by the sample. Any variations in the distance between the two nominally contacting surfaces (such as that caused by a dirt particle) could cause a hot spot and/or tilt the proximity cap, resulting in a non-uniform blueshift. It is illustrated in Fig 3.12

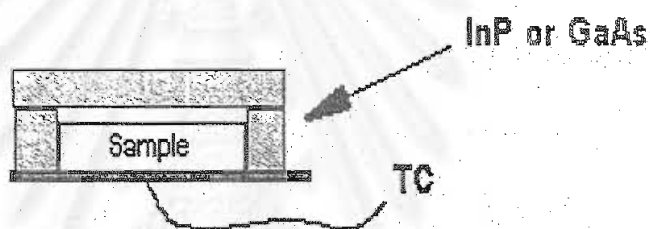


Fig 3.12 Schematic of placing sample.

According to our experience, we found that surface degradation can be a real problem, especially as temperature increases. Since group-V species easily volatile on InP and GaAs substrate, it is essential to protect the surface of sample by minimizing loss of P or As atoms. Since the vapor pressure of P is several times larger than that of As, it may be preferable to terminate an InP epitaxial structure with InGaAs. An upper InGaAs cap is common in device structures due to its good p-type doping capabilities. Logically, one would cap InGaAs with a GaAs proximity cap, and InP with an InP proximity cap, although Pearton [65] suggests that As overpressure could be used to protect InP. An investigation was performed by Joan H. Haysom to determine whether a significant difference existed between using an InP or GaAs proximity cap

when the structure is InP terminated. This was of particular interest because GaAs substrates are significantly cheaper than InP substrate.

Obtaining clean samples is an essential set in the RTA process. A simple three solvent clean followed by de-ionized water rinse was used for the samples after any possible contamination, such as mounting for 4K PL and implantation. Three solvents used are Trichloroethylene, Acetone, and Isopropyl. Those solvents are used in order because previous solvent is soluble in the next liquid. Cleaning process is illustrated in table 3.1. It starts from the first line to the end of the table.

Table 3.1 Cleaning process for RTA.

Solution	Time (mins)	Conditions
1. Trichloroethylene (T.C.E.)	5	
rinse the sample with de-ionized water for 2-3 mins		
2. Acetone	5	
rinse the sample with de-ionized water for 2-3 mins		
3. Isopropylene	5	
rinse the sample with de-ionized water for 2-3 mins		
4. de-ionized water	5	

III.3 Implantation.

Ion implantation technique followed by annealing process is one method to enhance blueshift in the QWI semiconductors; however, implanted method cause increased linewidths of PL and reduced optical efficiency. This technique introduces excess defects such as interstitial, antisites, vacancies, and various defect complexes into the selected region of wafer. Rapid thermal annealing (RTA) process release mobile defects, which cause QWI. Implantation simulation is a powerful tool to predict how deep the implanted ion can go

through the wafer during implantation. Transport of ion in matter (TRIM) is simulation that we use in this thesis. Some physical implantation is reviewed in section 3.3.1. Detail of this program is in section 3.3.2.

III.3.1 Principle of ion implantation.

Implantation depth in semiconductor material can be separated into shallow and deep implanted level. If defects are created above the QW region, it is named shallow implantation. If the defect go deeper than above condition, it is called deep implantation. The created damages cause more intermixing. In order to keep the end-of-range damage spatially separated from the QWs and thereby minimizing and reduction in their optical efficiency, it is preferable to choose implantation energy having an end-of-range above the QWs.

Since implanted ion is accelerated in electric field and implanted into a solid, penetration of implanted ion through the solid depends on accelerating voltage, the mass of ions, atomic mass of solid. After these ion travels in a medium for a while, the slowing down of ions occurs mainly due to electronic and nuclear slowing down. *Electronic stopping power* that mainly effects to moving of implanted ion in medium is inelastic collisions between electrons and the ion moving through it. Generally electronic stopping power is defined as a function of energy which is an average taken over all energy loss processes for different damage states. On the other hand, *nuclear stopping power* that depends on repulsive potential between two atoms is elastic collisions. When the ions are slowing down sufficiently, the collision with the nuclei become more probable. Then this type of stopping power is dominant. If atoms of the target gain significant recoil energy, they will leave their lattice positions and produce a cascade of further collision in the lattice.

The amount of damage and the implanted depth depend on type of ions, implanted energy, implanted dose, target temperature, and angle of incidence.

Energy of implanted ion

The more energy is, the deeper implanted ion can go through. Energy of implanted ion is varying between 100 eV and 700 MeV, depend on type of material and several factors.

Implanted dose

Dose is the main means of adjusting the number of defects created and magnitude of blueshift. One expects there to be a minimum threshold dose below which no measurable blueshift occurs due to lack of damage, and a maximum dose, above which the microstructure in the implanted material has become so altered that it inhibits the release of the mobile defects causing intermixing. These minimum and maximum dose are somewhat dependent on material, implant energy, and anneal conditions, but generally are in range of 10^{11} cm^{-2} and 10^{15} cm^{-2} , respectively.

Temperature of material during implantation process

The temperature of the sample during implantation is a critical parameter for the successful application of the P implantation technique. The NRC/UWO group found that room temperature implants result in very little blueshifting, while raising the sample temperature in the 50 to 200 C result in increases in the blueshift. Two possibilities can be,

- (a) The higher temperature allows the defects to diffuse further away from the center of implant damage track, where they might otherwise be locked up.
- (b) The temperature alters the relative concentrations of different defects, with more of the mobile intermixing-causing defect being formed at higher temperatures. Implanting at 200 C has also shown to be beneficial poor electron mobility and carrier concentrations for doping implantation.

Angle of incident beam

Ion trajectory can effect to the further penetrated depth of implanted ion if implanted channel is parallel to a lattice plane of crystal. To avoid this

problem, we implanted ions are implanted in a non-channeling angle into a medium.

III.3.2 Implantation Simulation

According to our background knowledge of implantation in the above discussion, I would now introduce simulation using in this thesis, the Stopping and Range of Ion in Matter (SRIM) and the Transport of ion in Matter (TRIM) [66][67][68]. SRIM and TRIM are based on Monte Carlo method. This simulation can calculate ion interactions with multi-layer complex targets by using quantum mechanical treatment of ion-atom collision. TRIM simulation accepts complex targets made of compound materials with up to eight layers, each of different materials. 3D distribution of the ions and also all kinetic phenomena associated with the ion's energy loss (target damage, sputtering, ionization, and phonon production) is also available in TRIM.

These simulations consist of four main parts. First part focuses on setup the ion and target. Run the calculation is in the second part. Third part is concentrated in interrupt the calculation to look at plots of distribution. Final part is save data files of all the detail.

Assumptions of TRIM and SRIM are based on, (1) Target material is amorphous with atoms in random position and (2) Ignore the directional properties of the crystal.

These simulations are composed of 6-mode calculation. First mode is Ion distribution and quick calculation of damage. This option should be used if the user does not care about details of target damage or sputtering. The damage calculated with this option would be the quick statistical estimates based on the Kinchin-Pease formalism. Second mode is calculation with full damage cascades. This option follows all of recoil until its energy drops below the lowest displacement energy of any target atom. Hence all collision damage to the target is analyzed. Third mode is calculation of surface sputtering. These allow you to analyze the effect of small variations on the surface binding

energy on the sputtering yield. This parameter is at the heart of sputtering, and its value is sometimes difficult to estimate. Fourth mode is concentrated on neutron/electron/photon cascades. This option is used to calculate only the damage cascades in a target. Generated of calculates the energy transfer to target atoms by neutrons, electrons or photons. TRIM takes this information and calculates the damage done to the target from recoil cascades. Fifth mode is various ion energy/angle/positions. This option allows TRIM with ions starting at various energies, or with varying trajectory angles to the target surface, or starting at various depths in the targets. Typical calculations of ions are from diffuse plasma, or from target with a receding surface due to rapid sputtering, or reactor radiation damage to metals. The last mode is special multi-layer biological targets. In this thesis will using the last mode to simulate implanted data.

The displacement energy, surface binding energy, and the lattice binding energy are important parameters in SRIM and TRIM simulation. *The displacement energy* is that recoil needs to overcome the lattice forces and to move more than one-atomic spacing away from its original site. If the recoiling atom does not move more than one lattice spacing, it is assumed that it will hop back into its original site and give up its recoil energy into phonons. Typical values are about 15 eV for semiconductors. To give a picture in our mind, Good example is given here. Assume an incident atom has atomic number Z_1 and energy E . It has a collision within the target with an atom of atomic number Z_2 . After the collision, the incident ion has energy E_1 and the struck atom has energy E_2 . E_d and E_b are the displacement energy and the binding energy of a lattice atom to its site, respectively. E_f is the final energy of moving atoms. If $E_2 > E_d$ (the hit atom is given enough energy to leave the site), *a displacement* occurs. If both $E_1 > E_d$ and $E_2 > E_d$ (both atoms have enough energy to leave the site), *a vacancy* is happened. If $E_2 < E_d$, then the struck atom does not have enough energy and it will vibrate back to its original site, releasing E_2 as phonons. If $E_1 < E_d$ and $E_2 > E_d$ and $Z_1 = Z_2$, then the incoming atom will remain at the site and the collision is called a *replacement collision*

with E_1 released as phonons. The atom in the lattice site remains the same atom by exchange. This type of collision is common in single element targets with large recoil cascades. If $E_1 < E_d$ and $E_2 > E_d$ and $Z_1 \neq Z_2$, then Z_1 will become a *stopped interstitial atom*. Finally, if $E_1 < E_d$ and $E_2 < E_d$, then Z_1 becomes an interstitial and $E_1 + E_2$ is released as phonons. If a target has several different elements in it, and each has different displacement energy, then E_d will change for each atom of the cascade hitting different target atoms. Sputtering on the surface is main effect of surface binding energy. Surface binding energy is not only the traditionally chemical binding energy for surface atoms but also all surface non-linearity energy effect such as those produced by radiation damage, surface relaxation, surface roughness. Sputtering energy is the energy that target atoms (sputter atom) can overcome to leave the surface of the target. Sputtering is the removal of near-surface atoms from the target. When a cascade gives target atom energy greater than the "surface binding energy" of that target, the atom may be sputtered. To actually be sputtered, the atom's energy normal to the surface must still be above the surface binding energy when it crosses the plane of the surface. The sputtering of a surface is described by a "*Sputtering Yield*", which is defined as the mean number of sputtered target atoms per incident ion. If the target is made of several elements, there is a separate sputtering yield for each element. The sputtering yield is very sensitive to the surface binding energy, which you input to the calculation. Be aware that for real surfaces, this changes under bombardment due to surface roughness, and also due to changes in the surface for compounds. Furthermore, sputtering involves mostly the upper monolayers of the target. The lattice binding energy is the energy that every recoiling target atoms loses when it leaves its lattice site and recoils in the target. Typically it is about 1-3 eV, but values are not known for most compounds. This energy is assumed to go into phonons. The lattice binding energy is, unfortunately, rather significant in calculating sputtering yield.

During the collisions, the ion and atom have a screened Coulomb collision, including exchange and correlation interactions between the

overlapping electron shells. The Charge State of the ion within the target is described using the concept of effective charge, which includes a velocity dependent charge state and long range screening due to the collective Electron Sea of the target. TRIM does not include the necessary density corrections to allow accurate evaluation of stopping powers and not include any nuclear reaction analysis. So that ions with energies above 5 MeV/amu may have inelastic energy losses which are not included.

III.3.3 Parameter of simulation

When we start the SRIM or TRIM, below parameters is needed to fill,

1. Ion Name, ion mass, ion energy. Unit of ion mass and ion energy is commonly in amu and keV, respectively.
2. Layer depths, layer density, layer name. Unit of layer depth is in angstroms. We may also used unit of microns, millimeters, meters or kilometers by using the indicated abbreviations. Unit of layer density is in g/cm^3 .

Main structure studied in this thesis is based on InP and InGaAs. Atomic mass and density of those compounds are illustrated in Table 3.2.

After we computer finished calculation by using above value, data in Range.txt and Vacancy.txt was needed to be plotted the number of implanted ion or vacancies as a function of implanted dose in order to obtain suitable implanted dose. Finally, the implanted energy is extracted by using a rule of thumb that is used by the group. Ion implanted dose should drop by 10^3 from the peak concentration at a distance of about 0.5 above the QWs. Good recovery of PL intensity following processing has been observed following this rule. We found that tilted by 7 and twisted by 20 could minimize channeling effects. Our samples were implanted with a 1.7-MeV Tandatron accelerator by our collaborators, M.I. Tomson, at University of Western Ontario.

Table 3.2 Density and atomic mass, mass number of atom and compound using this thesis.

Atoms	Z	Mass (amu)
In	49	114.82
Ga	31	69.72
As	33	74.922
P	15	30.974

Compound	Density
InGaAs	5.5
InP	4.72
InGaAsP	5.499

สถาบันวิทยบริการ
จุฬาลงกรณ์มหาวิทยาลัย

CHAPTER IV

EXPERIMENTAL RESULTS

In this chapter, results are presented pursuant to the goals that were fixed in chapter one, namely: 1-To quantify the interdiffusion length experienced by group-III and group-V atoms in $\text{In}_x\text{Ga}_{1-x}\text{As}_y\text{P}_{1-y}/\text{InP}$ QW heterostructures of different barrier/well composition after disordering, 2-Investigate means to assess residual damage in intermixed $\text{In}_x\text{Ga}_{1-x}\text{As}_y\text{P}_{1-y}/\text{InP}$ QW heterostructure. Thus in section 4.1 an Interdiffusion model is used to compare with experimental results and evaluate the ratio of diffusion length of group-III and that of group-V atomic species in $\text{In}_x\text{Ga}_{1-x}\text{As}_y\text{P}_{1-y}/\text{InP}$ QW heterostructures. Several techniques are able to introduce defects into the semiconductor material in order to enhance intermixing process in interface area between QW and barrier: impurity-induced disordering [69][70], laser-induced disordering [71], impurity-free vacancy disordering [72][73], implanted induced disordering [74] and low-temperature growth induced disordering. In this study, the defects have been created in the material using two different methods: ion implantation and grown-in defects. In section 4.2, we initial carrier lifetime studies of intermixed $\text{In}_x\text{Ga}_{1-x}\text{As}_y\text{P}_{1-y}/\text{InP}$ QW heterostructures. Such measurements techniques were applied successfully in the past for GaAs/AlGaAs QW heterostructures. The possibility of applying this method to InGaAsP/InP QW structures is investigated.

IV.1 Determination of the interdiffusion constants.

In this section, the interdiffusion constant is measured for lattice-matched and tensile strained InGaAs/InP multiple QW structures. The samples used are first introduced, then the results of PL measurements are introduced to quantify the amount of intermixing undergone by each sample, and finally

transmission measurements are presented and the results are compared with calculations to obtain interdiffusion constants.

IV.1.1 structure of samples.

Three 2-inch wafers were grown by Chemical Beam Epitaxy (CBE) on InP substrate in order to carry on study in this thesis. Two of them, namely CBE99-172 and CBE99-064 were lattice matched MQW samples, and CBE00-120 was a tensile strained MQW sample. All samples has similar layer structures with from substrate to top an InP buffer layer followed by the InGaAs MQW layers with InP barriers, followed by a 1.6 microns cladding layer and finally an $\text{In}_{0.53}\text{Ga}_{0.47}\text{As}$ cap was grown on the top in all wafers in order to prevent evaporation of group-V atoms from the surface during rapid thermal annealing[75]. The 1.5-micron InP Cladding layer of CBE99-172 wafers were grown at standard substrate temperature of 505 C and served as a target layer for ion implantation. In samples CBE99-064 and CBE00-120, the

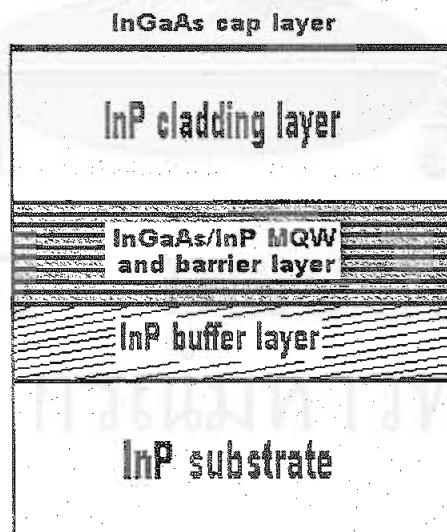


Fig 4.1 Schematic representing the sample in cross-section. Those three wafers have similar cross-section structure but different in Ga composition in QW layer and the width of each layer as listed in table 4.1

Table 4.1 structure of sample.

	CBE99172		CBE99064		CBE00120	
	Description	Depth	description	depth	description	depth
	In _{0.53} Ga _{0.47} As	200 A	In _{0.53} Ga _{0.47} As	300 A	In _{0.53} Ga _{0.47} As	300 A
Cladding layer	InP	1.5 microns	InP	1.6 microns	InP	1.6 microns
					In _{0.53} Ga _{0.47} As	100 A
Buffer layer	InP	250 A	InP	250 A	InP	500 A
Barrier	InP	10x190 A	InP	10x170 A	InP	8x160 A
QW	In _{0.53} Ga _{0.47} As	10x50A	In _{0.53} Ga _{0.47} As	10x50A	In _{0.455} Ga _{0.545} As	8x50A
Buffer layer	InP	3000A	InP	3000A	InP	3000A
Substrate	InP		InP		InP	

cladding layer was grown at 470 C to introduce grown-in defects, thus removing the necessity of implantation to introduce defects. Result using both types of intermixed layers will be compared. The cross-section structure of these wafers are illustrated in fig 4.1 and details of each wafers is shown in table 4.1.

In order to evaluate the thermal stability of our samples, only rapid thermal annealing process was performed at high temperature. First, we present the knee curves for our samples. Then perform ion implantation studied on the sample that did not have grow-in-defects, the results will be discussed later in order to promote interdiffusion.

As a first step in the process of intermixing QW samples, it is good practice to perform a series of RTA on as-grow pieces of the wafer in order to evaluate the thermal stability of the structure. This is useful to determine a temperature range with RTA process before implantation is performed on CBE99-172 in order to maximize the selectivity of the shifts between the implanted and non-implanted regions of the sample. Annealing temperature must be hot enough to allow these defects to diffuse from the damaged region through the QWs, and also repair the implantation damage. However, if it is

too hot, a large equilibrium generation of lattice defects occurs in non-implanted region, resulting in unwanted intermixing [76][77][78]. The different wafers were thus cleaved into several pieces approximately 5x5 mm in size. Each piece was identified by a scribe mark and then annealed separately at different temperatures for a controlled amount of time. The temperature evolution during the annealing was monitored using a chart recorder to insure temperature stability better than 5 degrees Celsius. PL measurements were performed on each piece before and after the annealing. The difference in PL peak position induced by the RTA process is thus obtained to measure the amount of interdiffusion induced in the sample. For example, figure 4.2 shows the PL map performed on non-annealing (a) and

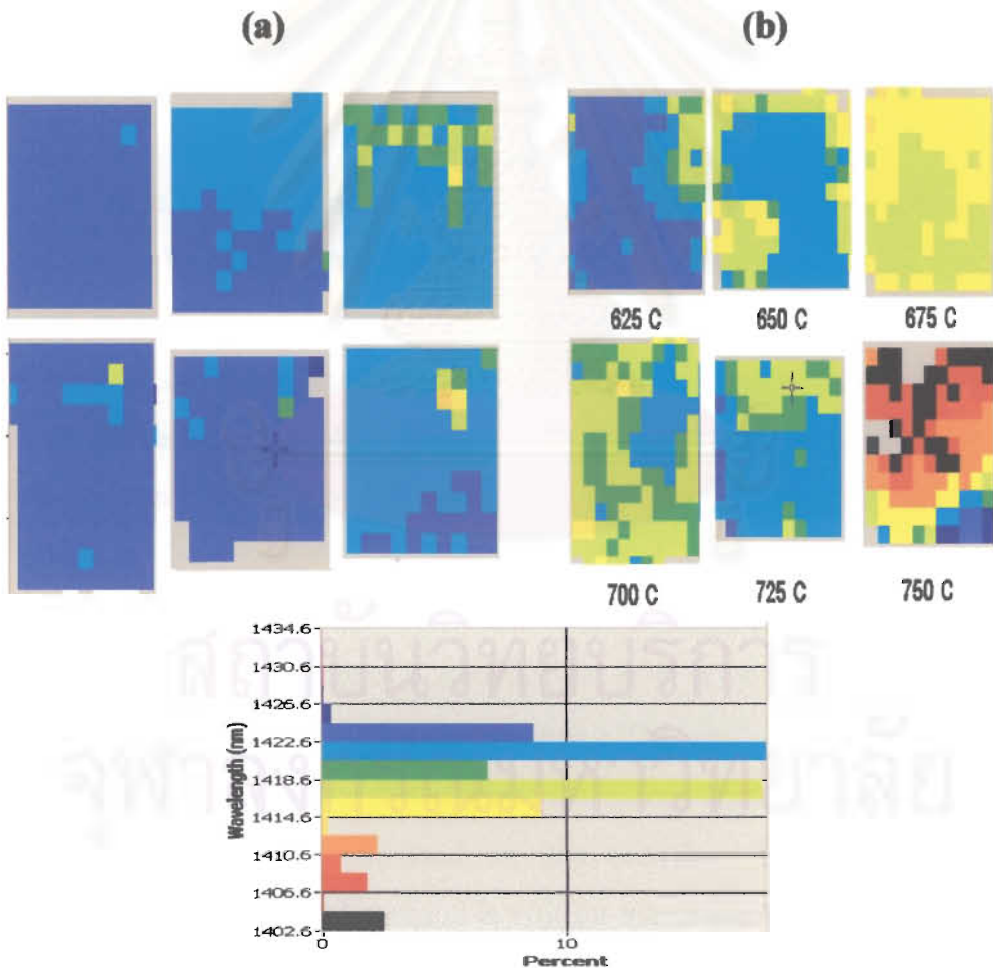


Fig 4.2 schematic of PL map performed on non-annealing (on left handside) and annealed (right handside) at different temperature in range 625 C to 750 C for 60 sec-total-time of Sample CBE99-172.

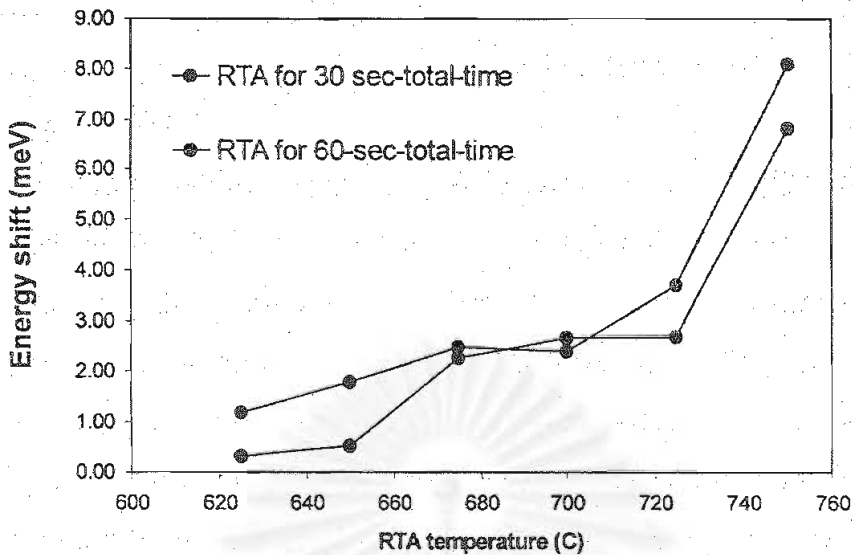


Fig 4.3 Evolution's CBE99-172 sample of energy shift from PL mapping in figure 4.2 plotted as function of annealing temperature in step of 25 ° C for 60 sec-total time.

annealed (b) pieces of sample CBE99-172. This sample was annealed for 60 sec-total-time by varying temperature. PL spectra of non-annealing pieces are uniform but are less uniform after annealing process is performed. The resulting PL shifts obtained at different annealing temperatures from these maps are plotted in figure 4.3. These curves are commonly referred to as "knee curves" due to the fact that one often observes a critical temperature marking the onset of the interdiffusion process. Indeed, one can see that below a temperature of about 725 C, the PL shift obtained from annealing is negligible, while above that temperature a measurable shift is obtained, indicating the onset of the thermal interdiffusion process. The shifts obtained are overall reasonably small (~ 8 meV). To enhance the energy shift, implantation process followed by RTA was performed on this sample. When performing the annealing on the implanted sample, it will be important to keep the annealing temperature below the knee temperature to prevent thermal interdiffusion. In this way we work in a regime that maximizes the contrast of bandgap shifts between implanted and non-implanted regions of the sample. So the reasonable annealed temperature is in range of 625 °C and 725 °C. Annealed

temperature should be hot enough to allow defects move to active QW layer and not too hot. Thus, we found the well suitable thermal-stability temperature of this sample is 700 C.

The shifts obtained from growth-in-defect samples (CBE99-064 and CBE00-120) as shown in fig 4.4 and 4.5 are larger than those obtained from CBE99-172 (fig 4.3). This result confirms our ability to introduce defects in the sample during the growth process. Therefore no implantation process is needed to enhance intermixing in the growth-in-defect samples. Defects created by growth-in-defect method evidenced the exact location of the defects (uniformly distribution in the cladding layer) so we can model their motion to the QW. In figure 4.4, blueshift of CBE99-064 sample -the difference of transition energy between non-intermixed sample and intermixed samples- obtained from single-point PL spectra at 4.2 K is plotted as a function of annealing time, increasing in step of 25 C for 360 sec. It is reflected that the higher blueshift was obtained with longer rapid thermal annealing and blueshift is ~183 meV for the highest annealed temperature. This reveals that the enhancement of the intermixing during the early stages of annealing occurs.

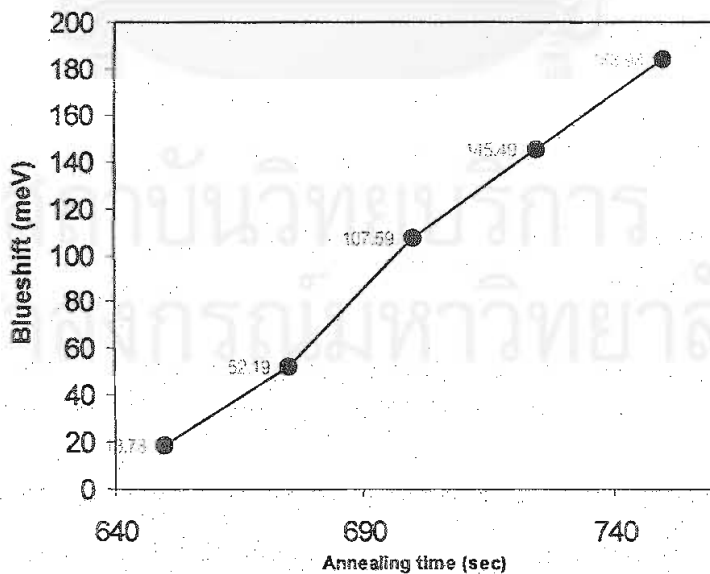


Fig 4.4 Energyshift evolution of CBE99-064 samples plotted as a function of annealing temperature in step of 25 °C for 360 sec-total time.

In figure 4.5, two PL peaks of CBE00-120 samples annealed for 30 sec were appeared after single PL was performed at both 4.2 K and 300 K. We had identified that the lower-energy peak was emitted from 100-A $\text{In}_{0.53}\text{Ga}_{0.47}\text{As}$ (below cladding layer) but the higher-energy peak was emitted from active QW layer. So blueshift of annealed samples was obtained from the higher-energy peak. Blueshift from PL spectra in figure 4.5 is plotted as a function of annealing temperature in step of 25 °C as shown in figure 4.6.

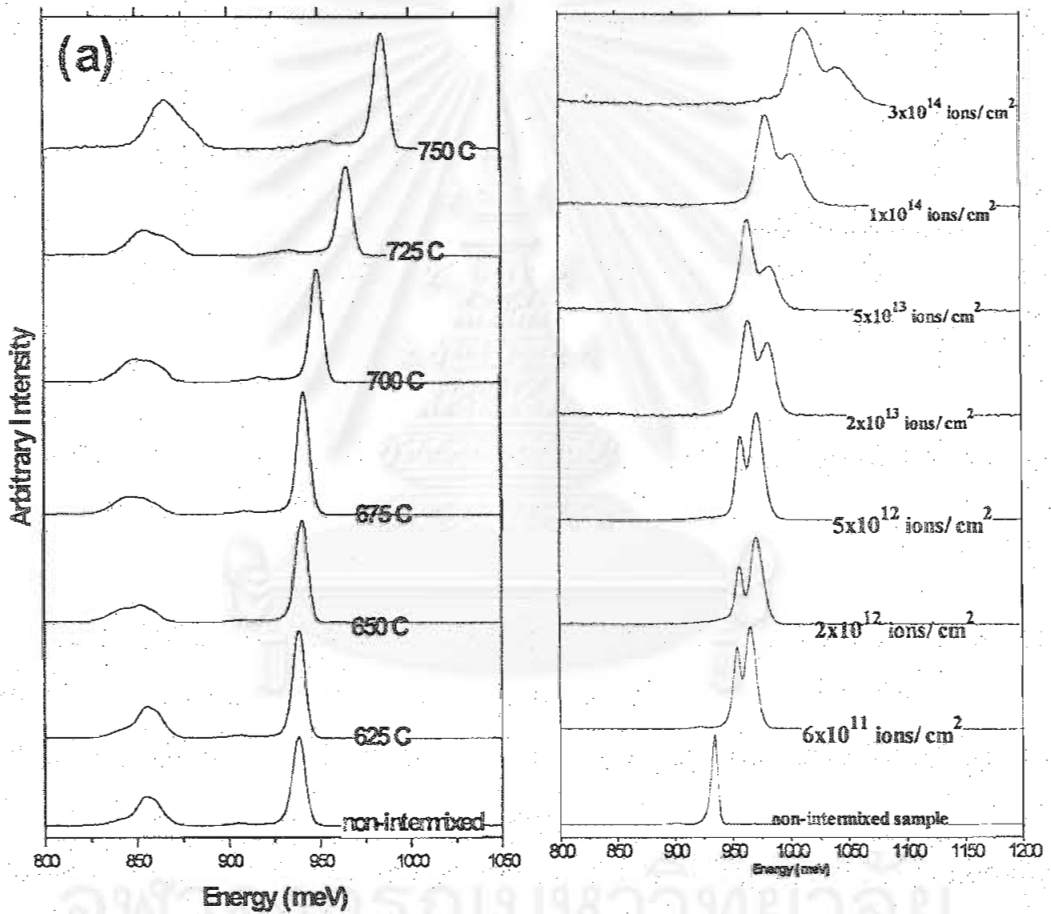


Fig 4.5 PL spectra performed at (a) 4.2 K and (b) 300 K for CBE00-120 samples annealed in step of 25 °C for 30 sec.

The result from those two samples (CBE99-064 and CBE00-120) is confirmed that defects is introduced to QW layer because of rising blueshift with increasing annealed temperature. Other possibilities may be occurred in these two samples is whether tensile strain is introduced in the QW region,

compressive strain will occur between interface area between QW and barrier region. This is illustrated in section II.5.2.

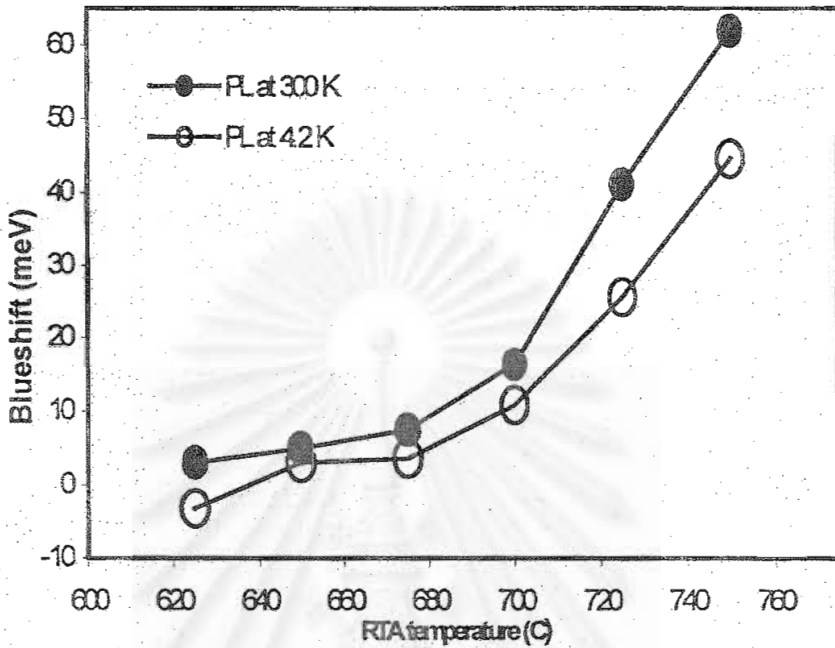


Fig 4.6 Evolution of blueshift of CBE00-120 PL spectra in figure 4.5: opened circle for PL spectra at 4.2 K and closed circle for PL spectra at 300 K.)

As the result of CBE99-172 sample in figure 4.3, a little blueshift is obtained with rising only annealing temperature so defects is need to create above active QW layer by using ion implantation technique in order to enhance the interdiffusion process. Since our samples are $\text{In}_x\text{Ga}_{1-x}\text{As}$ based on InP, P^+ ion is used as implanted ions. To predict the depth of implanted ion penetrated into the samples, simulation (SRIM) described in section III.3 is used. Implanted energy for this sample is varying in range of 550 meV and 1000 meV in order to introduce a number of vacancies and implanted ion above active QW layer. In figure 4.7, density of implanted ions plotted as a function of depths in semi-log scale at different implanted energy. The well suitable implanted energy is obtained by rule of thumb used in our group. Our rule of thumb is that density of implanted ions should drop by 10^3 from the peak

concentration at a distance of about 0.5 microns above the QWs. The result from simulation said that the well suitable implanted energy is ~550 meV.

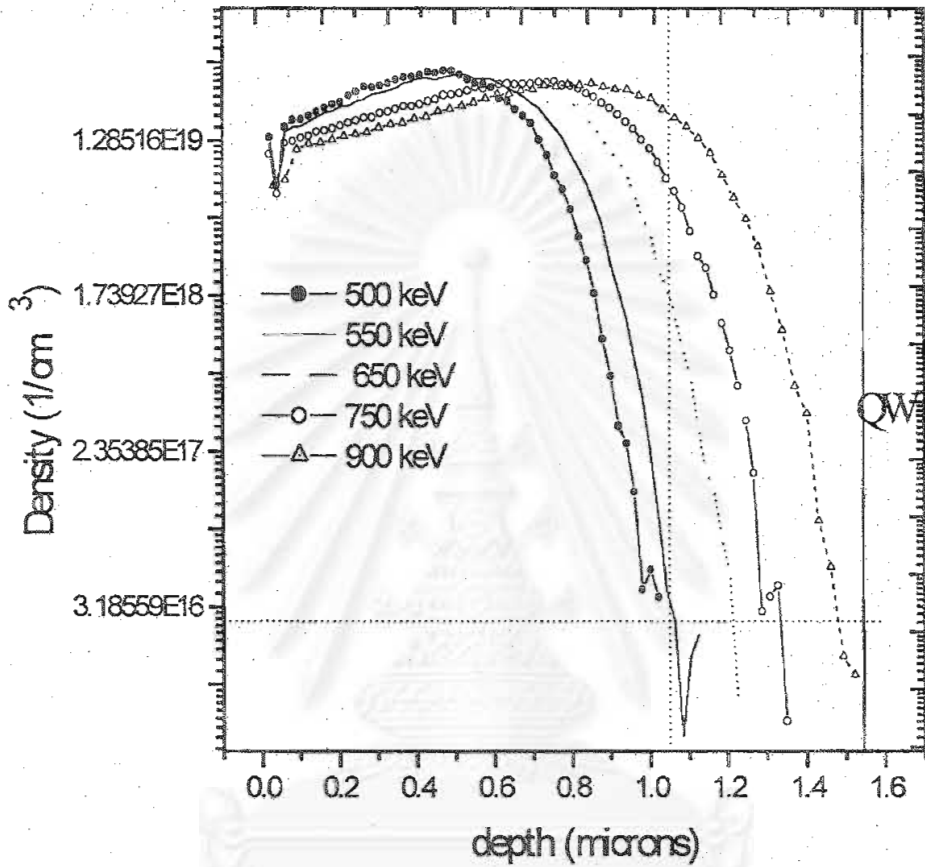


Fig 4.7 Density of implanted ions for CBE99-172 sample plotted as a function of penetrated depth from the surface by using SRIM simulation.

Then CBE99-172 wafer was cleaved into 5x5 mm in size. P^+ ions were implanted in each piece at different implanted dose in range of 6×10^{11} ions/ cm^2 and 1×10^{14} ions/ cm^2 . Our collaborators at the University of Western Ontario, using a 1.7 MeV Tandem accelerator performed implantation process. To diffuse those defects created in cladding down to active QW layer, RTA process is required. As our previous discussion of thermal-stability temperature in figure 4.3, the well suitable annealing temperature is about 700 °C. So implanted pieces were annealed at this temperature for 150 sec-sec

total time. Evolution of single point PL spectra performed at 4.2 K for this sample is plotted as a function of implantation dose in range of 6×10^{11} ions/cm² and 1×10^{14} ions/cm² as shown in figure 4.8. The result said that energy shifted to higher with increasing implantation dose and non-intermixed PL spectra split to double peak with introduction of implantation process together with RTA.

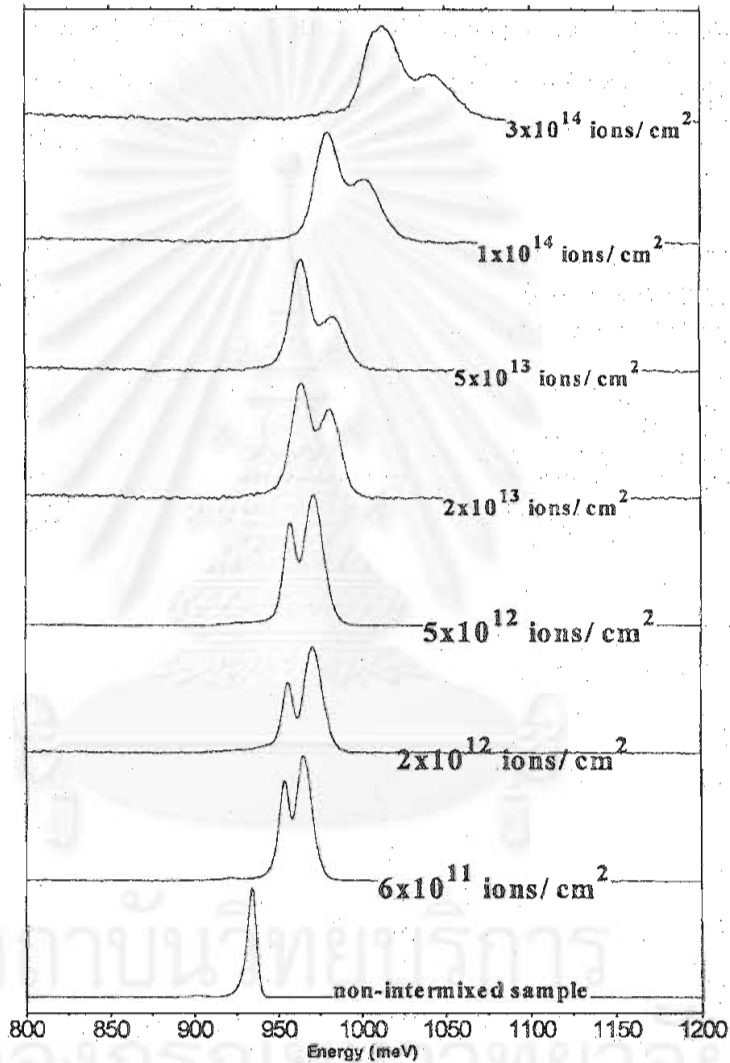


Fig 4.8 Evolution of single point photoluminescence spectra of CBE99-172 sample implanted and annealed for 150 sec-total time. PL was performed at 4.2 K.

To identify those two peaks, carrier population is excited by 490-nm Ar⁺ laser and 980-nm laser diode as shown in figure 4.9. 490-nm Ar⁺ laser excites electron-hole pairs in the barrier band. Then those electron-hole pair thermalize

to the bottom of barrier band and relax to the lowest state in the active QW layer though band-edge in the barrier and active QW. Eventually, Those are recombined and emitted radiative photons. However, photon energy of 980-nm laser diode is below InP bandgap so electron-hole pairs generate in the QW layer. In figure 4.9, one can see that the higher energy peak practically disappears when the sample is excited at 980 nm at photon energies below the InP bandgap. This suggest to us that higher energy peak occurs because carriers created outside the QW region and lower energy peak is from recombination of carrier in the QW region.

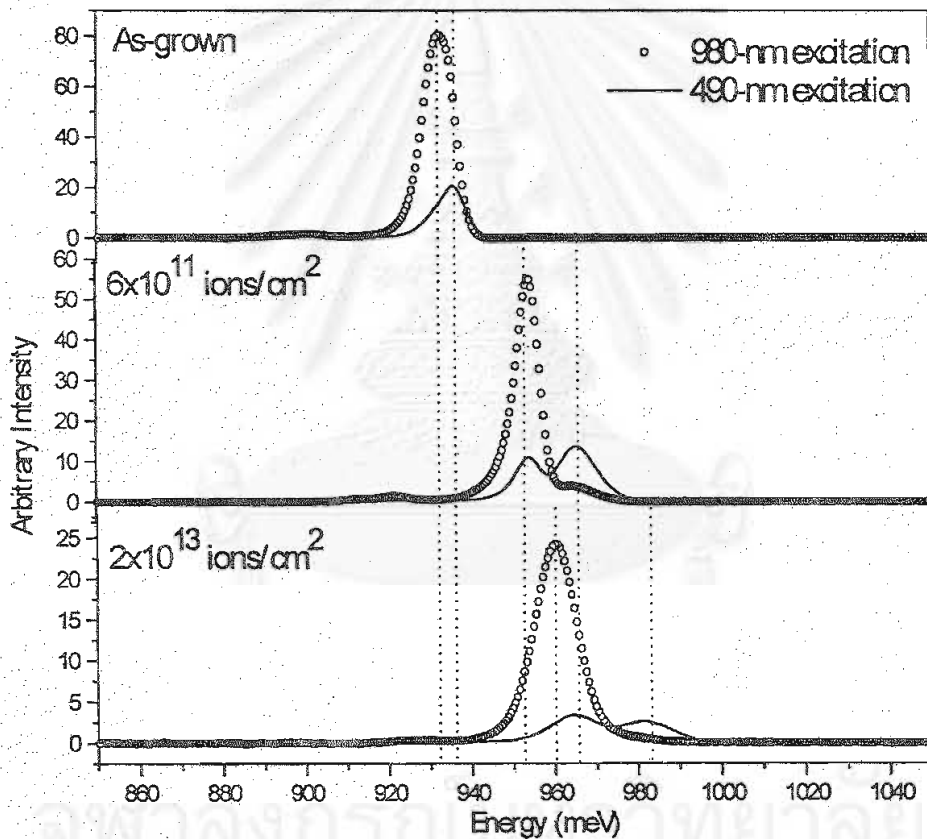


Fig 4.9 Intensity of CBE99-172 samples plotted as a function of energy. This sample is excited by 490-nm Ar-laser and 980-nm laser diode. The above, middle, and bottom figure are from As grown, 6×10^{11} ions/cm² implanted dose, and 2×10^{13} ions/cm² implanted dose sample, respectively.

PL mapping performed on CBE99-172 sample at 300 K as shown in figure 4.10. The result shows that non-uniform is introduced with increasing implantation dose in the intermixed sample. Blueshift obtained from PL spectra obtained at 4.2 K (in figure 4.8) and 300 K (in figure 4.10) is plotted as function of implantation dose as shown in figure 4.11. In figure 4.11, energy shift to higher with increasing implantation dose and the highest energy shift is ~ 70 meV for PL performed at 4.2 K and ~ 90 for PL performed at 300 K. This result confirms us that defects created by implantation technique diffuse down to active QW layer.

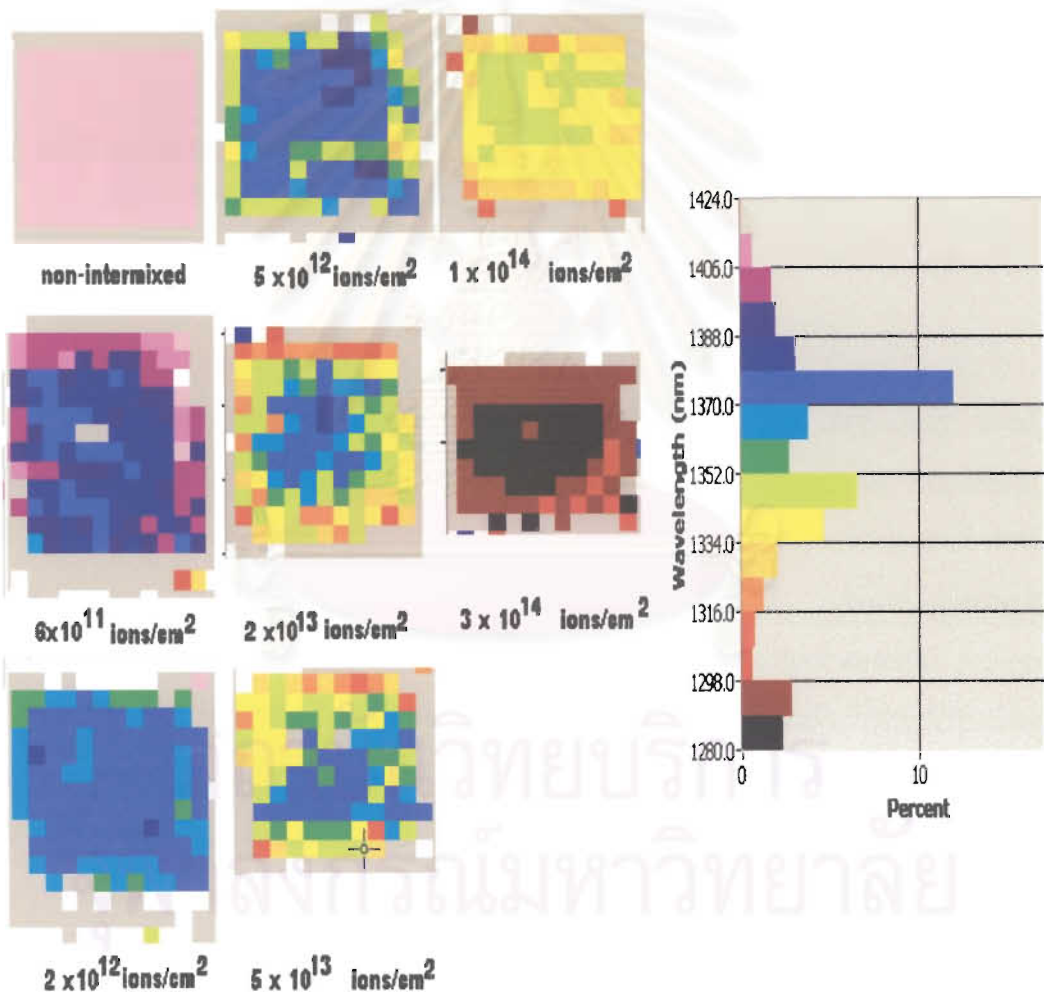


Fig 4.10 Cross-section of wavelength PL spectra of CBE99-172 sample plotted as a function of distance with our PL mapping system. PL mapping is performed at 300 K.

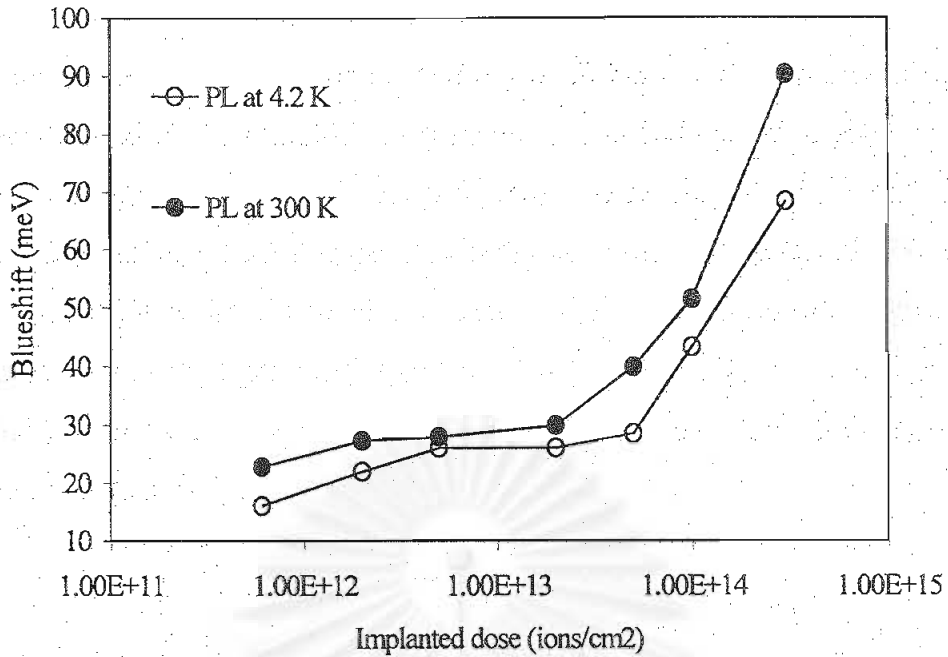


Fig 4.11 Evolution of blueshift as a function of implanted dose for CBE99-172 QW samples annealed at 700 C for 150-sec total time.

IV.1.2 Absorption data

Photoluminescence results in the previous section are only used to obtain energy shift of samples created defects by two methods: implantation QWI technique and growth-in-defect QWI techniques. It confirms that defects move down to active QW layer in three samples. Now absorption measurement together with interdiffusion simulation (experimental set-up in chapter III) is performed on those samples in order to obtain interdiffusion of group-III and group-V species atoms. Splitting between first heavy- (hh) and first light- hole (lh) transition obtains from absorption measurement.

Absorption measurement was performed at 4.2 K on three samples: CBE99-172, CBE99-064 and CBE00-120. For CBE99-172, Absorption spectra for non-intermixed and implanted samples by varying implanted dose are plotted as a function of energy as shown in figure 4.12. The results said that the energy difference between the hh and lh transition (the hh-lh splitting) has decreased in the slightly intermixed sample (a-c) to the point where the hh and lh overlap. In the more highly ion implanted dose sample (c to g), the

slope of the band edge has changed, leading us to believe that lh may now be the lowest transition. Eventually lh transition is now become higher energy than hh transition. The hh-lh splitting was increasing again while ion-implanted dose of intermixed implanted-samples (d-g) was gathered. It may suggest that tensile strain develops in quantum well region and then, off-zone-center maxima in the 'light hole' band can become the highest energy point. The actual transition energy in this material could have an indirect character as described in section II.5.

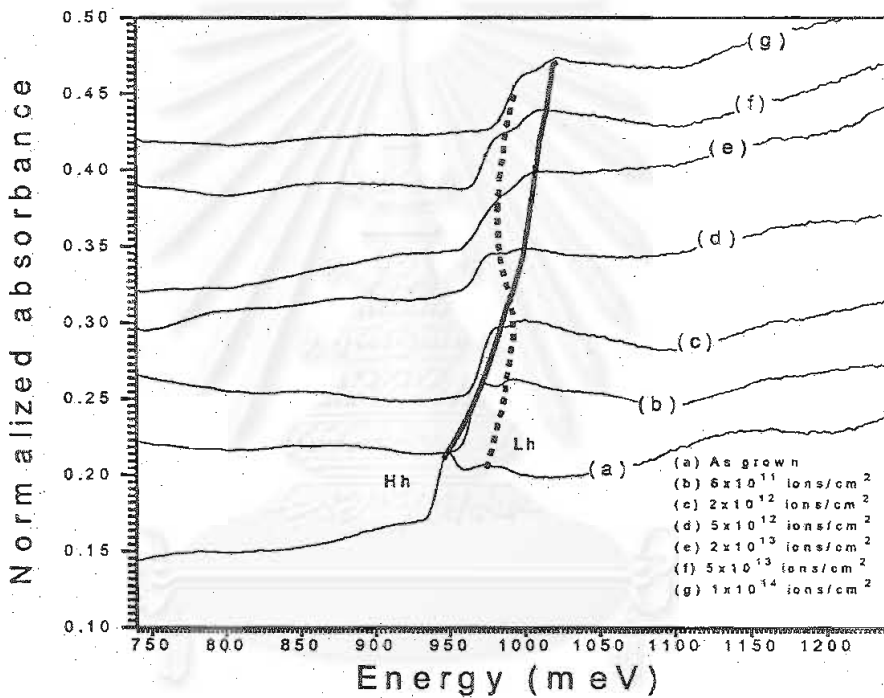


Fig 4.12 Normalized absorbance spectra from CBE99-172 QW sample implanted at (b) 6×10^{11} ions/cm², (c) 2×10^{12} ions/cm², (d) 5×10^{12} ions/cm², (e) 2×10^{13} ions/cm², (f) 5×10^{13} ions/cm² and (g) and 1×10^{14} ions/cm² but (a) non-intermixed sample.

Normalized absorbance spectra for growth-in-defect samples (CBE99-064 and CBE00-120) are plotted as a function of energy as shown in figure 4.13 and 4.14. Splitting between first hh and lh QW transition was gradually decreased with rising RTA temperature up to 725 °C for CBE00-120 samples and up to 675 °C for CBE99-064 sample. At slightly high RTA temperature, those first hh-lh splitting is become overlap and then slope of the band edge has

changed, leading us to believe that the lh-transition may now be the lowest transition energy. The explanation may be that strain rises in QW with increasing RTA temperature as illustrated in section II.5.3. Moreover, overlap between first hh- and lh-transition of CBE00-120 sample occurs at higher RTA temperature, compare to that of CBE99-064 sample because CBE99-064 sample is annealed for long total time than CBE00-120.

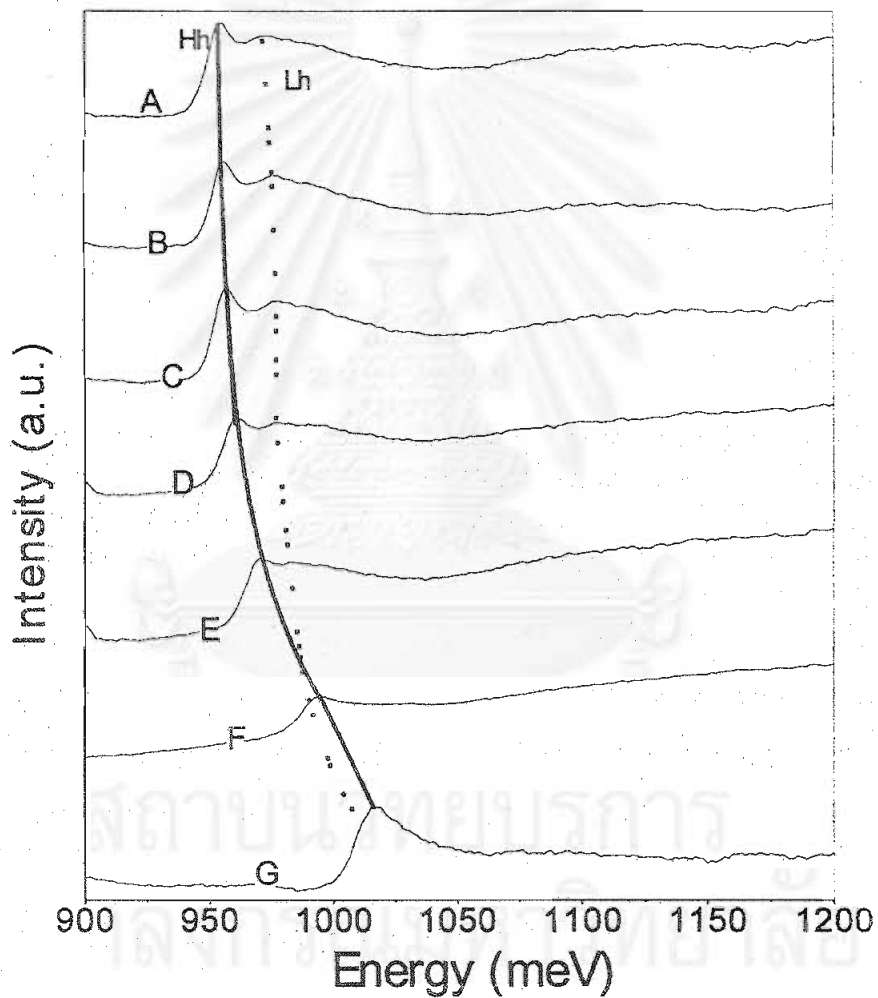


Fig 4.13 Normalized absorbance spectra of growth-in-defect CBE00-120 sample annealed at different temperature for 30 sec. Each piece was annealed (B) at 625 C, (C) at 650 C, (D) at 675 C, (E) at 700 C, (F) at 725 C, and (G) at 750 C but (A) non-intermixed piece.

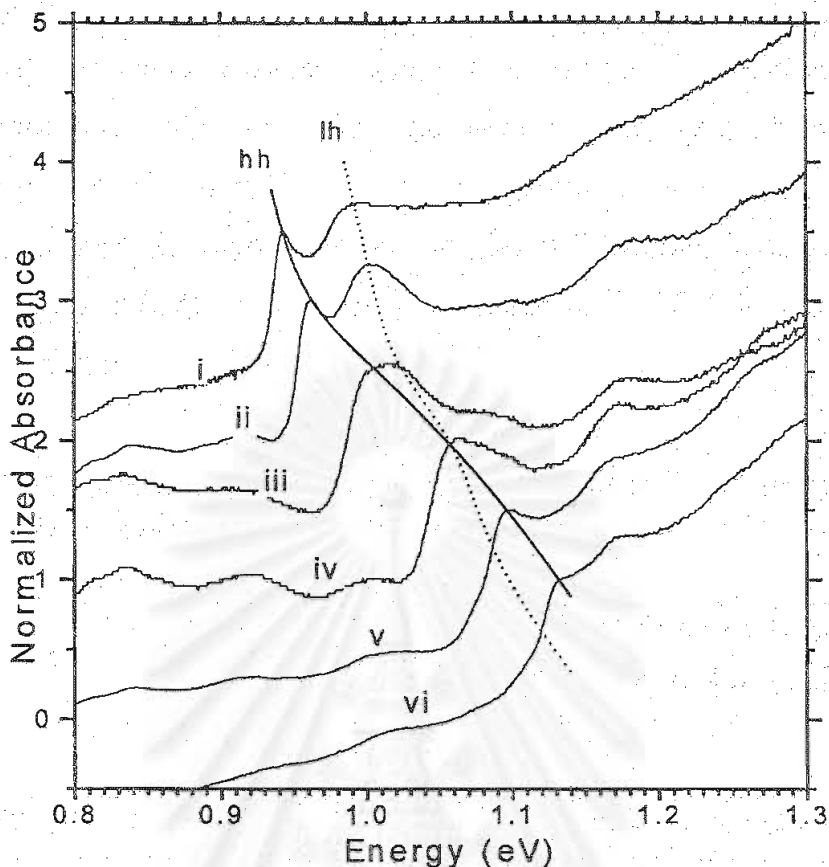


Fig 4.14 Normalized absorbance spectra of growth-in-defect CBE99-064 sample annealed at different temperature for 30 sec. Each piece was annealed (ii) at 625 C, (iii) at 650 C, (iv) at 675 C, (v) at 700 C, (vi) at 725 C, and (vii) at 750 C but (i) non-intermixed piece.

It must be admitted that guide eye for first hh- and lh- transition for all above sample is hard to indicate the exact first hh- and lh- transition when rapid thermal annealed temperature is increased. So error bar shown in the following section tells us how much accumulated error has been.

IV.1.3 Simulation data and point to find K value.

Error function model – detail in section II.5.2 - has been using to simulate hh-lh splitting and hh transition energy shift - the energy difference of first hh-transition between non-intermixed and intermixed sample. Error function model is based on two hypotheses. First hypothesis is that self-species atoms are exchanged. For example group-III species in the QW will exchange

with group-III species in the barrier. Second hypothesis is that exchange process will occurred between approaching atoms. Simulation software together with result from PL, TEM and x-ray measurement of each sample have been used to fit the base value of compositional Ga and QW width. We found that the best-fit value for those samples is illustrated in table 4.2. This result told us that slightly tensile strain was introduced to QW after intermixing process was performs.

Table 4.2 The best fitting value of composition Ga and QW width by using error function model compare to the ideal one.

Sample	Ideal Value			Best-fit value from error function model		
	%Ga	L _{QW}	strain	%Ga	L _{QW}	strain
CBE99-172	0.47	50	0.0	0.52	55.56	0.36
CBE99-064	0.47	50	0.0	0.51	50	0.30
CBE00-120	0.545	50	0.5	0.545	55.74	0.50

From figure 4.15 to figure 4.17, solid line represents simulation data plotted hh-lh splitting as function of hh-transition energy shift by varying k value - a ratio of the group-V to group-III diffusion lengths. Closed circles represent experimental data by using absorption measurement (previous section). Generally how far group-III and group-V species atom can move described by k value. If k is not equal to one, local strain develops as illustrated in section II.5.2. In figure 4.15, k value tends toward to infinity is best description for implanted CBE99-172 QW samples. This result means the movement of group-V atoms is dominant although the value of lh-hh splitting is quite far from the simulation data at the higher hh energy shift. The explanation is that the defects are introduced to QW layer when hh energy shift to higher.

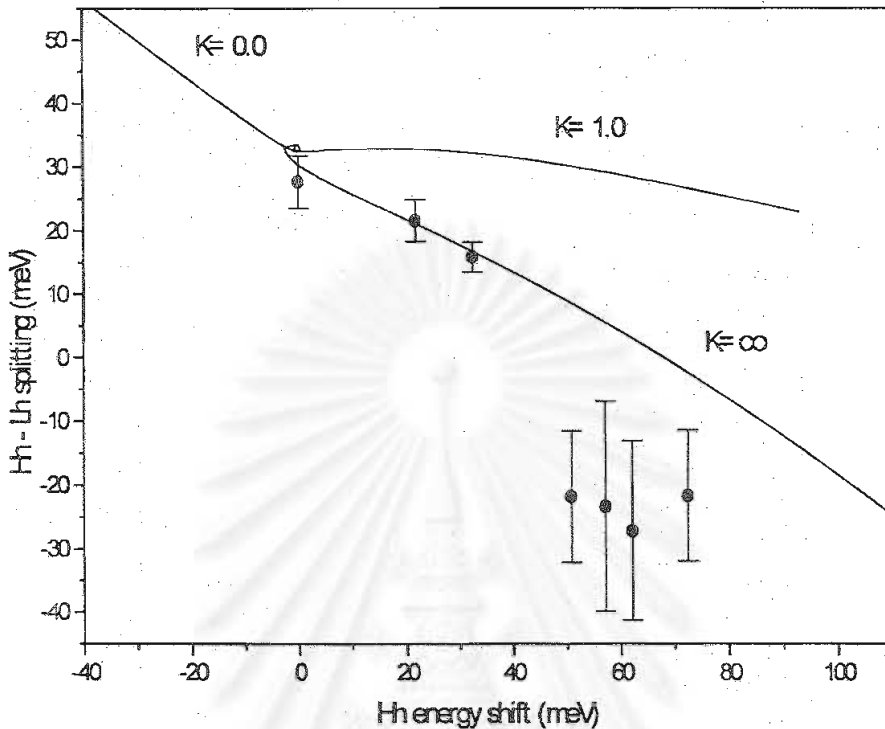


Fig 4.15 Hh-lh splitting plotted as a function of hh energy shift for CBE99-172 QW samples created defects by implantation technique. Closed circles represent to experimental data from absorption measurement and solid line represent simulation data by varying k value.

In figure 4.16, k is between 2 and 4 is best fit value for CBE99-064 sample. Explanation may occur that the tensile strain development at the center of the QW is strong enough and off-zone center contributions to the transition may need to be considered. It is also feasible that the k may represent a combination of intermixing due to non-equilibrium defects as well as a (smaller) contribution due to equilibrium generation of defects since for RTA temperatures of 725 C or more (refer to absorption data in the previous section).

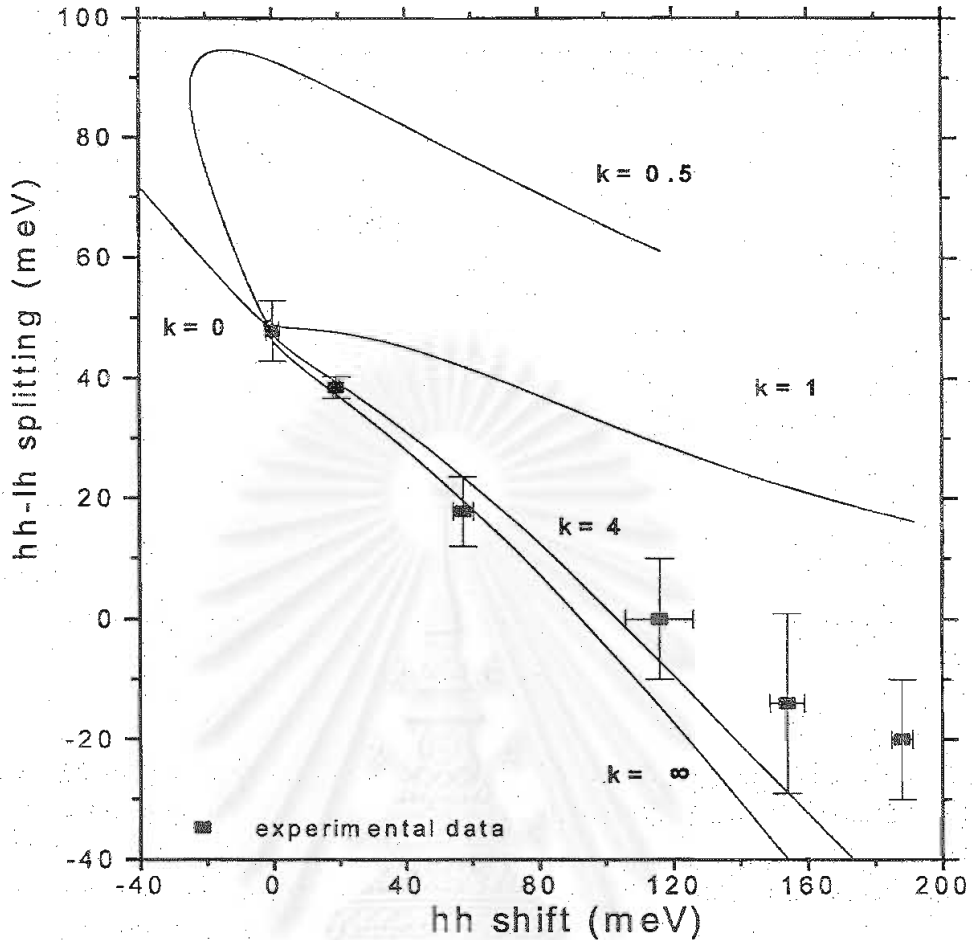


Fig 4.16 Hh-lh splitting plotted as a function of hh energy shift for CBE99064 QW samples created defected by growth-in-defect QWI technique. Closed circles represent to experimental data from absorption measurement and solid line represent simulation data by varying k value.

In figure 4.17, the best k value described for tensile CBE00-120 samples is between 4 and infinity. It seems that the movement of group-V atoms is dominant than that of group-III atoms. The explanation may be that strain arising out of lattice constant mismatch may cause interesting changes in physical properties through deformation potential effect. Strain changes the bandgap of the constituent materials and remove the degeneracy of heavy- and light-hole valence band at $\vec{k} = 0$. This illustrated in section II.5.2.

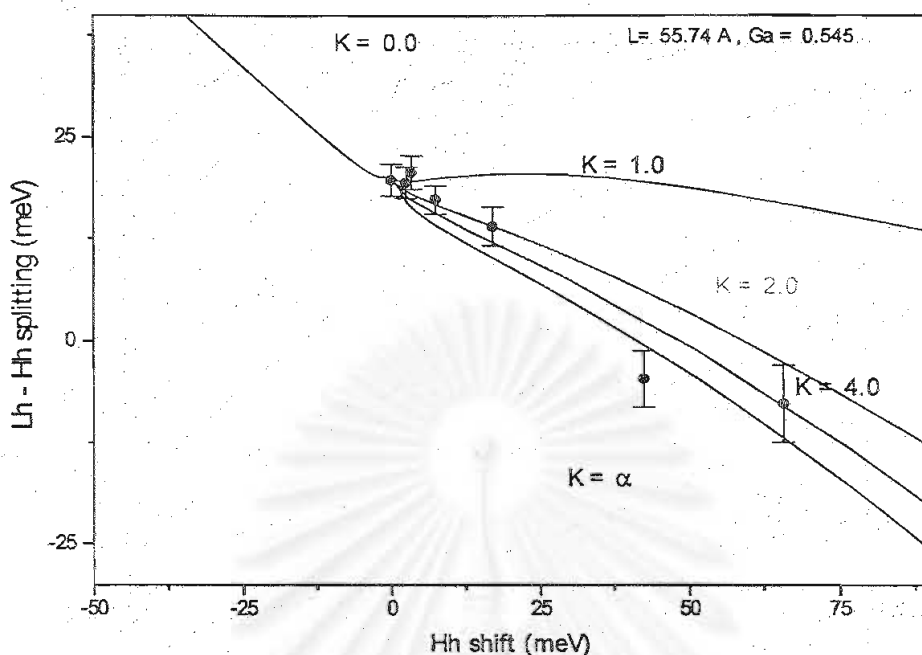


Fig 4.17 Hh-lh splitting plotted as a function of hh energy shift for CBE00120 tensile QW samples created defected by growth-in-defect QWI technique. Closed circles represent to experimental data from absorption measurement and solid line represent simulation data by varying k value.

As above results, k value in between 4 and tend to infinity seems to be similar so the diffusion of group-III and group-V species atoms proceed in the same way for those three samples created defects by two techniques: growth-in-defect QWI and implantation QWI technique. The results from those three sample said that the movement of group-V atoms in InGaAs/InP QW samples was dominant. To give a clear picture of interdiffusion of group-III and group-V atoms, phase space graph is shown in fig 4.18. The vertical and horizontal axis represent the varying composition of group-V atoms and that of group-III atoms, respectively. Binary compound present at the corner of the graph: InP, InAs, GaAs and GaP. Ternary and quaternary compounds represent at the edge line of and inside graph, respectively. Red dash line represents lattice-match strain compound. Above red dash line (green dash line) represent samples with

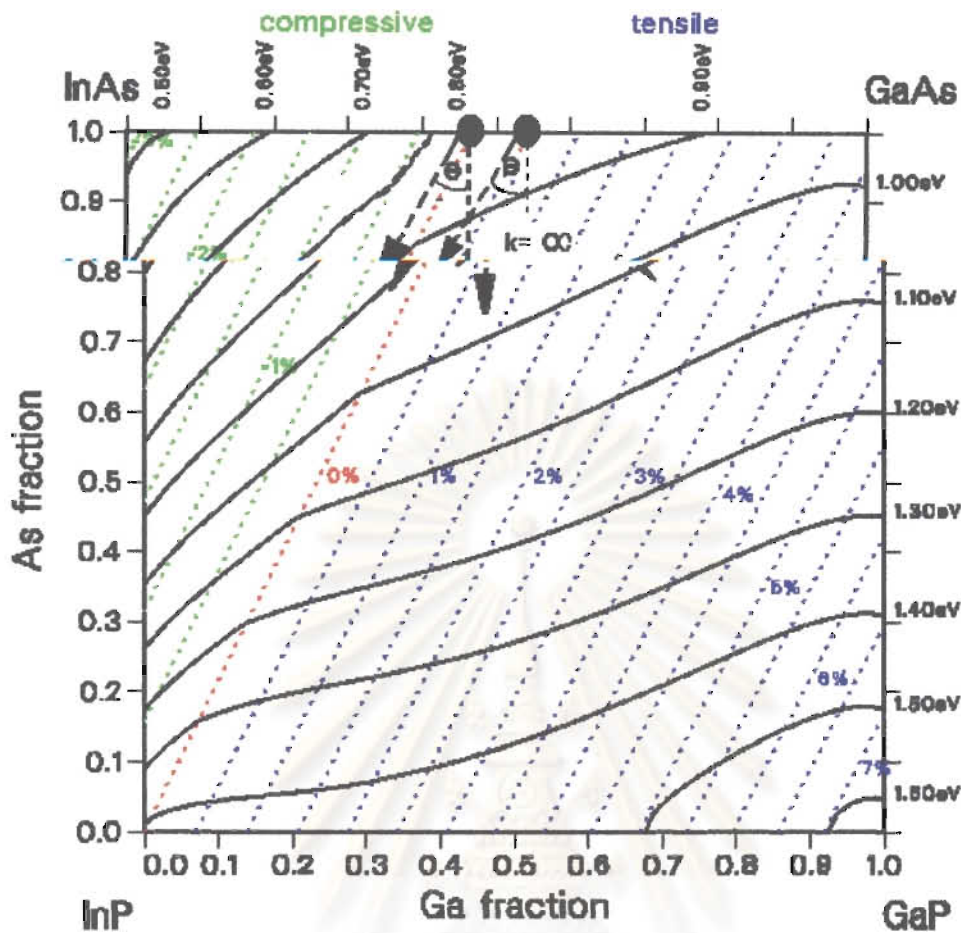


Fig 4.18. Phase space of $\text{In}_x\text{Ga}_{1-x}\text{As}_y\text{P}_{1-y}$ gaps at 4 K shown the relation of interdiffusion of group-III and group-V atoms.

compressive strain but the below one present sample with tensile strain. Solid line inside the graph represents energygap of samples measured at 4.2 K. Our three samples are represented by closed circle at the top horizontal edge line. For implanted sample, k tends toward infinity so the movement of group-V atoms is dominant. This is illustrated as the dot line with arrow in the vertical axis. As seen in the graph, the direction of arrow indicates that tensile strain is introduced into QW layer. For growth-in-defect sample, k equals to 4 that indicate by dash line with arrow in diagonal direction. So compressive strain seems to introduce. This fulfills one of our goals. It is also important to evaluate the quality of the layers in photonic devices. Thus time-resolved photoluminescence is performed to investigate residual damage and evaluate the optical quality of the layer before and after intermixing.

IV.2 TRPL used as a tool to investigate QW damage.

TRPL is also important for the design and fabrication of optoelectronic devices such as LED's, laser diodes, and modulator. Furthermore, the usability of intermixing for photonic integrated circuits (PICs) depends on the amount of damage introduced in QW by interdiffusion process and this topic become a popular subject in last five years. Carrier lifetime is one of parameters to determine the device performance. Generally residual damage of intermixed sample depends on the magnitude of the obtained energy shift. Piva and co-workers [79] have developed a method to characterize residual damage by using time resolved photoluminescence technique. This demonstration was done for samples of GaAs/AlGaAs emitting at ~ 0.8 microns. In this section, the possibility of extending this technique to $\text{In}_x\text{Ga}_{1-x}\text{As}_y\text{P}_{1-y}/\text{InP}$ layers emitting at 1.5 microns is investigated, with the objective to extract information on residual damage. To the best of our knowledge, no such investigations have been performed by time-resolved photoluminescence for intermixed $\text{In}_x\text{Ga}_{1-x}\text{As}_y\text{P}_{1-y}$ based on InP heterostructures. The first problem we need to address is the need to develop a time-resolved photoluminescence tool for this investigation. Indeed, it is difficult to find a sensitive detector at 1.5 microns with good time resolution, better than one nanosecond. This will be discussed in the next section.

So this section will focus on (i) provision of better TRPL system to monitor decay time in the region of 1.3 – 1.6 microns, and (ii) better understanding of the $\text{In}_{1-x}\text{Ga}_x\text{As}$ based on InP MQW material from investigation of carrier lifetimes in the intermixed QWs. These measurements will be performed on a series of samples with excess defects created by shallow ion implantation and grown-in-defect in the cladding layer.

While recombination dynamics in lattice-matched InGaAs/InP quantum wells has been subject to extensive investigations both experimental and theoretical, only little is known about the recombination dynamics in $\text{In}_{1-x}\text{Ga}_x\text{As}_y\text{P}_{1-y}/\text{InP}$ QW structures. Other authors have performed lifetime

measurements in InGaAs/InP QW structures on a different physical phenomenon. For example, U. Cebulla, G. Bacher and *et.al.* [80] have investigated the lifetime of InGaAs/InP QW as a function of QW width in range from 1 nm to 5 nm. They obtained that the thinner well width, the longer lifetime (~ 1 ns) is introduced. It was evidence that a reduced transition probability caused the penetration of the envelope wave function of the electrons into the barrier material was occurred. Furthermore, Hoffmann and co-workers [81] demonstrated that the narrower the well thickness, the longer excitonic recombination lifetimes is. These effects are influenced by the changes in band offsets as well as in the effective mass. Feldmann and his co-workers [82] also revealed that the lifetime decreased with decreasing well width due to the enhanced excitonic binding energy. Reducing the well width even further results in a smaller overlap integral of the electron and hole envelope wave functions in conduction and valence band. For electrons penetrate stronger into the barriers than the holes, which remain localized predominantly within the well. The higher the Ga composition, the shallower the potential well for electrons is become. Thus it is effect to increase the amplitude of the electron wave function in the barriers. At the same time, the holes remain localized in their virtually unchanged well, which leads to a reduction of the wave function overlap and give rise to longer recombination lifetimes.

According to different examples found in the literature, lifetime measurements can be used to probe many different physical phenomena: lh-hh state, exciton and LO-phonon scattering effect [83] [84], electron-hole overlap, carrier dynamic [85] [86] [87], orientation of crystal growth [88], interface state and non-radiative defects.

After a brief summary of the presented knowledge and a motivation from Piva's work, we will discuss about temporal resolution of our system at national research council of Canada in the following section. Then result of two series samples will describe later.

IV.2.1 System response

With the time-resolved photoluminescence system described in the previous chapter, temporal resolution of our system response at NRC is detected by single-photon-counting mode. Pulse-laser signal represents at the above corner of graph in fig 4.19. Ideally shape of pulse laser is similar to delta function. The decay side of the spectra at longer time (on the right) is fitted by a single exponential decay to extract the temporal resolution limit of the system. We obtain a decay constant of 270 ps, much longer than the 2 ps of the laser pulse thus indicating the laser pulse can indeed be considered like an infinitely short event compared to the system resolution. This resolution for characterizing the PL decay of InGaAs/InP QW heterostructures, which generally have lifetime of 300 ps or longer [88].

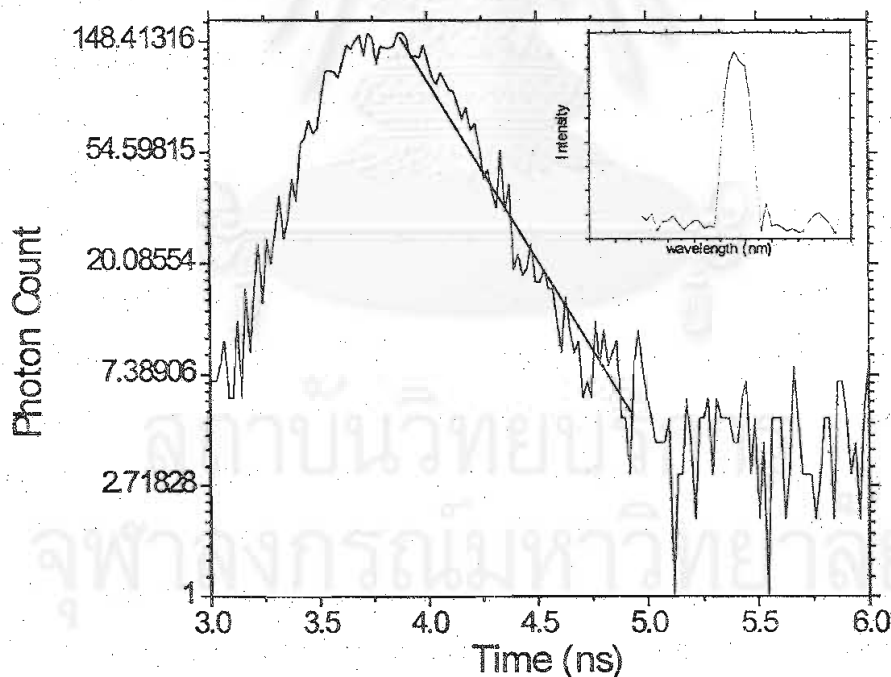


Fig 4.19 Typical instrumental response from 6.36 nm FWHM input laser pulse at a wavelength of 728.5 nm as shown at the above corner. Temporal resolution is ~ 270 ps.

IV.2.2 Lifetime of $\text{In}_x\text{Ga}_{1-x}\text{As}/\text{InP}$ heterostructures.

Time-resolved photoluminescence have been performed on two $\text{In}_{0.53}\text{Ga}_{0.47}\text{As}/\text{InP}$ multiple-quantum well structure introduced excess defects with two techniques: implantation QWI technique and growth-in-defect QWI technique. First series introduced excess defects by implantation QWI technique was CBE99-172 sample. Second series induced excess defects by growth-in-defect QWI technique was CBE99-064. For the first series, our identification in section IV.1 said that lower energy peak is emitted from active QW layer. So TRPL measurement was performed at 4.2 K with pulse laser at repetition rate of 4 MHz to obtain lifetime. Some TRPL trails of CBE99-172 sample implanted at different dose in range of 6×10^{11} ions/cm² and 1×10^{14} ions/cm² as shown in figure 4.20. In order to investigate summary of the lifetime, traces in figure 4.21 deduced from the traces shown in figure 4.20 are plotted. For doses below 10^3 cm⁻², the lifetime is constant at ~9 ns. At slightly high implantation doses, a reduction in the lifetime is observed. Finally lifetime becomes stable at shorter lifetime (~ 1.5 ns) for implanted doses above 5×10^{13} cm⁻². However, with this peak assignment, the long lifetimes observed for the as-grown sample are not consistent with results published in the literature. According to Cebulla and his co-workers work [89], for an InGaAs/InP QW similar to CBE 99172 sample, one would expect a lifetime in the range of 1 ns, which is significantly shorter than what is observed here. However, the published results were concerned with samples grown by MOCVD while the samples for this study were grown by CBE. Also it was recently shown that many of the QW layers grown by CBE do not have sharp interfaces (see more detail in section II.5.8.3). During the growth, thin (~3 monolayer) interfaces of InAsP form on either side of the InGaAs QW. The exact composition of this thin layer is difficult to determine, however it is possible that these layers cause a type-II band alignment, or that they cause the valence band maximum to occur at $k \neq 0$. Both cases would cause the lifetimes to become dramatically longer. As the samples are interdiffused, the ternary

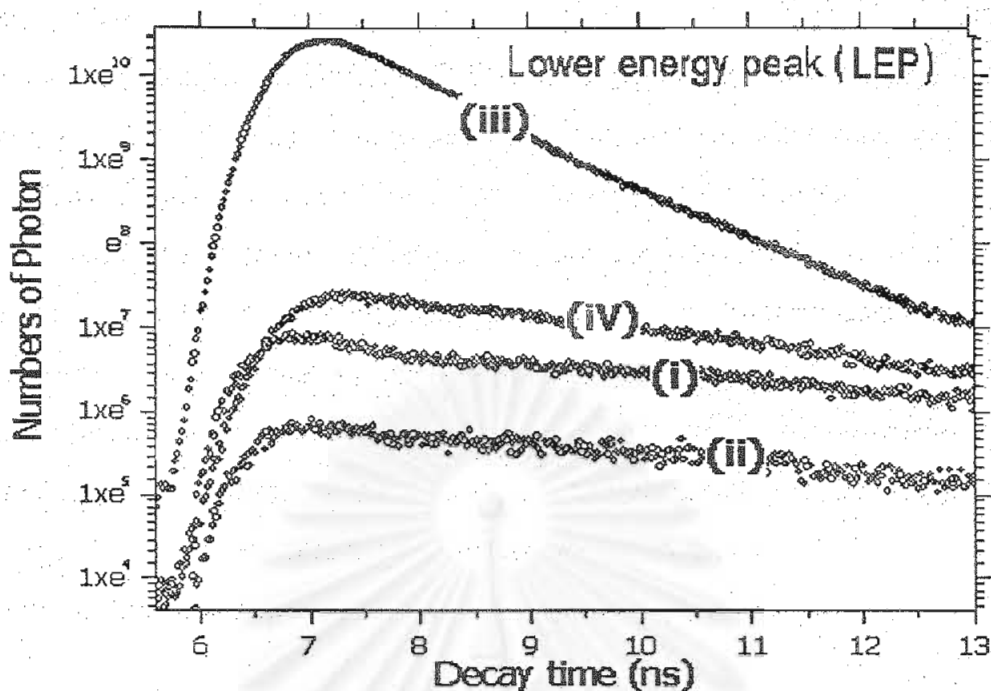


Fig 4.20 TRPL measurement performed at 4.2 K with pulse laser at repetition rate of 4 MHz on implanted sample (CBE99172) by varying implanted doses: (i) implanted dose at 6×10^{11} ions/cm² (at 1298 nm), (ii) implanted dose at 5×10^{12} ions/cm² (at 1286 nm), (iii) implanted dose at 5×10^{13} ions/cm² (at 1288 nm), and (iv) implanted dose at 1×10^{14} ions/cm² (at 1229 nm)

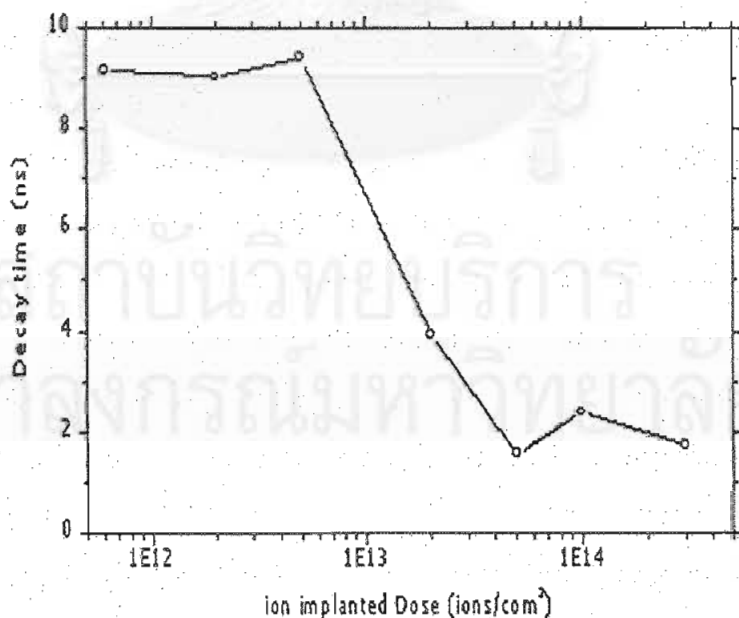


Fig 4.21 Decay time of CBE99172 samples (from fig 4.20) by varying ion implanted dose from 6×10^{11} ions/cm² to 1×10^{14} ions/cm²

interface layers will be washed out and the effect it has on the band structure vanishes. A standard InGaAsP/InP QW is recovered and the lifetime becomes closer to the other values reported in the literature. This may explain the decrease in lifetime observed for doses of $5 \times 10^{13} \text{ cm}^{-2}$ and higher.

Another possible explanation involves the introduction of non-radiative centers during the intermixing process. Indeed, as the implant dose is increased more defects are created in the sample and one might expect that a higher concentration of non-radiative centers may be present in the sample even after annealing. According to the theory presented in chapter 2, the measured lifetime can be expressed in terms of a radiative and non-radiative recombination lifetime as follows:

$$\frac{1}{\tau_{\text{measured}}} = \frac{1}{\tau_{\text{rad}}} + \frac{1}{\tau_{\text{nonrad}}}$$

In general one can expect that the non-radiative recombination lifetime will become shorter as the concentration of non-radiative defects increases. Thus, the measured lifetime can become shorter as the amount of interdiffusion (i.e. implantation dose) increases. However, in this case one would expect the lifetime to decrease gradually with increasing implantation dose, which is not what is observed in figure. 4.21.

TRPL also performed at 4.2 K to growth-in-defect CBE99-064 samples to observe decay time plotted as a function of energy shift is shown in fig 4.22. It can be seen that decay time is become longer when the energy shift increases. This measurement was obtained at 5K under non-resonant excitation conditions, which excitation wavelength is 710 nm. In the as-grown sample, the lifetime is quite short (~2 ns) and this value is comparable to results obtained by other groups [89] for nominally similar structures. At lower interdiffusion lengths (Shifts < 50 meV), the decay time increases slowly. This does not suggest any degradation of the optical quality in the structure since the introduction of residual damage (i.e. increasing density of non-radiative centers) would cause a decrease of the measured lifetime. W. Pickin and J. P.

R. David work [90] explained effect of non-radiative centers were introduced associated with the well-barrier interface for GaAs QW. Their demonstration was described the recombination rate was become significantly higher if the coupling between the carrier wave functions and the interface states in quantum confined structures is greater than that in bulk material. Their work encourage explanation. At higher interdiffusion lengths (PL shift 100-120 meV), the lifetime suddenly increases to 25 ns. This sudden increase is correlated with the point at which the hh and lh transitions become degenerate, as can be seen from the transmission measurements (fig. 4.14). This crossing of lh and hh states causes the valence band maximum to be at $k \neq 0$. The PL transition therefore becomes an indirect transition, which has a considerably longer lifetime than the direct transition. Note that in this sample, only one PL peak could be observed, so any discussion in terms of interface layers is ignored.

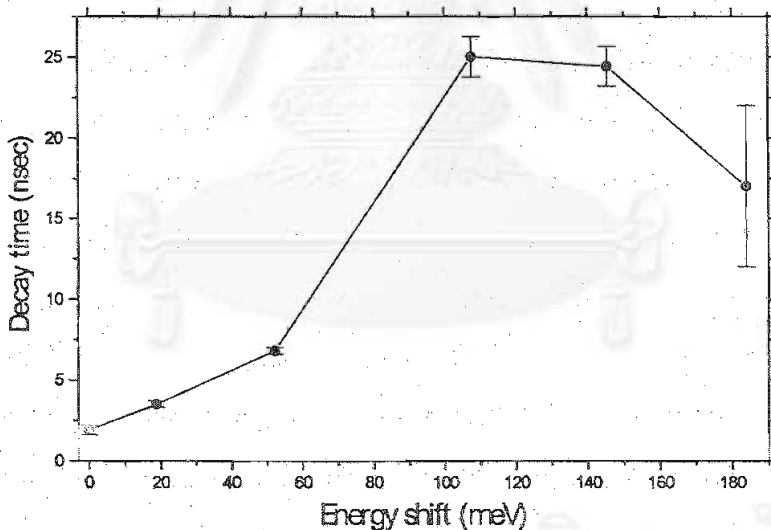


Fig 4.22 Decay time of low-temperature grown sample (CBE99064) plotted as a function of energy shift measured by PL technique.

IV.2.3 Lifetime Vs temperature

Generally, carriers do not diffuse far enough to reach the defects at low temperature (~ 4.2 K). Until then temperature is increased, diffusion rate of the

carriers is introduced and the probability of hitting a non-radiative defect is higher. So performing TRPL as a function of temperature may give us some information relative to the presence of non-radiative centers in our samples. Temperature dependent TRPL was operated on non-intermixed sample (CBE99172), intermixed sample implanted at 2×10^{12} ions/cm² and 5×10^{13} ions/cm². According to work done by Piva and co-workers [79], they performed temperature dependent TRPL on implanted GaAs/AlGaAs heterostructure found that *intermixed and non-intermixed wells possess similar recombination rates at low temperatures. Lifetime begins to increase with rising temperature for non-intermixed sample but decreases with rising temperature for higher implanted dose.* His explanation for this is that the formation of an increasing number of non-radiative recombination sites in the intermixed QW structures resulting from the ion bombardment. By increasing the density of defects through implantation, the average separation between non-radiative recombination sites surviving the RTA is reduced. If the average free excitons displacement before recombination is significantly smaller than average separation between non-radiative recombination sites at low temperature, fewer encounters with non-radiative centers result. In this way, it is expected that the lifetime at low temperature will be unaffected by the intermixing process. At higher temperature, free excitons diffusivities increase, and a greater number of non-radiative defects may be encountered thus reducing the carrier lifetimes. Figure 4.23 shows temperature dependent TRPL on non-intermixed CBE99-172 samples. Opened (closed) circle is from lower energy peak (higher energy peak) at 4.2 K (see figure 4.8). When temperature is raised, those lower and higher energy peak merge to a peak as shown in figure 4.24. Decay time is slightly stable in range 20 K to 100 K and then gradually falls down to shorter lifetime at 170 K. At temperature above 170 K, lifetime become stable at ~ 6 ns. This may means the QW behaves as if there were non-radiative centers. To confirm this result, log PL intensity vs temperature is performed as shown in figure 4.25. In range 4.2 K to 10 K, intensity in figure 4.26 is constant while lifetime in figure 4.24 is slightly

stable. Actually, the lifetime is supposed to increase with temperature in a pure semiconductor as non-intermixed sample [91]. Only radiative recombination time is considered at low temperature, however, non-radiative time is take into account if the temperature is introduced. It may probably be explained our result for non-intermixed sample that either interface between QW and barrier or QW and barrier material is not perfectly pure. .

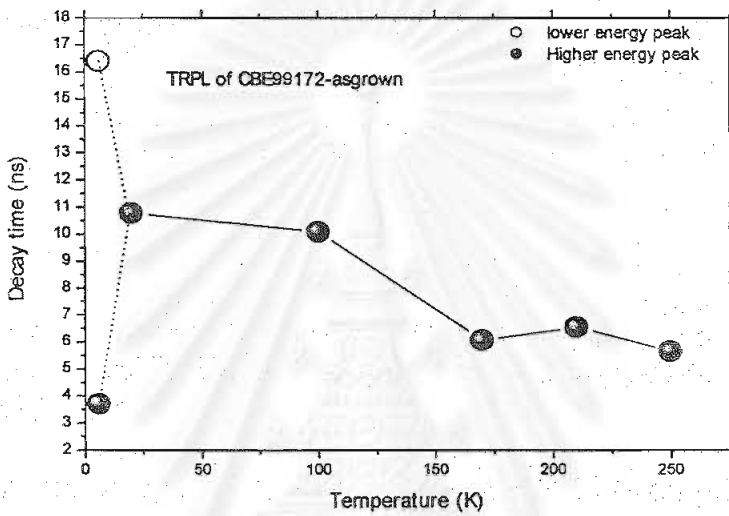


Fig 4.23 Temperature dependence TRPL on non-intermixed CBE99-172 sample (RTA at 700 C for 150-sec-total-time) by using 710-nm pulse laser. Dot and solid line are for guide-eye.

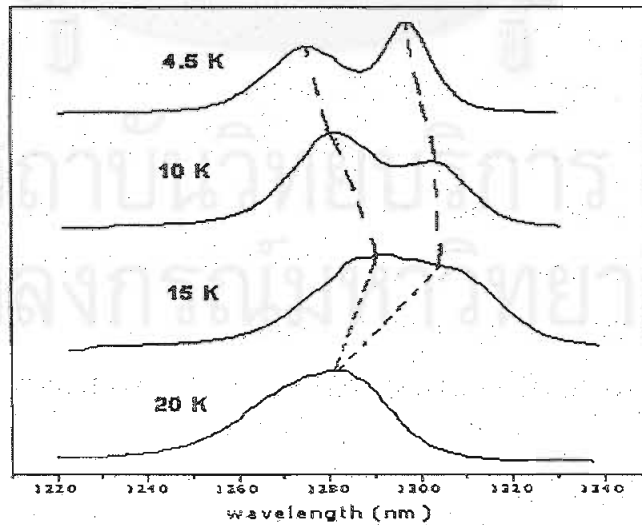


Fig 4.24 Intensity PL by varying temperature for non-intermixed CBE99-172 samples by using 710-nm pulse laser. Dot line is guide-eye for merged of lower and higher energy peak by varying temperature.

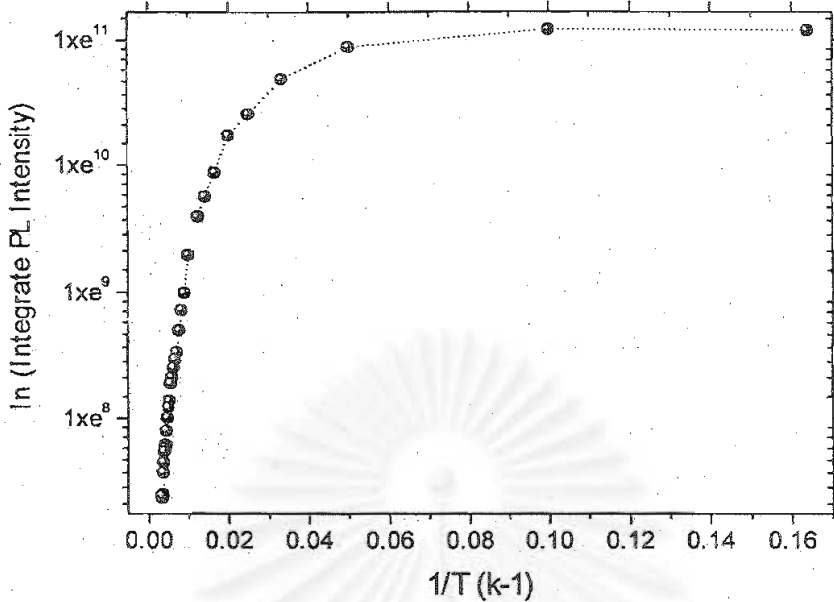


Fig 4.25 Log integrated intensity PL vs temperature dependence for non-intermixed CBE99-172 samples by using 980-nm laser diode at 1.89 mW.

Similar technique is applied to intermixed CBE99-172 samples implanted at 2×10^{12} ions/cm² to investigate lifetime as a function of temperature as shown in figure 4.26. Decay time is sharply decreasing with increasing temperature to 80 K and then decay time is more stable (~ 2 ns) until temperature reach 300 K. Note that those lower and higher energy peak merge together at 80 °C. According to figure 4.27, log integrated PL intensity plotted as a function of inverse temperature shows that integrated PL intensity is stable when temperature is in range 4.2 to 10 K. This may explain as resulting from the temperature dependent distribution of kinetic energy among excitons in the QW. As only free excitons near the Brilluin-zone center can recombine, increased lattice temperatures decrease the protion of them which may readily recombine.

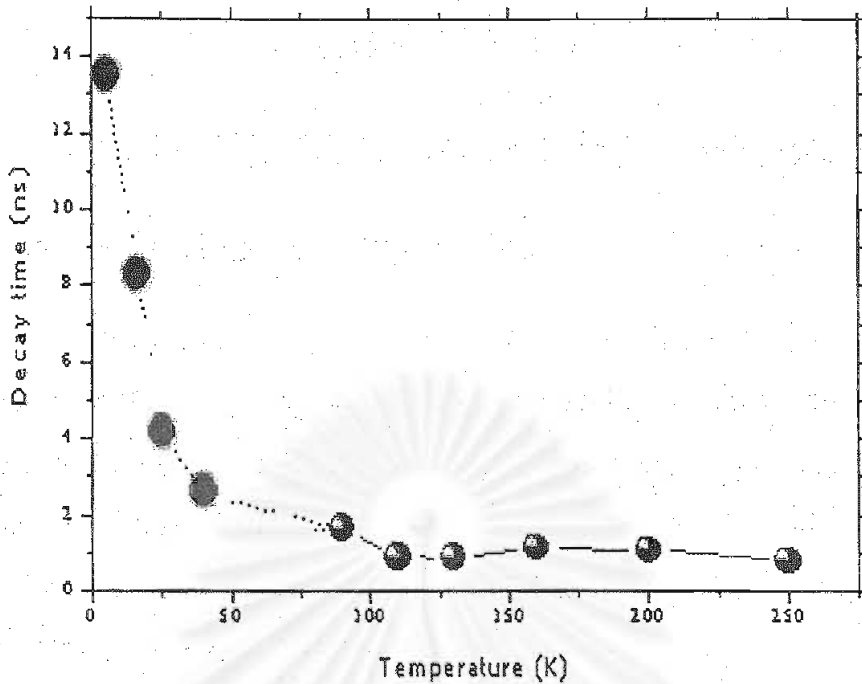


Fig 4.26 Temperature dependent TRPL of intermixed CBE99-172 sample implanted at 2×10^{12} ions/cm² (RTA at 700 C for 150-sec-total-time) by 710-nm CW laser. Dot and solid line are for guide-eye.

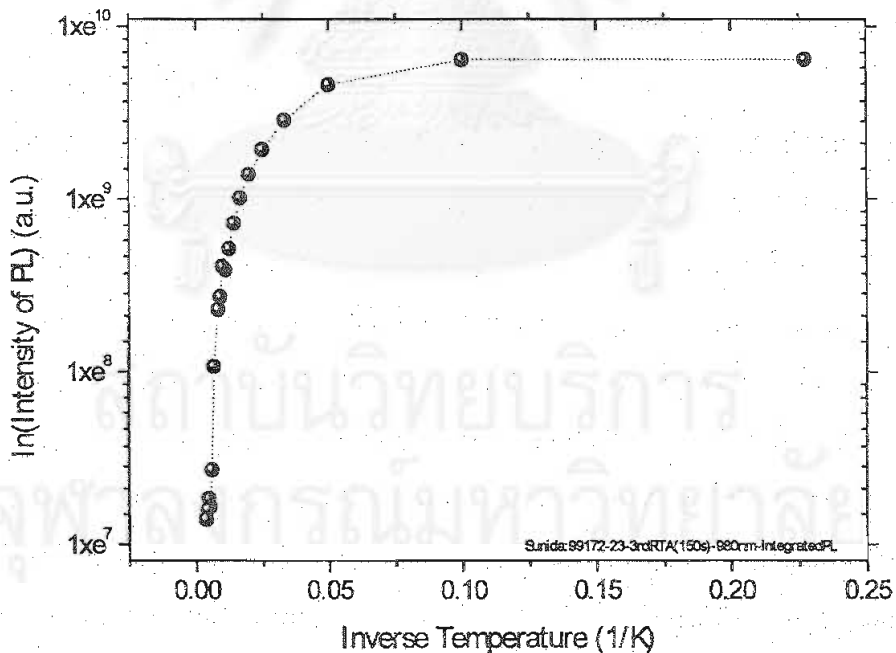


Fig 4.27 Log integrated intensity PL vs temperature dependence for intermixed CBE99-172 sample implanted at 2×10^{12} ions/cm² (RTA at 700 C for 150-sec-total-time) by using 980-nm laser diode at 1.89 mW. Dot line is for guide-eye.

CHAPTER V

SUMMARIZATION & FUTURE WORK

V.1 Summarization and Suggestion.

We found that slightly tensile strain is introduced to all wafers after intermixing process is applied, which correspond to observed coefficient interdiffusion rate (k). If k value is greater than 1, the center and the edge of the QW were respectively become introduction of tensile and compressive strain. It is clear that interdiffusion process is dominated by the motion of the group-V atom in InGaAs based on InP QWs.

The results from both absorption measurement and time-resolved photoluminescence technique were agreed together that either non-equilibrium defects or equilibrium generation of defect is represented in the intermixed low-temperature grown samples. However, temperature dependent time-resolved photoluminescence is also needed to operate on to obtain the presence of non-radiative defects in the material.

For implanted sample bombard by varying implanted dose, we found that results from absorption measurement and time-resolved photoluminescence technique at low temperature (~ 4.2 K) tell us a possibility of non-radiative center is introduced with increasing implanted dose. However temperature dependent dose on non-intermixed and some intermixed implanted samples seem to disagree with our hypothesis observed from time-resolved photoluminescence and absorption technique at low temperature (~ 4.2 K). Decay time for non-intermixed and lower intermixed sample is decreasing with rising temperature but increasing with rising temperature for the higher implanted dose. The reasons is explained for this,

1. no non-radiative center is presented at higher implanted dose due to light- and heavy-hole overlap.
2. Lifetime in non-intermixed sample is often longer than that reported in literature. This indicates that the sample is perhaps not what we

thought it was and we may have to work on the reproducibility of the growth process. In particular, it may be that sharper interfaces are needed (evidence of 2-3 mono-layer of compound material).

V.2 Future work

Temperature dependent TRPL was also needed to utilize on low-temperature grown samples because carriers generally do not diffuse far enough to reach the defects at low temperature (~ 4.2 K). Until then temperature is increased, diffusion rate of the carriers is introduced and the probability of hitting a non-radiative defect is higher. However, The duration time is limited time and we need to concentrate on understanding the result of TRPL performed at 4.2 K on both samples that we have right now before we can go to a more complicated step. Furthermore, we can extend our work to TRPL on quaternary $\text{In}_x\text{Ga}_{1-x}\text{As}_y\text{P}_{1-y}/\text{InP}$.

Reference

- [1] J.J. He, S. Charbonneau, P.J. Poole, G.C. Aers, Y. Feng, and E.S. Koteles. Polarization insensitive InGaAs/InGaAsP/InP amplifiers using quantum well intermixing. Appl. Phys. Lett. **69**(1996): 562-564.
- [2] E. Kapon, N.G. Stoffel, E.A. Dobisz and R. Bhat. Appl. Phys. Lett. **52** (1988): 351-353.
- [3] T. Wolf, C-L Shieh, R. Engelmann, K. Alavi and J. Mattz. Appl. Phys. Lett. **55**(1989):1412-1414.
- [4] N. Jr. Holonyak, W.D. Laidig, M. D. Camras, J. J. Coleman and P.D. Dapkus. Appl. Phys. Lett. **39**(1981):102-104.
- [5] W.D. Laidig, J.W. Lee and P.J. Caldwell. Appl. Phys. Lett. **45**(1984):485-487.
- [6] John H. March. Quantum well intermixing. Semicond. Sci. Technol. **8** (1993): 1136-1155.
- [7] T. Miyazawa, H. Iwamura, and M. Naganuma. Integrated External-Cavity InGaAs/InP lasers Using Cap-Annealing Disordering. IEEE Photon. Technol. Lett. **3**(1991): 421-423.
- [8] S. Si, S. Kim, J. Lee and *et al.* A Large Bandgap Shift in InGaAs(P)/InP Multi-Quantum Well Structure Obtained by Impurity-Free Vacancy Diffusion Using SiO₂ Capping and Its Application to Photodetectors SPIE. **3287**(1998): 88-95.
- [9] C. Francis, F.H. Julien and *et al.* Selective Band-gap Blueshifting of InGaAsP/InGaAs(P) quantum wells by thermal intermixing with phosphorus pressure and dielectric capping. J. Appl. Phys. **75** (1994): 3607-3610.
- [10] M. Katayama, Y. Tokuda, T.Y. Inoue, A. Usami, and T. Wada, Ga out-diffusion in rapid-thermal-processed GaAs with SiO₂ encapsulants. J. Appl. Phys. **69**(1991): 3541-3545.

- [11] R.C. Alferness, U. Koren, L.L. Buhl *et.al.* Broadly tunable InGaAsP/InP laser based on a vertical coupler filter with 57-nm tuning range. Appl. Phys. Lett. **60**(1992): 3209-3211.
- [12] M. Aoki, M. Suzuki, H. Sano, T. Kawano, T. Ido, T. taniwatari, K. Uomi, and A. Takni. InGaAs/InGaAsP MQW electroabsorption modulator integrated with a DFB laser fabricated by band-gap energy control selective-area MOCVD. IEEE. J. Quantum Electron. **29**(1993): 2088-2096.
- [13] A. R. Pratt and R. L. Williams *et.al.*, Indium migration control on patterned substrates for optoelectronic device applications. Appl. Phys. Lett. **65**(1994): 1009-1011.
- [14] J.J. Dubowski, S. Charbonneau, A.P. Roth *et al.* A Comparative study of laser- and Ion Implantation-induced quantum well intermixing in GaInAsP/InP microstructure. SPIE. **2991**(1997): 113-118.
- [15] B.A. Lengyel. Introduction to Laser Physics. New York, United States of America: John Wiley and Sons, Inc. 1966.
- [16] Sheng S. Li. Semiconductor Physical Electronics. New York, United States of America: Plenum Press. 1993.
- [17] Tom Wenckebach. Essentials of Semiconductor Physics. Singapore: John Wiley and sons. 1999.
- [18] Pallab Bhattacharya. Semiconductor Optoelectronic Devices. United States of America: Prentice-Hall. 1994.
- [19] W. Crawford Dunlap. An Introduction to semiconductors. United States of America: John Wiley and Sons. 1957.
- [20] Donald A. Neamen. Semiconductor Physics and devices. United State of America: Richard D. Irwin. 1992.
- [21] Robert F. Pierret. Semiconductor Device Fundamentals. United states of America: Addison-Wesley Publishing Company. 1996.
- [22] Jasprit Singh. Semiconductor Devices: An Introduction. International Editions (n.p.): McGraw-Hill. 1994.

- [23] H.V. Keer. Principles of the Solid State. First printed version. India: Wiley Eastern Limited and New Age International limited. 1993.
- [24] Brian Tuck. Atomic Diffusion in III-V Semiconductors. Bristol and Philadelphia: Adam Hilger. 1988.
- [25] P.K. Basu. Theory of Optical Process in Semiconductor Bulk and Microstructures. NY, USA: Oxford University Press. 1997.
- [26] J. Dabrowski. Point Assisted Diffusion in Semiconductor. Solid state Phenomena. 61(2000): 23-50.
- [27] C. Kittel. Introduction to Solid state Physics. 6th edition. Canada: John Wiley & Sons. 1986.
- [28] M.P.C.M. Krijn, Semicon. Sci. Technol. 6(1991): 27.
- [29] K. M. Mukai, M. Sugawara and S. Yamazaki. Interdiffusion process in lattice-matched $\text{In}_x\text{Ga}_{1-x}\text{As}_y\text{P}_{1-y}/\text{InP}$ and $\text{GaAs}/\text{Al}_x\text{Ga}_{1-x}\text{As}$ quantum wells. Phys. Rev. B. 50(1994): 2273-2282.
- [30] B. L. Weiss, Y. Chan and *et.al.* The electro-optic properties of interdiffused InGaAs/InP quantum well structures. J. Appl. Phys. 88(2000): 3418-3425.
- [31] T. Fujii, M. Sugawara, A. Yamazaki and K. Nakajima. Macroscopic Mechanism of Group V Interdiffusion in Undoped InGaAs/InP Quantum Wells Grown by MOVPE. J. Cryst. Growth. 105(1990): 348.
- [32] I. Harrison. Review Impurity-induced disordering in III-V multi-quantum wells and superlattices. Sci. Mats. In. Elec. 4(1993): 1-28.
- [33] H. Temkin, S.N.G. Chu, M.B. Panish and R.A. Logan. Thermal stability of InGaAs/InP Quantum Well Structures grown by gas source molecular beam epitaxy. Appl. Phys. Lett. 50(1987):956.
- [34] R.W. Glew, J.P. Stagg, P.D. Greene, A.T.R. Briggs, S. Bradshaw and J.H. Marsh, presented at 3rd International Conference on InP and Related Materials, Cardiff, 1991.

- [35] S. J. Yu, H. Asahi, S. Emura, S. Gonda and K. Nakashima. Raman Scattering study of thermal interdiffusion in InGaAs/InP superlattice structure. J. Appl. Phys. 70(1991): 204-208.
- [36] Sang-Wan Ryu, Byung-Doo choe and *et.al.* Determination of interdiffusion coefficients of cations and anions in InGaAs/InP superlattice. Appl. Phys. Lett. 71(1997): 1670-1672.
- [37] D.G. Deppe and N. Holonyak. Atom diffusion and impurity-induced layer disordering in quantum well III-V semiconductor heterostructures. J. Appl. Phys. 64(1988): R93-R113.
- [38] Wai-Chee Shiu, J. Micallef, and *et.al.* Effects of different cation and anion interdiffusion rates in disordered In_{0.53}Ga_{0.47}As/InP single quantum wells. Jpd. J. Appl. Phys. 34(1995): 1778-1783.
- [39] H. Chen, R. Feenstra and *et.al.* Enhanced group-V intermixing in InGaAs/InP quantum wells studied by cross-sectional scanning tunneling microscopy. Appl. Phys. Lett. 75(1999): 79-81
- [40] Gerald Bastard. Wave mechanics applied to semiconductor heterostructures. France. De physique. 1986.
- [41] Calvin Yi-Ping Chao and Shun Lien Chuang. Phys. Rev. B. 46 (1992): 4110.
- [42] W. Seifert, X. Liu, and L. Samuelson, Mat. Res. Soc. Symp. Proc. 281(1993):97.
- [43] Dieter K. Schrode, Semiconductor material and Device Characterization. Singapore: John Wiley and Son (n.d.).
- [44] G.W. Ewing, Instrumental Methods of Chemical Analysis. 5th Edition. (n.p.): McGraw-Hill Book Company. 1985.
- [45] R. G. Messerschmidt, M.A. Harthcock. Infrared Microspectroscopy Theory and applications. NY, USA: Marcel Dekker. 1988.
- [46] Peter R. Griffiths. Fourier Transform infrared spectrometer. NY, USA: Wiley. 1986.
- [47] Robert G. Messerschmidt and Mathew A. Hartheock. Infrared Microspectroscopy: theory and applications. NY, USA: K1988.

- [48] E. F. Schubert. Doping in III-V semiconductors. Cambridge. The press Syndicate of the University of Cambridge. 1993.
- [49] White, Robert. Chromatography/Fourier Transform Infrared Spectroscopy and its applications. NY, USA: Marcel Dekker. 1990.
- [50] Joseph W. Goodman. Introduction to Fourier Optics. San Francisco, USA: McGraw-Hill. C1968.
- [51] White, Robert. Chromatograph/Fourier Transform Infrared spectroscopy and its application. NY, USA: Marcel Dekker. 1990: 3-41.
- [52] R.J. Bell. Introductory Fourier Transform Spectroscopy. NY, USA: Academic press. 1972.
- [53] J. P. Bergmann, P.O. Hotz, and B. Monemar. Decay measurements of free- and bound-exciton recombination in doped GaAs/Al_xGa_{1-x}As quantum wells. Phys. Rev. B. 43(1991): 4765-4770.
- [54] M. Wegener, I. Bar-Joseph, and *et.al.* Femtosecond dynamics of excitonic absorption in the infrared In_xGa_{1-x}As quantum wells. Phys. Rev. B. 39(1989): 12794-12801.
- [55] B.K. Ridley. Kinetics of radiative recombination in quantum wells. Phys. Rev. B. 41(1990): 12190-12196.
- [56] P. Tronc. G. Wang and *et.al.* Time-resolved photoluminescence study of GaInAs/AlGaInAs superlattices. Superlattices and Microstructures. 24(1998): 347-352.
- [57] S. Zimmermann, L. Vina, H. Schweizer and *et.al.* Role of hole localization in the optical singularities of a tow-dimensional electron gas studied by time-resolved photoluminescence. Semicond. Sci. Technol. 12 (1997): 953-957.
- [58] Chris Van Hoof. Physics and application of resonant tunneling towards Novel optoelectronic devices. NY. USA: 1988.
- [59] Andrew Richard Pratt. Control of Indium Migration on Patterned substrates for Optoelectronic Device Application. Degree of Doctor

of Philosophy and Diploma of Imperial College. Physics department Science. University of London. 1995.

- [60] S. Raymond. Zero-Dimensional Properties of Self-Assembled Islands. Doctoral degree. Physics department. Science. University of Ottawa. 1997.
- [61] E.V. K. Rao, A. Hamoudi and *et.al.* New encapsulant source for III-V quantum well disordering. Appl. Phys. Lett. 66(1995):472-474.
- [62] A. Hamoudi, E.V. K. Rao and *et.al.* Controlled disordering of compressively strained InGaAsP multiple quantum wells under SiO:P encapsulant and application to laser-modulator integration. J. Appl. Phys. 78(1995):5638-5641.
- [63] W.P. Gillin, S.D. Perrin and K.P. Homewood. Comparative study of silicon nitride encapsulated and phosphine overpressure annealing on the interdiffusion of In_xGa_{1-x}As_yP_{1-y} heterostructure. J. Appl. Phys. 77(1995): 1463-1465.
- [64] N. Cao, B.B. Elenkrig and *et.al.* Band-gap blue shift by impurity-free vacancy diffusion in 1.5- μ m strained-InGaAsP/InP multiple quantum-well laser structure. Appl. Phys. Lett. 70(1997): 3419-3421.
- [65] S. J. Pearton, C.R. Abernathy, and F. Ren. Topics in growth and device processing of III-V semiconductor. Singapore: World Scientific Publishing. 1996.
- [66] J.F. Ziegler, J.P. Biersack and U. Littmark. The stopping and Range of Ions in Solids. Vol 1. NY, USA: Pergamon Press. 1985.
- [67] H. Ryssel and H. Glawischnig. Ion Implantation Technique: The Calculation of Ion Ranges in Solids with Analytic Solutions. Berlin: Springer-Verlag. 1982.
- [68] J.F. Ziegler and J.M. Manoyan. The stopping of ions in compounds. Nuclear Instruments and Methods. B35(1989): 215-228.

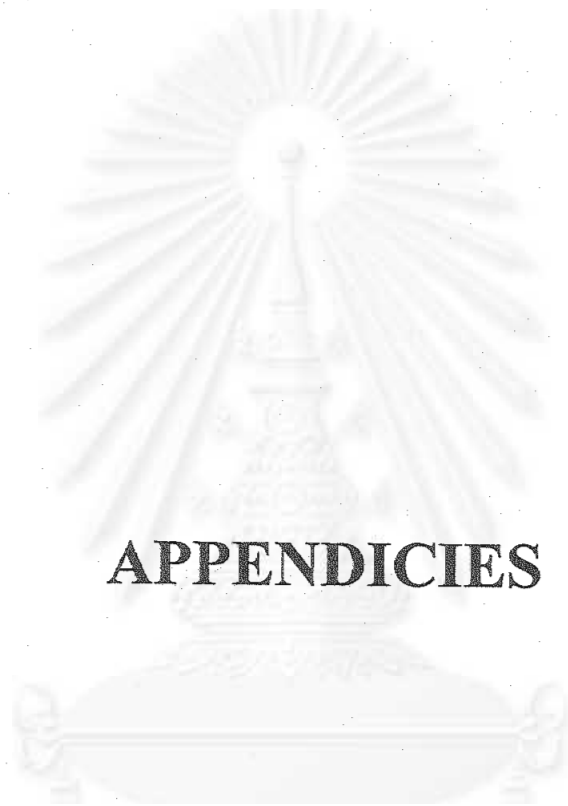
- [69] W.D. Laidig, N. Holonyak, M.D. Camras, K. Hess, J.J. Coleman, P.D. Dapkus, and J. Bardeen. Disorder of an AlAs-GaAs superlattice by impurity diffusion. Appl. Phys. Lett. **38**(1981):776.
- [70] S.R. Andrew, J.H. Marsh, M.C. Holland, and A.H. Kean. Quantum-Well Laser with Integrated Passive Waveguide Fabricated by Neutral Impurity Disorder. IEEE Photonics Technol. Lett. **4**(1992):426.
- [71] D. Kirillov, J. L. Merz, P.D. Dapkus, and J.J. Coleman, J. Appl. Phys. **55** (1984):1105.
- [72] D. G. Deppe, L. J. Guido, N. Holonyak, K. C. Hsieh, R. D. Burnham, R. L. Thornton, and T.L. Paoli. Stripe-geometry Quantum Well Heterostructure $\text{Al}_x\text{Ga}_{1-x}\text{As}$ -GaAs lasers defined by defect diffusion. Appl. Phys. Lett. **49**(1986): 510.
- [73] J.D. Ralston, S. O'Brien, G. W. Wicks, and L. F. Eastman, Appl. Phys. Lett. **52**(1988): 1151.
- [74] J. Z. Wan, D.A. Thompson and J. G. Simmons. Ion implantation induced compositional intermixing in the InGaAs/InP MQW system for wavelength shifted waveguides. Nuclear Instruments and Methods B. **106**(1995): 461-465.
- [75] C.K.W. Wyllie and D.A. Thompson. Compositional intermixing enhancement in InGaAs(P)/InP quantum well heterostructures related to lateral composition modulation. Semicond. Sci. Technol. **13**(1998): 750-755.
- [76] S.J. Pearton and A. Katz. High temperature rapid thermal annealing of InP and related materials. Mater. Sci. Eng. B **18**(1993): 153.
- [77] S.J. Pearton and R. Caruso. Rapid thermal annealing of GaAs in a graphite susceptor-comparison with proximity annealing. J. Appl. Phys. **66**(1989): 663.
- [78] S.J. Pearton. Ion beam processing and rapid thermal annealing of InP and related compounds. 2nd Int. Conf. On Indium Phosphide and Related materials: Denver, 1990, NY, USA : IEEE : 379.

- [79] P.G. Piva, S. Charbonneau and *et.al.* Effect of implantation dose on photoluminescence decay times in intermixed GaAs/AlGaAs Quantum wells. Appl. Phys. Lett. **68**(1996): 2252-2254.
- [80] U. Cebulla, G. Bacher, A. Forchel, and *et.al.* lifetimes in thin $\text{In}_x\text{Ga}_{1-x}\text{As}/\text{InP}$ Quantum wells. Phys. Rev. B. **39**(1989): 6257-6259.
- [81] A. Hoffmann, H. Siegle, and *et.al.* Recombination Dynamics in Strained $\text{In}_{1-x}\text{Ga}_x\text{As}/\text{InP}$ Quantum Well Structures. Superlattices and Microstructures. **15**(1994): 303-307.
- [82] Feldmann, G. Peter, E. O. Gobel and *et.al.* Linewidth dependence of radiative exciton lifetimes in quantum well. Phys. Rev. Lett. **59** (1987): 2337- 2340.
- [83] P. Michler, A. Hangleiter, A. Moritz and *et.al.* Influence of exciton ionization on recombination dynamics in $\text{In}_{0.53}\text{Ga}_{0.47}\text{As}/\text{InP}$ quantum wells. Phys. Rev. B. **47**(1993):1671-1674.
- [84] J. Kovac, H. Schwelzer and M. H. Pikuhn. Influence of the kinetic energy of electrons on the formation of excitons in a shallow $\text{In}_x\text{Ga}_{1-x}\text{As}/\text{GaAs}$ quantum well. Phys. Rev. B. **54**(1996): 13440-13443.
- [85] P.L. Souza, L. Samuelson and *et.al.* Evaluation of carrier capture times for very thin InGaAs/InP quantum-wells. Brazilian J. Phys. **24** (1994): 175-179.
- [86] S. Marcinkevicius, H. Hillmer and *et.al.* Photoexcited dynamics in $\text{InAlGaAs}/\text{InP}$ quantum well laser structures. Appl. Phys. Lett. **69** (1996):1101-1103.
- [87] G. Bacher, H. Schweizer, J. Kovac and *et.al.* Influence of barrier height on carrier dynamics in strained $\text{In}_x\text{Ga}_{1-x}\text{As}/\text{GaAs}$ quantum wells. Phys. Rev. B. **43**(1991): 9312-9315.
- [88] G.S. Buller, S.J. Fancey and *et.al.* Time-resolved photoluminescence measurements of InGaAs/InP multiple-quantum-well structures at 1.3 microns wavelengths by use of germanium single-photon avalanche photodiodes. Appl. Opt. **35**(1996): 916-921.
- [89] U. Cebulla and *et.al.* Superlattices and microstructures **5**(1989): 227.

- [90] W. Pickin and J. P. R. David. Carrier decay in GaAs quantum wells”
Appl. Phys. Lett. 56(1990): 268-270.
- [91] M. Gurioli, Am Vinattieri, and M. Colocci. Temperature dependence of
the radiative and nonradiative recombination time in GaAs/Al_xGa_{1-x}As quantum-well structures. Phys. Rev. B. 44(1991): 3115-3124.

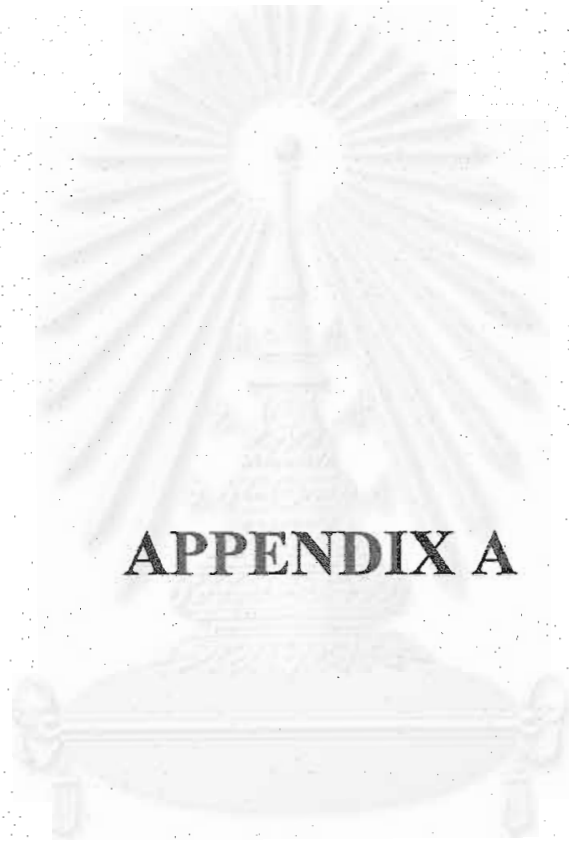


สถาบันวิทยบริการ
จุฬาลงกรณ์มหาวิทยาลัย



APPENDICIES

สถาบันวิทยบริการ
จุฬาลงกรณ์มหาวิทยาลัย



APPENDIX A

สถาบันวิทยบริการ
จุฬาลงกรณ์มหาวิทยาลัย

In_{1-x}Ga_xAs_yP_{1-y} Model Parameters

The parameters used here were fixed primarily by Mark Silver during his visit to Nortel, Canada in 1997/8. This parameter is using in a program written by Goef.

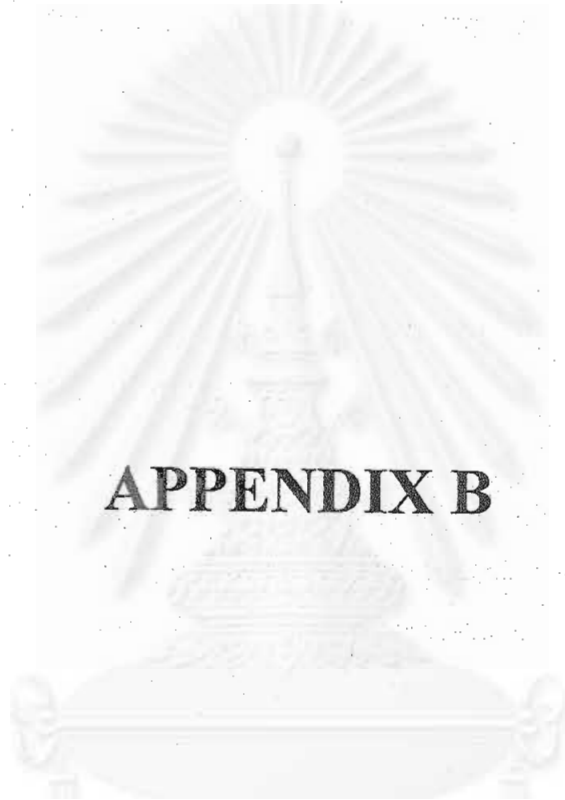
Binary Parameter

Parameter	GaAs	InAs	InP	GaP
Lattice constant (angstroms)	5.6533	6.0583	5.8687	5.4510
C11(x10 ¹¹ dynes cm ⁻²)	11.88	8.329	10.22	14.12
C12(x10 ¹¹ dynes cm ⁻²)	5.38	4.526	5.76	6.253
Dielectric Constant	12.85	15.15	12.56	11.10
Electron effective mass	0.067	0.023	0.079	0.17
Heavy hole effective mass	0.377	0.342	0.52	0.50
Light hole effective mass	0.068	0.025	0.12	0.14
4 K unstrained gap (eV)	1.5192	0.4105	1.4140	2.853
300 K unstrained gap (eV)	1.424	0.36	1.350	2.74
Spin orbit splitting (eV)	0.34	0.371	0.114	0.08
Vb hydrostatic def pot (eV)	1.16	1.0	1.27	1.7
Cb hydrostatic def pot (eV)	-8.0	-4.881	-4.91	-7.75
Uniaxial def pot (eV)	-1.7	-1.8	-1.5	-1.5
Average vb energy (eV)	-6.84	-6.68	-7.04	-7.06

Ternary parameters

Parameter	GaAs/InAs	InAs/InP	InP/GaP	GaP/GaAs
4k unstrained gap bowing (eV)	0.45	0.28	0.79	0.21
300 K unstrained gap bowing (eV)	0.475	0.36	0.786	0.166
Quaternary gap bowing (eV)	1.0			

สถาบันวิทยบริการ
จุฬาลงกรณ์มหาวิทยาลัย



APPENDIX B

สถาบันวิทยบริการ
จุฬาลงกรณ์มหาวิทยาลัย

Bilinear interpolation

For a material parameter, M , this method assumes a linear variation of M for a ternary alloy between its two binary alloys values, and then a bilinear variation of M for a quaternary $\text{In}_{1-x}\text{Ga}_x\text{As}_y\text{P}_{1-y}$ alloy between the four constituent binaries InP, InAs, GaP and GaAs. This approach is essentially an expansion of Vegard's Law, is commonly used in the literature, and is reasonably accurate for a large number of different material properties. The equation is as follows:

$$M_{\text{In}_{1-x}\text{Ga}_x\text{As}_y\text{P}_{1-y}} = (1-x)yM_{\text{InAs}} + (1-x)(1-y)M_{\text{InP}} + x(1-y)M_{\text{GaP}} + xyM_{\text{GaAs}} \quad (\text{B1})$$

The following material parameters for a quaternary alloys are calculated using the bilinear interpolation method:

lattice constant a

effective masses m^*_j of all three carriers

conduction band hydrostatic deformation potential A_c

valence band hydrostatic deformation potential A_v

uniaxial deformation potential B

elastic constants C_{11} and C_{12}

spin orbit splitting Δ_0

Interpolation scheme for the unstrained bandgap (E_g)

A linear interpolation scheme is not accurate enough for the bandgap of ternary and quaternary alloys. However, with the addition of additional terms, called the bowing parameters, B , the method again produces reasonable accuracy to experimental results. For each ternary alloy, there is one bowing parameter. A quaternary then depends on the interpolation of the ternary values, with an additional quaternary bowing term. The four ternary and one quaternary equation are as follows:

$$\begin{aligned}
E_{g \text{ In}_{1-x}\text{Ga}_x\text{As}} &= x E_{g \text{ GaAs}} + (1-x) E_{g \text{ InAs}} + x(x-1) B_{\text{In}_{1-x}\text{Ga}_x\text{As}} \\
E_{g \text{ In}_{1-x}\text{Ga}_x\text{P}} &= x E_{g \text{ GaP}} + (1-x) E_{g \text{ InP}} + x(x-1) B_{\text{In}_{1-x}\text{Ga}_x\text{P}} \\
E_{g \text{ GaAs}_y\text{P}_{1-y}} &= y E_{g \text{ GaAs}} + (1-y) E_{g \text{ GaP}} + y(y-1) B_{\text{GaAs}_y\text{P}_{1-y}} \\
E_{g \text{ InAs}_y\text{P}_{1-y}} &= y E_{g \text{ InAs}} + (1-y) E_{g \text{ InP}} + y(y-1) B_{\text{InAs}_y\text{P}_{1-y}}
\end{aligned} \tag{25}$$

$$\begin{aligned}
E_{g \text{ In}_{1-x}\text{Ga}_x\text{As}_y\text{P}_{1-y}} &= \\
& \frac{x(1-x) \left[y E_{g \text{ In}_{1-x}\text{Ga}_x\text{As}} + (1-y) E_{g \text{ In}_{1-x}\text{Ga}_x\text{P}} \right] + y(1-y) \left[x E_{g \text{ GaAs}_y\text{P}_{1-y}} + (1-x) E_{g \text{ InAs}_y\text{P}_{1-y}} \right]}{x(1-x) + y(1-y)} \\
& - x(1-x)y(1-y) B_{\text{In}_{1-x}\text{Ga}_x\text{As}_y\text{P}_{1-y}}
\end{aligned} \tag{B2}$$

The bowing parameters have been empirically determined; values are included in the table which follows.

Interpolation scheme for unstrained valence band energy (E_v)

We use the method of Krijn[ref 18] to interpolate the absolute valence band energy of quaternaries from the binary values. It is similar to the above interpolation scheme for the E_g , but with bowing parameters which are approximately calculated instead of empirically determined. The ternary bowing terms are dependent on the deformation potential and bulk lattice constants of the two binaries, as shown below for the ternary InGaAs:

$$B_{\text{In}_{1-x}\text{Ga}_x\text{As}} = 3 \cdot (A_v \text{GaAs} - A_v \text{InAs}) \cdot \frac{(a_{\text{GaAs}} - a_{\text{InAs}})}{a_0} \tag{26}$$

where a_0 is the lattice constant of the substrate. The bowing parameters for the other ternaries can be determined similarly using the appropriate binary values. Any additional bowing for the quaternary material has not been determined as of yet, so the parameter is set to zero, i.e. $B_{\text{InGaAsP}}=0$. The values of E_v can thus be determined by using these ternary and quaternary bowing parameters in an equation of the form of eqn. [25]. This interpolation method seems to produce values for relative offsets between materials that agree reasonably well with those that have been measured experimentally (binaries and a few ternaries).

Biography

Miss Sunida Awirothananon was born on April 11th 1976 in Chiang Rai, Thailand. She graduated bachelor's degree from Chiang Mai University in 1997. Her major was Science, especially physics. In the middle of 1998, she participated in international women in engineering and science training for 18 month at national research council of Canada (NRC), Ottawa, Canada. The research topic was focus on diffusion coefficient and residual damage in InGaAs/InP Quantum well heterostructure and quantum well intermixing. In 1999, she presented poster at Photonic's north international conference on the application of photonic technology (ICAPT) in Quebec, Canada. Her poster was shown in Intermixing Properties for In_{1-x}Ga_xAs_{1-y}Py/InP Quantum Well Structures with Varying Initial Composition and Strain Profiles. She also published "Tuning of the Electronic Properties of Self-Assembled InAs/InP quantum dots by rapid thermal annealing" in MRS 2000 proceeding. She has been also awarded developed and promotion of science and technology Talent (DPST) scholarship since 1994. During her study at Chiang Mai University, she was nominated bronze medal and excellent development mark certificate in 1995. Furthermore she was selected honor badge and excellent GPA certificate for her bachelor's degree from Processor Tab Neelannithi Foundation award in 1997. She has started her master's degree with Thailand Graduated Institute of Science and Technology (TGIST) scholarship since 1998.